

Targeted optimization of chromatographic columns based on 3D analysis of packing microstructure

Kumulative Dissertation

zur Erlangung des Doktorgrades
der Naturwissenschaften (Dr. rer. nat.)

dem Fachbereich Chemie
der Phillips-Universität Marburg
vorgelegt von

Arved Ernst Reising, M.Sc.

geboren in Göttingen

Marburg an der Lahn, 2017

Originaldokument gespeichert auf dem Publikationsserver der
Philipps-Universität Marburg
<http://archiv.ub.uni-marburg.de>



Dieses Werk bzw. Inhalt steht unter einer
Creative Commons
Namensnennung
Weitergabe unter gleichen Bedingungen
4.0 International Lizenz.

Die vollständige Lizenz finden Sie unter:
<https://creativecommons.org/licenses/by-sa/4.0/deed.de>

Vom Fachbereich Chemie der Philipps-Universität Marburg (Hochschulkennziffer 1180) als
Dissertation angenommen am:_____.

Erstgutachter: Prof. Dr. Ulrich Tallarek
Zweitgutachter: Prof. Dr. Bernhard Roling

Tag der mündlichen Prüfung:_____.

Die vorliegende Arbeit wurde in der Zeit von Mai 2013 bis September 2017 am Fachbereich
Chemie der Philipps-Universität Marburg unter Leitung von Prof. Dr. Ulrich Tallarek
angefertigt.

Teile der Dissertation wurden bereits in den folgenden Artikeln veröffentlicht:

A.E. Reising, J.M. Godinho, K. Hormann, J.W. Jorgenson, U. Tallarek, Larger voids in mechanically stable, loose packings of 1.3 μm frictional, cohesive particles: Their reconstruction, statistical analysis, and impact on separation efficiency, *J. Chromatogr. A* 1436 (2016) 118–132. doi:10.1016/j.chroma.2016.01.068.

A.E. Reising, J.M. Godinho, J.W. Jorgenson, U. Tallarek, Bed morphological features associated with an optimal slurry concentration for reproducible preparation of efficient capillary ultrahigh pressure liquid chromatography columns, *J. Chromatogr. A* 1504 (2017) 71–82. doi:10.1016/j.chroma.2017.05.007.

J.M. Godinho, A.E. Reising, U. Tallarek, J.W. Jorgenson, Implementation of high slurry concentration and sonication to pack high-efficiency, meter-long capillary ultrahigh pressure liquid chromatography columns, *J. Chromatogr. A* 1462 (2016) 165–169. doi:10.1016/j.chroma.2016.08.002.

A.E. Reising, S. Schlabach, V. Baranau, D. Stoeckel, U. Tallarek, Analysis of packing microstructure and wall effects in narrow-bore ultrahigh pressure liquid chromatography columns using focused-ion beam scanning electron microscopy, *J. Chromatogr. A* 1513 (2017) 172–182. doi: 10.1016/j.chroma.2017.07.049.

Danksagung

Diese Arbeit wurde erst durch die Unterstützung vieler Leute ermöglicht. Hiermit möchte ich mich bei all jenen bedanken, die mich in den letzten Jahren unterstützt haben und mit denen ich zusammengearbeitet habe. Ein besonderer Dank gilt dabei meinem Betreuer Prof. Dr. Ulrich Tallarek, der mir die Möglichkeit gegeben hat an einem hochinteressanten, für viele Anwendungen wichtigem Thema zu arbeiten und dabei vielfältige, spannende Kooperationen mit anderen Forschergruppen unterstützt hat. In dieser Zeit habe ich viel über die wissenschaftliche Forschung gelernt und bin von ihm stets gefordert und gefördert worden.

Ich freue mich, dass Prof. Dr. Bernhard Roling, mit dem wir ein sehr spannendes Projekt gestartet haben, sich bereit erklärt hat, das Zweitgutachten zu erstellen. Darüber hinaus möchte ich mich Prof. Dr. Robert Berger für die Beteiligung an der Prüfungskommission bedanken.

Weiterhin möchte ich den Mitgliedern der Arbeitsgruppe Tallarek für die jahrelange gute und erfolgreiche Zusammenarbeit danken. Dies gilt insbesondere für Dr. Stefan Bruns, Dr. Kristof Hormann und Tibor Müllner für die Einarbeitung in verschiedene Methoden, für Dr. Daniela Stöckel, Dr. Vasili Banarau, Dr. Dzmitry Hlushkou für die Zusammenarbeit in gemeinsamen Projekten und für Julia Rybka für viele hilfreiche Diskussionen und die Auflockerung des Labor- und Büroalltags. Ebenfalls möchte ich mich bei Kai Peter, Tobias Weimar, Moritz Kroll, Janek Bernzen und Ralph Kusche bedanken, die ich in ihren Bachelorarbeiten, Forschungspraktika oder Masterarbeiten betreuen durfte und die durch ihre Beiträge meine Forschung unterstützt haben.

Einen elementaren Beitrag haben unsere verschiedenen Kooperationspartner geliefert. Prof. Dr. James W. Jorgenson und Dr. Justin Godinho (Department of Chemistry, University of North Carolina, Chapel Hill) danke ich für ihre exzellente Arbeit beim Packen und der chromatographischen Charakterisierung der Kapillarsäulen und die vielen produktiven Diskussionen während der Interpretation unserer Ergebnisse und der Planung neuer Experimente. Prof. Dr. Schachtner, Dr. Franz Grolig und Dr. Martin Kollmann (Fachbereich Biologie, Philipps-Universität Marburg) danke ich für die Genehmigung der Mitbenutzung des Konfokal-Lasermikroskops sowie die Einweisung in das Gerät und Unterstützung bei Problemen. Ebenfalls bedanken möchte ich mich bei Dr. Christian Kübel, Dr. Sabine Schlabach und Dr. Torsten Scherer (Karlsruhe Nano Micro Facility (KNMF), Karlsruhe Institute of Technology, Eggenstein-Leopoldshafen), die durch ihre Unterstützung erfolgreiche elektronenmikroskopische Aufnahmen von dreidimensionalen Strukturen ermöglicht haben. Bei Prof. Dr. Bernhard Roling, Nico Kaiser, Stefan Spannenberger (Fachbereich Chemie, Philipps-Universität Marburg) und Dr. Yuki Katoh (Toyota Motor Europe, Belgien) möchte ich mich für die interessante Zusammenarbeit auf dem Gebiet der Festelektrolytbatterien bedanken, die verspricht in naher Zukunft zu einer wissenschaftlichen Publikation zu führen.

Einen nicht zu vernachlässigenden Beitrag bei vielen kleineren und größeren Problemen haben weitere Mitglieder, die Werkstätten und die Serviceabteilungen des Fachbereichs Chemie geliefert. Explizit bedanken möchte ich mich bei Rüdiger Penzel für seine Hilfe mit chromatographischen Anlagen, bei Michael Hellwig für die Unterstützung am Elektronenmikroskop und bei Dr. Hermann Uchtmann für die Unterstützung beim Zuschneiden von Proben.

Zum Abschluss möchte ich mich bei meiner Familie und meinen Freunden bedanken, die mich während der gesamten Studienzeit und der Promotion stets unterstützt haben.

Contents

I. Abstract	1
II. Zusammenfassung.....	4
III. Introduction	7
III.1 Motivation	7
III.2 Mechanisms of band broadening.....	9
III.3 Imaging methods	12
III.3.1 CLSM.....	12
III.3.2 FIB-SEM	14
Chapter 1.....	20
1.1 Introduction	21
1.2 Experimental.....	23
1.2.1 Chemicals and materials.....	23
1.2.2 Preparation of capillary UHPLC columns.....	24
1.2.3 Chromatographic analysis	24
1.2.4 Imaging of packing microstructure.....	25
1.2.5 Image restoration and bed reconstruction.....	26
1.2.6 Analysis of the reconstructions	27
1.2.7 Scanning electron microscopy (SEM).....	28
1.2.8 Pycnometry.....	29
1.3 Results and discussion	29
1.3.1 Kinetic column performance	29
1.3.2 Physical reconstructions and bed morphology	32
1.4 Conclusions	45
Chapter 2.....	55
2.1 Introduction	56
2.2 Experimental.....	57
2.2.1 Chemicals and materials.....	57
2.2.2 Preparation of capillary UHPLC columns.....	57
2.2.3 Acquisition of videos during the packing process.....	58
2.2.4 Chromatographic characterization.....	58
2.2.5 Imaging of packing microstructure.....	58
2.2.6 Image restoration and bed reconstruction.....	60
2.2.7 Analysis of reconstructions	61
2.2.8 Scanning electron microscopy.....	62

2.3 Results and discussion	62
2.3.1 Kinetic performance of the packed columns	62
2.3.2 Bed reconstruction and morphological analysis	65
2.3.2.2 Analysis of larger voids.....	70
2.3.2.3 Investigation of bed formation	73
2.4 Conclusions	74
Chapter 3.....	81
3.1 Introduction	81
3.2 Materials and Methods	83
3.2.1 Chemicals and materials.....	83
3.2.2 Preparation of capillary UHPLC columns.....	83
3.2.3. Chromatographic analysis	84
3. Results and Discussion	85
4. Conclusions	87
Chapter 4.....	92
4.1 Introduction	93
4.2 Experimental.....	96
4.2.1 Chemicals and materials.....	96
4.2.2 Column bed embedding and FIB-SEM imaging	96
4.2.3 Scanning electron microscopy (SEM).....	98
4.2.4 Image restoration	99
4.2.5 Image reconstruction	101
4.2.6 Reconstruction analysis	101
4.2.7 Simulation of fluid flow	102
4.3 Results and discussion	103
4.4 Conclusions	109
IV. Conclusions and perspective	116
V. Appendix	120
V.1 Curriculum vitae	120
V.2 Publikationsverzeichnis	121
V.3 Erklärungen.....	122

I. Abstract

The preparation, structure, and performance of functional materials porous are strongly interrelated. Hence, a detailed analysis of the pore structure of a functional porous material in combination with a detailed characterisation of its performance can provide an understanding of the influence of individual parameters during preparation and thus identify structural limitations to an improved utilization. The obtained results can be used to tune the preparation towards a better pore structure suited for the targeted application. This work focuses on packings of silica-based particles for highly efficient chromatographic separations. The prepared packings combine an interparticle macropore space for fast flow-based transport with an intraparticle mesopore space providing high surface areas for molecule-surface interactions. Such packed columns have a wide field of application, not only in highly efficient separations, but also for catalysis, and (energy) storage. However, the focus here is on separations in liquid chromatography.

In Chapter 1, the influence of the slurry concentration on separation efficiency and bed structure was investigated for capillary columns (75 μm inner diameter, 30 cm length) packed with 1.3 μm bridged-ethyl hybrid (BEH) fully porous silica particles. The slurry concentration was varied from 5 to 50 mg/mL while every other packing parameter was kept constant. Chromatographic characterisation with hydroquinone as weakly retained analyte revealed highly efficient separations (reduced plate heights as low as 1.5) at an optimal intermediate slurry concentration of 20 mg/mL for this specific set of packing parameters. Confocal laser scanning microscopy (CLSM) was utilized to conduct a three-dimensional reconstruction and to carry out a detailed morphological analysis of the column with the best performance, a column packed with a slurry concentration below the optimum, and one packed above the optimum. Two counteracting effects were revealed: Radial heterogeneities limit the separation efficiency for columns packed at low slurry concentrations. With an increase in slurry concentration, these radial effects get suppressed but the number and size of large voids with a diameter similar to the mean particle diameter increase significantly. Interestingly, the reconstructions also revealed high external bed porosities between 0.47 and 0.50 which are higher than expected with respect to the random loose packing limit reported for frictional, cohesionless particles. However, no signs of bed instability could be observed demonstrating the significant impact of interparticle forces for particles as small as 1.3 μm .

In Chapter 2, the investigation of the optimal slurry concentration was expanded by analysing the effects for a different particle size to obtain a more general picture. A similar set of capillary columns (75 μm inner diameter, 45 cm length) was packed with 1.9 μm BEH particles at eleven different slurry concentrations between 5 and 200 mg/mL including additional tests for reproducibility at selected concentrations and the observation of bed formation using optical microscopy. While comparable reduced plate heights were achieved, the observed optimum of 140-160 mg/mL to pack highly efficient columns reproducibly differed significantly from the 20 mg/mL for the 1.3 μm particles identified in Chapter 1. This can be explained by the difference in the particle diameter as interparticle forces and particle aggregation become more dominant at still smaller diameters. CLSM-based reconstructions revealed similar trends in the

bed structures as seen in Chapter 1. At low concentrations, pronounced ordered particle layers in the direct vicinity of the column wall, local bed densification near the column wall, and particle size-segregation limit the achieved separation efficiency. The peculiarity of the first effect is continuously decreasing with an increase in the slurry concentration even beyond the optimum while the latter two effects are already suppressed at the optimal slurry concentration. On the other hand, the number and size of large voids increase with an increase in the utilized slurry concentration as already seen in Chapter 1. The videos acquired during column packing provided very helpful insights into bed formation mechanisms and thus delivered possible explanations for these structural features. At 10 mg/mL, particles arrive individually at the bed front allowing individual settlement and rearrangement on the arrival of following particles what allows a discrimination of particles according to their individual properties. The picture looks completely different for 100 mg/mL as example for higher concentrated slurries. Here, particles tend to aggregate during packing and arrive in large batches. This prevents discrimination of individual particles but significantly reduces the chances for rearrangement and is thus prone to the conservation of defects formed between the border of the arriving batches of particles and the front of the bed.

Chapter 3 is based on the results obtained during the work presented in Chapters 1 and 2. The combination of high slurry concentration and ultrasound was already proposed there as chance to keep transcolumn heterogeneities as low as possible while preventing the formation of large voids. To test this hypothesis, two sets, each consisting of three capillary columns (75 μm inner diameter, 100 cm length) were packed with 1.9 μm BEH particles at a slurry concentration of 200 mg/mL; one set under application of ultrasound during packing, the other one without. All three columns, which underwent sonication, showed significantly better performance than each of the other columns. The obtained reduced minimum plate height for a weakly retained analyte was even lower than the already impressive value of 1.5 for columns packed at a slurry concentration optimal for packing without sonication and reached values close to unity over a length of 1 m for the best-performing column. The achieved theoretical plate counts of $\sim 500,000$ demonstrate a unique potential for highly efficient separations of extremely complex samples.

In Chapter 4, the focus is shifted from capillary columns to the more common analytical format. CLSM could not be applied here as the steel columns are not transparent and extrusion of the bed is not possible without losing either stability or optical transparency. Thus, an imaging and reconstruction procedure based on focused ion beam scanning electron microscopy was developed using a commercial narrow-bore analytical column (2.1 mm inner diameter, 50 mm length) packed with 1.7 μm BEH particles. The packing was embedded with poly(divinylbenzene) prior to extrusion from the steel column in order to conserve the bed structure. Two image stacks were acquired and reconstructed at characteristic positions within the bed: one in the central section of the column along the flow direction to obtain the bulk properties of the bed and one from the column wall towards the column centre to investigate and quantify the influence of the geometrical wall effect and the second wall effect. To investigate the effect of the microstructure in the wall region on local flow through the bed, a radially resolved flow profile was obtained by lattice-Boltzmann simulations. For this column,

the region affected by wall effects spanned over approximately 62 particle diameters showing a decrease in the local mean porosity by up to 10% and an increase in the local mean particle diameter by up to 3% with respect to the bulk region inducing a decrease of the local flow velocity by up to 23%. Furthermore, four more ordered layers of particles were formed directly at the hard column wall due to the geometrical wall effect leading to local velocity fluctuations by up to a factor of three. These quantified structural features are in excellent agreement with previous reports about macroscopic characterisations of the wall effects by optical or chromatographic measurements.

II. Zusammenfassung

Die Herstellung eines Materials, seine Struktur und seine funktionellen Eigenschaften stehen in einem direkten Zusammenhang miteinander. Daher ist eine detaillierte Analyse der Porenstruktur eines Funktionsmaterials, Hand in Hand mit einer detaillierten anwendungsorientierten Charakterisierung, extrem hilfreich für das Verständnis der Auswirkungen einzelner Präparationsparameter und zur Identifikation von strukturellen Limitierungen in der Anwendung. Eine Betrachtung aller erhaltenen Ergebnisse im Gesamtkontext ermöglicht, den Herstellungsprozess und damit die Porenstruktur gezielt für spezielle Anwendungen zu optimieren. In dieser Arbeit wurden Packungen von siliciumdioxid-basierten Partikeln untersucht, die einen interpartikulären Makroporenraum, der schnellen Stofftransport durch Porenströmung ermöglicht, mit einer hohen intrapartikulären Oberfläche für Wechselwirkungen mit Zielmolekülen kombinieren. Diese haben vielfältige Anwendungen in hocheffizienten Stofftrennungen und Katalyse, sowie der Stoff- und Energiespeicherung. Als spezielle Anwendung stand dabei die Stofftrennung durch Flüssigchromatographie im Vordergrund dieser Arbeit.

Im ersten Kapitel wurde dabei der Einfluss der Suspensionskonzentration während des Packprozesses auf die chromatographische Effizienz und die Bettstruktur von Kapillarsäulen (75 μm innerer Durchmesser, 30 cm Länge) am Beispiel von Acquity BEH (bridged ethyl hybrid) Partikeln mit einem durchschnittlichen Durchmesser von 1.3 μm untersucht. Dazu wurden neun Säulen bei einer schrittweisen Erhöhung der Suspensionskonzentration von 5 mg/mL auf 50 mg/mL gepackt, wobei alle weiteren Packparameter konstant gehalten wurden. Die chromatographische Charakterisierung mit Hydrochinon als schwach retardiertem Analyten zeigte ausgezeichnete Trenneffizienzen, wobei das beste reduzierte Bodenhöhenminimum von 1.5 bei einer mittleren Suspensionskonzentration von 20 mg/mL erhalten wurde. Sowohl höhere als auch niedrige Konzentrationen zeigten signifikant schlechtere Effizienzen. Um die Ursachen für diese unterschiedlichen Trennleistungen zu verstehen, wurden drei der gepackten Säulen für dreidimensionale Rekonstruktionen ihrer Bettstrukturen mittels Konfokal-Lasermikroskopie (CLSM, confocal laser scanning microscopy) ausgewählt: eine Säule repräsentativ für Suspensionskonzentrationen unterhalb des Optimums, die Säule mit der höchsten Trenneffizienz und eine Säule repräsentativ für Suspensionskonzentrationen oberhalb des Optimums. Dabei konnten zwei gegenläufige Effekte identifiziert werden. Bei niedrigen Suspensionskonzentrationen limitieren radiale Heterogenitäten die Trenneffizienz, die bei höheren Konzentrationen zunehmend unterdrückt wurden. Gegenläufig bilden sich allerdings bei zunehmenden Konzentrationen mehr und mehr Hohlräume in der Größe eines typischen Partikels in der Struktur, wobei sowohl deren Größe als auch deren Zahl mit der Suspensionskonzentration zunimmt. Am Optimum wurden diese Effekte am besten ausbalanciert. Ein weiterer interessanter Aspekt dieser Säulen sind ihre hohen interpartikulären Porositäten zwischen 0.47 und 0.50, die sogar höher sind, als Untersuchungen der Stabilität loser Kugelpackungen erwarten ließen. Der Umstand, dass keinerlei Instabilitäten der Bettstrukturen beobachtet werden konnten, verdeutlicht den

signifikanten Einfluss von interpartikulären, stabilisierenden Wechselwirkungen für derartig kleine Partikel.

Im zweiten Kapitel wurde die Untersuchung des Einflusses der Suspensionskonzentration vertieft, um ein allgemeineres Bild zu erhalten. Dazu wurde analog zum ersten Kapitel eine weitere Serie von Säulen gepackt, wobei diesmal Acquity BEH Partikel mit einem durchschnittlichen Durchmesser von 1.9 μm verwendet wurden. Es wurden elf Säulen (75 μm innerer Durchmesser, 45 cm Länge) mit Suspensionskonzentrationen zwischen 5 und 200 mg/mL gepackt, wobei für ausgewählte Konzentrationen (20 mg/mL, 80 mg/mL, 140 mg/L) die Reproduzierbarkeit des Packprozesses untersucht wurde und zusätzlich Videos während der Ausbildung des Säulenbettes für 10 und 100 mg/mL aufgenommen wurden. Die chromatographische Charakterisierung zeigte vergleichbare minimale reduzierte Bodenhöhen zu den 1.3 μm Partikeln aus Kapitel 1. Allerdings liegt das Optimum für das reproduzierbare Packen hocheffizienter Säulen bei deutlich höheren Suspensionskonzentrationen von 140–160 mg/mL (im Vergleich zu 20 mg/mL in Kapitel 1). Dies lässt sich durch den signifikanten Größenunterschied zwischen den beiden Partikeltypen erklären, da die interpartikulären Wechselwirkungen mit kleinerem Durchmesser massiv an Einfluss gewinnen. Es wurden ebenfalls CLSM-basierte Rekonstruktionen durchgeführt, die ähnliche strukturelle Trends identifizieren wie in Kapitel 1. Bei niedrigen Suspensionskonzentrationen zeigen sich geordnete Partikellagen direkt an der Säulenwand gefolgt von zufälliger aber verdichteter Packungsstruktur in der Nähe der Säulenwand, sowie eine radiale Diskriminierung der Partikel anhand ihrer Größe. Diese Effekte werden mit zunehmender Konzentration unterdrückt bzw. zunehmend in ihrer Ausprägung reduziert, wobei gegenläufig eine zunehmende Ausbildung von größeren Hohlräumen zu beobachten ist. Die aufgenommenen Videos liefern Anhaltspunkte, wie sich diese Strukturen ausbilden. Bei einer Konzentration von 10 mg/mL erreicht ein kontinuierlicher Strom von einzelnen Partikeln die Front des Packungsbettes, was mehrfaches Umlagern und radiale Diskriminierungen ermöglicht. Ein komplett anderes Bild zeigt sich bei hohen Konzentrationen. Hier erreichen größere Aggregate von Partikeln die Bettfront, was die Chance für spätere Umlagerungen reduziert, aber jegliche Defekte, die sich beim Auftreffen der Aggregate auf die Bettfront bilden, konserviert.

Das dritte Kapitel baut auf den Ergebnissen der ersten beiden Kapitel auf, um eine weitere Verbesserung des Packverfahrens zu erreichen. Dort wurde die mögliche Kombination von hohen Suspensionskonzentrationen zur Reduzierung der radialen Heterogenitäten mit dem Einsatz von Ultraschall während des Packprozesses als mögliche Lösung diskutiert. Um diese Hypothese zu testen, wurden zwei Sets von je drei Säulen (75 μm innerer Durchmesser, 100 cm Länge) mit 1.9 μm Acquity BEH Partikeln bei einer Suspensionskonzentration von 200 mg/mL gepackt, wobei für ein Set nach dem gleichen Protokoll wie in Kapitel 2 gearbeitet wurde und für das andere Set zusätzlich Ultraschall eingesetzt wurde. Jede der Säulen, die mit Hilfe von Ultraschall gepackt wurde, zeigte eine signifikant bessere Trenneffizienz als jede der Säulen, die ohne Ultraschall gepackt wurden. Dabei wurden für schwach retardierte Analyten minimale reduzierte Bodenerhöhen von nahe 1 erreicht, welche sogar die bereits sehr guten Werte von 1.5 für optimale Packprotokolle ohne Ultraschall in den Kapiteln 1 und 2 deutlich

übertreffen. Damit zeigen die Säulen mit einer Bodenzahl von ca. 500.000 ein großes Potential für die hocheffiziente Trennung von sehr komplexen Proben.

Im vierten Kapitel wird der Fokus von Kapillarsäulen auf das deutlich weiter verbreitete analytische Format verlagert. In diesem kann CLSM nicht auf gepackte Säulenbetten angewendet werden, da die Säulengehäuse (gewöhnlich aus Edelstahl) nicht optisch transparent sind und bei einem Extrudieren des Bettes nicht gleichzeitig Struktur und optische Transparenz gewahrt werden können. Daher wurde auf der Basis von fokussiertem Ionenstrahl in Kopplung mit Rasterelektronenmikroskopie (FIB-SEM, focused ion beam scanning electron microscopy) ein Abbildungs- und Rekonstruktionsverfahren anhand einer exemplarisch ausgewählten, kommerziellen narrow-bore Säule entwickelt (2.1 mm innerer Durchmesser, 5 cm Länge, 1.9 μm Acquity BEH Partikel). Vorbereitend wurde das gepackte Bett durch das Einbetten in Polydivinylbenzol stabilisiert und anschließend aus der Säule extrudiert. Zwei Bereiche wurden vermessen und rekonstruiert: ein Abschnitt im Bulkbereich der Säule entlang der Flussrichtung zur Untersuchung der Bulkeigenschaften und ein Abschnitt von der Säulenwand in Richtung der Säulenmitte, um die strukturellen Eigenschaften des geometrischen Wandeffektes und des sogenannten zweiten Wandeffektes zu charakterisieren und zu quantifizieren. Weiterhin wurden die Auswirkungen der Mikrostruktur in der Wandregion auf den Fluss durch die Säule mittels Simulationen unter Anwendung der lattice-Boltzmann Methode untersucht. Die Rekonstruktionen zeigen signifikante Unterschiede der Packungsstruktur in der Wandregion im Vergleich zur Bulkregion mit einer Ausdehnung von ca. 62 Partikeldurchmessern. Dabei ist die mittlere Porosität lokal um bis zu 10% reduziert und gleichzeitig der mittlere Partikeldurchmesser um bis zu 3% erhöht, was zusammen zu einer Reduktion der lokalen Fließgeschwindigkeit um bis zu 23% führt. Außerdem bilden sich durch den geometrischen Wandeffekt vier Partikellagen mit höherer Ordnung direkt an der Säulenwand aus, was zu lokalen Oszillationen der Fließgeschwindigkeit bis zu einem Faktor von drei führt. Diese Quantifizierungen einzelner Struktur- und Dynamikeffekte sind in exzellenter Übereinstimmung mit Arbeiten, welche die Wandeffekte durch makroskopische optische Messungen oder traditionelle chromatographische Messungen studiert haben.

III. Introduction

III.1 Motivation

A profound understanding of potentials and limitations of functional porous materials requires detailed knowledge of their transport properties and their three-dimensional (3D) morphology [1]. 3D imaging and reconstruction techniques allow the acquisition of detailed representations of their pore structure. Spatial analysis of these obtained models allows interpretation of the identified morphological characteristics with respect to the performance of the material. If this is utilized in studies varying systematically the manufacturing procedures, it can provide crucial insights into the influences of the varied parameters. This can be supported by computer based simulations of transport processes, either directly in reconstructed structures or in computer generated structures which can prove and quantify morphology-transport relationships. For example, such an investigation has been conducted for monolithic silica structures. Two different generations of commercial monoliths for chromatographic separations have first been analysed regarding their macropore structure [2]. Subsequent simulations of flow and dispersion in the reconstructed pore space were able to explain differences in their performances in detail [3]. Materials based on porous silica (which are also investigated in the work presented here) combine flow-through macropores with a mesopore and/or micropore network providing high surface areas for interaction between the surface (or surface-bonded ligands) and target molecules. This paves the way for a wide variety of applications in catalysis [4,5], (energy) storage [6–9], and separation science [10,11].

The work presented here is primarily focused on packed columns used in high performance liquid chromatography (HPLC). Since the first reported application in 1967 [12] the continuous reduction of the mean particle diameter has allowed to pack shorter and shorter columns with drastically improved performances [11]. At the same time, modern applications, especially with biological and medical samples, require a further improvement in column technology [13]. At the first glance simple solutions like the further reduction of the particle diameter or packing of longer columns face new challenges, e.g., higher backpressures require more advanced HPLC systems [14] or frictional heating in analytical columns starts to contribute significantly to band broadening [15–17]. One successful approach is the introduction of multi-dimensional chromatography which combines two or more columns with significantly different surface chemistries [18]. In addition, several new types of separation materials were introduced or re-introduced successfully. Columns with monolithic silica structures achieve decent separation efficiencies while maintaining very low backpressure allowing long columns with high flow rates for fast analyses [19]. The revisited concept of using particles with a solid core and a porous shell (core-shell particles) has achieved similar separation efficiencies as fully porous particles at larger particle diameters which significantly reduces the backpressure for the same application [20]. Simultaneously, tremendous work has been conducted to further push the column fabrication protocols. Column packing was considered an “art” for a long time, only improved by empirically driven optimization [21]. This started to change around the year 2000 when several groups began to systematically study the influence of specific packing parameters

and aimed to identify physical explanations for their observations. Investigations included the influence of mechanical stress during bed formation [22,23], of colloidal and hydrodynamic aspects [24–26], of particle shape and slurry conditions [21], and of cross-sectional channel geometries in HPLC microchips [27,28]. In 2011, Bruns and Tallarek implemented an imaging and reconstruction procedure for packed capillary columns providing a powerful tool to directly study the influence of different parameters on the resulting bed structure [29]. These capillary columns are challenging in their handling due to very high backpressures [30] and high sensitivity to extra-column band broadening but are important for the analysis of biological samples due to their high peak capacities, the compatibility with very small sample volumes, and the good compatibility of the low volumetric flow rates with mass spectrometry [30]. The reconstruction procedure was utilized to investigate the direct influence of several parameters on the packing of capillary columns and to obtain general insights on their role regarding column packing: the influence of particle types [31] and column diameter on the bed structure in cooperation with the group of Prof. Dr. James W. Jorgenson (University of North Carolina at Chapel Hill, Chapel Hill, NC, USA) [32]. In a following study, they started to investigate the influence of the slurry concentration with respect to bed structure and separation efficiency [33]. Capillary columns were packed at two different slurry concentrations for bridged-ethyl hybrid (BEH) fully porous particles with mean diameters between 0.9 and 1.9 μm and for 1.9 μm Kinetex core-shell particles. For each pair of columns, the higher slurry concentration resulted in a column with higher separation efficiency what can be explained by a significant reduction of radial heterogeneities. This went hand in hand with an increase in the number of larger packing voids (defects which could accommodate a particle with a diameter typical for the used batch). Based on these results, the existence of an optimal intermediate slurry concentration with best balance between the two effects was proposed. Chapters 1, 2 and 3 of the work presented here were conducted in cooperation with the Jorgenson group to test this hypothesis and to further optimize the packing process for BEH particles. Two series of capillary columns were packed with a gradual increase of the used slurry concentration: one with 1.3 μm BEH particles between 5 and 30 mg/mL (Chapter 1) and one with 1.9 μm BEH particles between 10 and 200 mg/mL (Chapter 2). We identified optimal slurry concentrations and investigated structural features behind these optima. The obtained insights were used for a further optimization of the packing protocol towards even better separation efficiencies (Chapter 3).

A different issue is the investigation of the packing structure of packed analytical columns which are more common regarding their application in conventional HPLC. CLSM is not suited for these columns as their steel or polymer housings are not optically transparent and the bed cannot be extruded without stabilization which, in turn, would result in significant structural changes. In Chapter 4, a reconstruction procedure utilizing focused ion-beam scanning electron microscopy (FIB-SEM) was introduced for a commercial narrow-bore column covering sample preparation, imaging, image restoration, and binarization. A long known structural feature limiting separation efficiency was chosen for investigation: the influence of the column wall on the bed structure in the vicinity of the column wall referred to as “wall effect”. Significant differences in the flow velocity and dispersion between the vicinity of the column wall and the

bulk region of packed chromatographic columns have been reported since a long time [34–37]. Shalliker et al. [38] achieved the first visual proof for two column wall effects in 2000 using a transparent 100×17 mm column and iodine as coloured, unretained marker analyte. The geometrical wall effect is formed due to the hard and smooth column wall which cannot be penetrated by the spherical particles. They form several layers of particles, with a high order for the first layer touching the column wall and a step-wise decrease in order by the following layers, until a random bed structure is reached. The second wall effect is formed between these ordered particle layers and the relatively homogeneous bulk region in the centre of the column due to friction between the bed and the column wall. This is investigated on a microstructural level by imaging and reconstruction of a section of the column spanning from its wall towards the centre of the bed and a section from the centre of the column which provides the bulk properties of the bed. The interpretation of the results regarding structural features limiting separation efficiency is supported by simulations using the lattice-Boltzmann method (LBM) which illuminate the influence of the structure on flow through the column and thus allow direct comparison with reported results from chromatographic experiments.

III.2 Mechanisms of band broadening

The most common model to describe band broadening in chromatography was developed by van Deemter et al. [39]. They simplified the solution of the kinetic model derived by Lapidus and Amundson by assuming a Dirac shape of the injection pulse [40]. In analogy to the plate theory introduced by Martin and Synge [41], the efficiency of a column is characterised by its height equivalent to a theoretical plate. The impact of different contributions to the plate height is described by the van Deemter equation

$$H = A + \frac{B}{u} + Cu \quad (\text{III.1})$$

where H is the plate height and u is the average mobile phase flow velocity. Three different contributions were identified: (i) eddy dispersion due to irregular flow paths through the column bed represented by the A -term, (ii) longitudinal diffusion along the column due to concentration gradients represented by the B/u -term, and (iii) mass transfer resistance due to diffusion of the analyte molecules into the mesopore network within the particles and out of the particles represented by the Cu -term. To allow the comparison of columns packed with different particle types and particle diameters, the dimensionless variant can be utilized

$$h = a + \frac{b}{v} + cv \quad (\text{III.2})$$

where the reduced plate height h can be obtained via the mean Sauter particle diameter d_s ($h = H/d_s$) and the reduced velocity v can be obtained via d_s and the pressure-dependent diffusion coefficient of the analyte in the bulk mobile phase D_m ($v = ud_s/D_m$) [42]. While Equations (III.1) and (III.2) fit well to most experimental chromatographic data, difficulties arise to relate the

resulting parameter values to actual physical processes taking place in the packed columns [43,44].

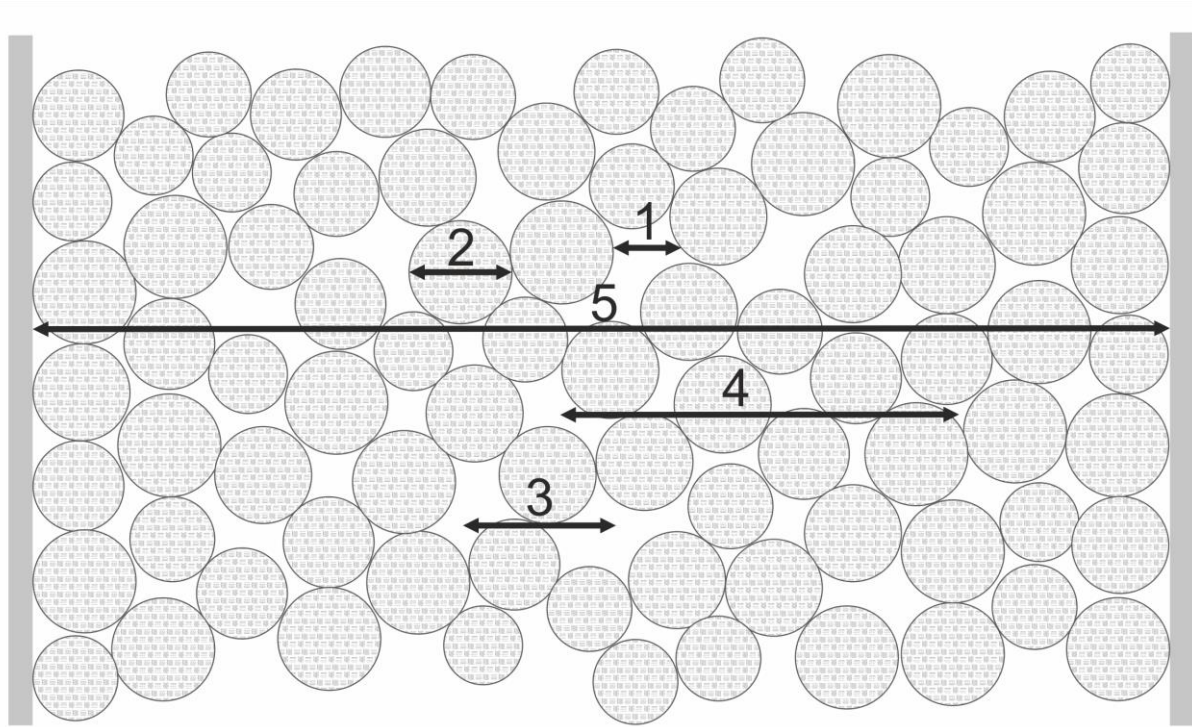


Fig. III.1: Characteristic length scales of flow heterogeneities in a packed bed according to Giddings [45]. 1 – transchannel effect; 2 – transparticle effect, 3 – short-range interchannel effect, 4 – long-range interchannel effect; 5 – transcolumn effect.

A more sophisticated model was introduced by Giddings [45] proposing a velocity dependent α -term by applying a random-walk model and a coupling between lateral diffusion and convection driven transport. He identified five different velocity inequalities contributing to zone spreading which are shown schematically in Fig. III.1: (1) the transchannel contribution due to velocity gradients across channels between individual particles, (2) the transparticle contribution due to exchange occurring through the stagnant mobile phase within the particles (this effect was identified as pore diffusion mechanism by Gritti and Guiochon [46] and, thus, is not discussed as part of eddy dispersion in the remainder of this work), (3) the short-range interchannel contribution due to velocity differences between neighbouring inter-particle channels with different diameters, (4) the long-range interchannel contribution due to velocity differences between regions with different average packing densities, and (5) the transcolumn contribution due to the difference between the bed region influenced by column wall effects and the central bulk region of the column. Their impact on the reduced plate height is described by the following expression:

$$h = \frac{b}{v} + \sum_i \frac{2\lambda_i}{1+2\lambda_i/(\omega_i v)} + cv \quad (\text{III.3})$$

λ_i and ω_i are structural parameters characterising the individual contribution i (with $i = 1$ representing the transchannel contribution, $i = 2$ representing the short-range interchannel contribution, $i = 3$ representing the transcolumen contribution, and $i = 4$ representing the long-range interchannel contribution). The structural parameters are directly correlated to the characteristic length scales of the individual contributions and to the characteristic velocity differences:

$$\lambda_i = \frac{\omega_{\lambda,i}\omega_{\beta,i}^2}{2} \quad (\text{III.4})$$

$$\omega_i = \frac{\omega_{\alpha,i}^2\omega_{\beta,i}^2}{2} \quad (\text{III.5})$$

$\omega_{\lambda,i}d_s$ is the characteristic longitudinal distance between two velocity extremes, $\omega_{\beta,i}$ represents the fractional departure of a velocity extreme from the mean velocity, and $\omega_{\alpha,i}d_s$ is the characteristic radial distance between two velocity extremes. At low velocities, the exchange process between slow and fast flow streams is dominated by diffusion in a linear dependence between reduced plate height and reduced velocity ($h_i \sim \omega_i v$). In contrast, convection driven exchange is dominant at high velocities where h_i approaches the constant value $2\lambda_i$. The transition between the two regimes is commonly described by the reduced transition velocity $v_{1/2,i} = 2\lambda_i/\omega_i$ where the corresponding plate height term reaches half of its limiting value. In the original model, these parameters do not account for retention. This has already been addressed by Giddings and Schettler by providing a general theory and its solutions for extremely low and extremely high velocities [47]. Recently, Daneyko et al. [48] developed an extension of the Giddings formula for fully porous and core-shell particles for a cell model which was then used to analyse the individual contributions by numerical simulations. While Giddings already derived approximations for the magnitude of the structural parameters, studies based on numerical simulations in computer generated packings allowed a more precise determination [48–50]. Daneyko et al. [48] investigated a model bulk packing structure with a porosity of 0.4 and identified two characteristic radial length scales: 0.11 particle diameters what can be assigned to transchannel eddy dispersion, and 1.37 particle diameters what can be assigned to short-range interchannel eddy dispersion. Further work based on numerical simulations in computer generated packings has allowed to identify typical reduced transitions velocities for the different contributions. Simulations in unconfined bulk provided values of $v_{1/2,1} \approx 200$ for the transchannel contribution and values of $v_{1/2,2} = 3\text{--}4$ for the short-range interchannel contribution whereas exact values depend on interstitial velocity and bed homogeneity [49,50]. For the transcolumen contribution, a computer generated, confined, cylindrical packing (diameter: 20 particle diameters; interstitial porosity: 0.40) was investigated providing $v_{1/2,3} = 227$. A long-range interchannel contribution was not identified in these simulations what can be explained in the following way: no corresponding structural feature was present in the computer generated packings.

III.3 Imaging methods

A wide portfolio of methods is available for 3D-imaging of functional materials [1,51–54]. For each sample, a suitable method has to be selected based on required volume, required resolution, and properties of the material, e.g., transparency, chemical composition, stability towards oxygen and water vapour, or hardness. Two methods were utilized during the work presented here: confocal laser scanning microscopy (CLSM) and focussed ion beam scanning electron microscopy (FIB-SEM). Both methods will be explained in more detail in the following paragraphs.

III.3.1 CLSM

Confocal laser scanning microscopy is an optical imaging method based on line-by-line scanning of a sample in combination with pixel-by-pixel detection. Contrast can be achieved with different strategies, e.g. local fluorescence (used here), differential interference contrast, or reflection. The main difference compared to a conventional microscope is the confocal aperture (or pinhole) resulting in the observation of a single point instead of simultaneous observation of all sample points. A schematic of the ray path in a typical CLSM is shown in Fig. III.2A. A laser beam is focussed to a single spot resulting in excitation of a fluorescent dye. The resulting emitted light is collected by the optical setup and directed through the pinhole and a wavelength-selective emission filter towards the detector. The pinhole results in exclusion of light emitted from outside the focal plane and the diameter of the pinhole determines the size of the imaged volume.

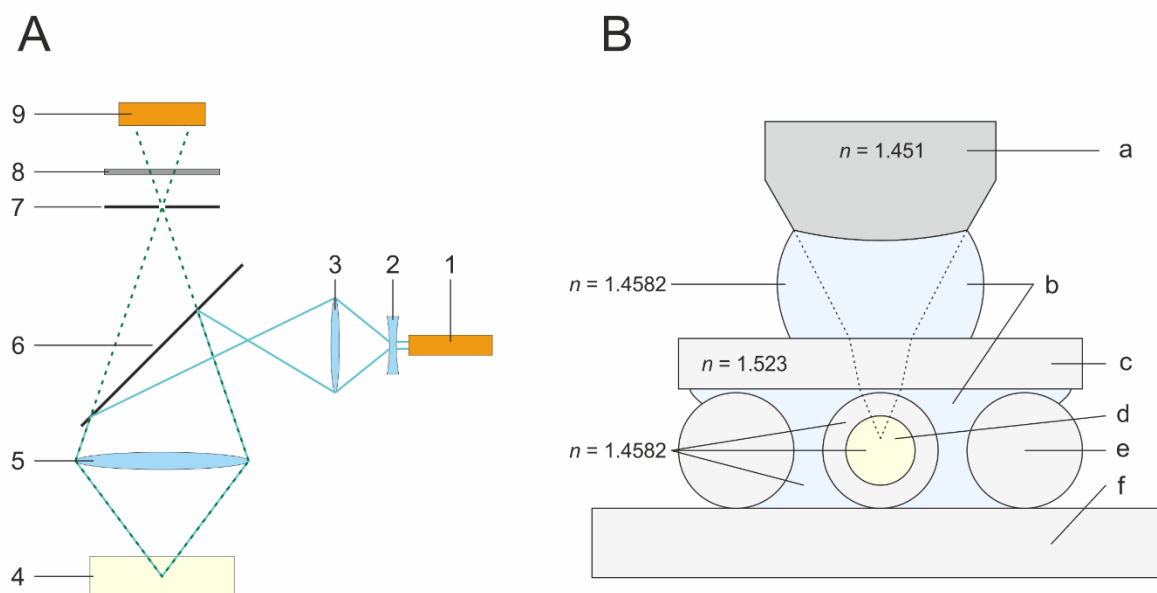


Fig. III.2: (A) Schematic of a confocal laser scanning microscope; (B) Schematic of the optical setup to image capillary columns (with refractive indices of important components). 1 – laser for excitation beam; 2,3 – beam expander; 4 – dichroic mirror; 5 – microscope objective; 6 – sample; 7 – pinhole; 8 – emission filter; 9 – detector; a – microscope objective; b – immersion/embedding medium; c – cover slide; d – stained and refractive index matched column bed; e – support capillaries; f – object slide.

To achieve highly resolved imaging deep into a porous material, the pores have to be filled with a liquid with perfect matching between the refractive indices of the material and the liquid. In addition, the optical setup, especially the used objective, has to be adapted to the refractive index of the material. In his dissertation, Stefan Bruns [55] developed a setup suitable for the investigation of the bed structure of capillary columns with glass wall and silica as porous material utilizing CLSM (Fig. III.2B) which was successfully utilized for the investigation of monolithic columns [56] and packed columns [29]. Glycerol/dimethyl sulfoxide (DMSO) water 70/19/11 (v/v/v) is used as refractive index matching liquid, embedding medium, and immersion medium as it mimics the refractive behaviour of silica over the utilized wave lengths. Consequently, the main source for a resolution loss is the mismatch of the refractive indices of the immersion medium and the objective. The replacement of the standard cover slip with a thickness of 170 μm by a “type 0” coverslip with a thickness of 120 μm significantly reduces spherical aberrations. Residual aberrations can be minimized by tuning of the correction collar of the objective.

The resolution potential of a CLSM is defined by the optical setup, the utilized wavelengths, and the width of the pinhole. A typical measure for the width of the pinhole is the Airy Unit (AU) which is defined as

$$1\text{AU} = \frac{1.22\lambda_{\text{ex}}}{NA} \quad (\text{III.6})$$

where λ_{ex} is the wavelength of the light used for excitation and NA is the numerical aperture of the objective. In case of fluorescence, the calculation of the resolution requires also the specific mean wavelength $\bar{\lambda}$ which considers both the excitation wavelength and the emission wavelength λ_{em} .

$$\bar{\lambda} \approx \sqrt{2} \frac{\lambda_{\text{ex}}\lambda_{\text{em}}}{\sqrt{\lambda_{\text{ex}}^2 + \lambda_{\text{em}}^2}} \quad (\text{III.7})$$

The smaller the pinhole is set, the better is the achieved resolution. However, if the pinhole is set too small, the actual light intensity reaching the detector is too low for a successful imaging process. For very small pinhole widths, the resolution limit can be determined in axial and lateral direction (represented by the full widths at half maximum $FWHM_{\text{axial}}$ and $FWHM_{\text{lateral}}$)

$$FWHM_{\text{axial}} = \frac{0.64\bar{\lambda}}{n - \sqrt{n^2 - NA^2}} \quad (\text{III.8})$$

$$FWHM_{\text{lateral}} = 0.37 \frac{\bar{\lambda}}{NA} \quad (\text{III.9})$$

where n is the refractive index of the immersion medium. Using the optical conditions applied in this work ($\lambda_{\text{ex}} = 488 \text{ nm}$, $\lambda_{\text{em}} = 503 \text{ nm}$, $n = 1.4582$, $NA = 1.3$), Eq. (III.8) provides $FWHM_{\text{axial}}$

= 397 nm and Eq. (III.9) provides $FWHM_{\text{lateral}} = 141$ nm. For practical reasons, the pinhole is set to 0.5 AU resulting in a slight loss of resolution and small mismatches in the optical setup can prevent to reach the theoretical resolution limit. The required resolution for a successful imaging process depends on the smallest feature size. In the case of packed beds, this is the interparticle pore space. The characteristic size of interparticle channels was estimated by Giddings as a third of the mean particle diameter d_p [45]. For the 1.3 μm and 1.9 μm particles investigated here, this corresponds to a characteristic channel width of ~ 430 nm and ~ 633 nm showing that the resolution limit of the instrument is reached, especially for the smaller 1.3 μm particles. High quality of the reconstructions of the acquired images is ensured by an image restoration process, in particular resolution enhancement based on a deconvolution procedure, and utilization of the known feature shape in form of spherical particles through a fitting procedure (detailed descriptions of the restoration and reconstruction processes can be found in [29,56] and in Chapters 1 and 3).

For structures with smaller characteristic sizes, especially with irregular feature shapes, the CLSM method has been developed further to achieve higher resolution. Hell and co-workers developed the stimulated emission depletion microscopy (STED) [57,58] breaking Abbe's diffraction resolution limit [59] which was honoured by the Nobel Prize in Chemistry in 2014. They introduced a second laser into the CLSM setup at another wavelength which is focused around the point illuminated by the excitation laser to induce deactivation of the fluorophores. As a result, the excitation volume is significantly smaller than in a conventional CLSM. An even further improvement was achieved by combining STED with 4Pi microscopy (illumination from two different angles resulting in improvement of the axial resolution to values typical for lateral resolution) [60].

III.3.2 FIB-SEM

Focussed ion beam scanning electron microscopy is a 3D imaging method based on the combination of cutting by ion beam and imaging by electron microscopy. Compared to CLSM, FIB-SEM is not limited to optically transparent materials and achieves higher resolution but requires more complex sample preparation and longer imaging times. While focused ion beams are used in material science since the 1980s, dual beam instruments combining the ion beam with an electron beam were reported first around 2000 [61,62]. During the following years, the utilization in 3D structure analysis started for biological samples [63] and metal alloys [64]. For most samples, the volume of interest is excavated prior to the imaging process to avoid shadowing effects by surrounding structure and to avoid re-deposition of removed material on the fresh surface. In addition, the top surface of the volume of interest is typically covered with a layer of a highly conductive element (e.g., platinum or carbon) by beam supported deposition to protect it from beam damage and increase the system stability. A schematic of the beam geometry during imaging of such an excavated volume is shown in Fig. III.3. The crucial feature is the tilt between the ion beam and the electron beam (a typical tilt angle is 52°) during the imaging process allowing fast transitions between cutting and imaging. The ion beam is used to remove the volume of interest layer-by-layer starting from the front surface. After removal of each layer, the new front surface is imaged using the electron beam. It should be noted that

both beams can play further roles. The ion beam can also be used for image acquisition (with limited resolution) as often used for drift correction during stack acquisition and the electron beam can also be used for (very slow and fine) cutting or material deposition. Minimum slice thicknesses of approximately 10 nm can be achieved while the SEM detection can typically achieve resolutions down to 1 nm [54]. Typically imaged volumes span over a range of (1–100 μm)³ whereas the resolution should be reduced for large volumes to keep reasonable imaging times and to reduce artefacts due to instrument drift during cutting and imaging of individual slices. Depending on the instrument, the imaging of larger volumes is possible but might require splitting into multiple sub-stacks (as adapted in Chapter 4).

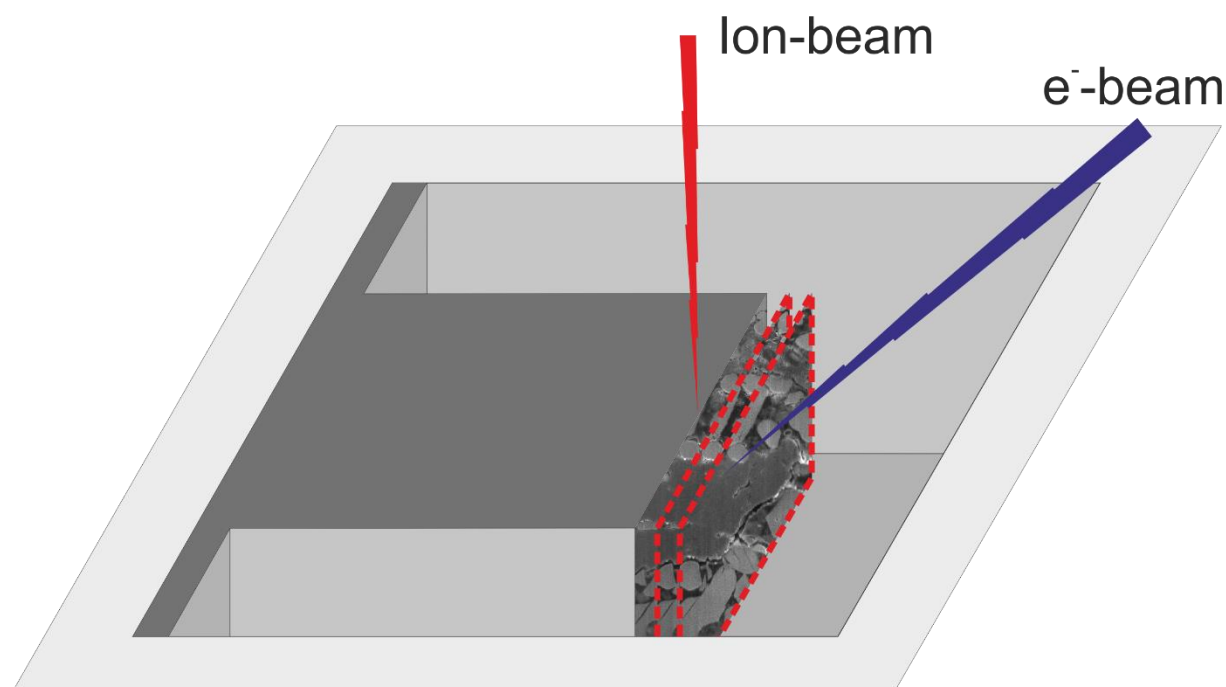


Fig. III.3: Schematic of a focussed ion beam scanning electron microscope during stack acquisition. The darker section of the top surface represents the protective layer of platinum or carbon. The ion beam is used to remove slices of the front surface of the sample and the electron beam is used to acquire images of the surface between cuts.

FIB-SEM has already been used for porous silica materials for chromatographic separations by Stoeckel et al. in the case of silica monoliths [65,66]. This method could be adapted for the packed column type as well, since it provides stabilization of the bed structure with a divinylbenzene based polymer and fills the pore space with solid phase. Complete pore filling is crucial for achieving high quality reconstruction as residual void space (especially in materials with low electric conductivity) results in charging artefacts, background illumination, and can induce significant beam shift. Electron contrast between the organic polymer and the silica is sufficient to allow successful imaging. If a material does not provide enough electron contrast compared to a standard polymer, different approaches can be utilized. Negative staining uses a high-contrast filling agent, e.g., silicon polymers provide intermediate contrast between carbon materials and metal oxides [67]. The opposite approach is used during positive

staining where a high-contrast agent is deposited onto the surface of the material prior to pore filling with the low-contrast polymer, e.g., tetraphenyllead [68] or ruthenium tetroxide [69].

References

- [1] T. Müllner, K.K. Unger, U. Tallarek, Characterization of microscopic disorder in reconstructed porous materials and assessment of mass transport-relevant structural descriptors, *New J. Chem.* 40 (2016) 3993–4015.
- [2] K. Hormann, T. Müllner, S. Bruns, A. Höltzel, U. Tallarek, Morphology and separation efficiency of a new generation of analytical silica monoliths, *J. Chromatogr. A* 1222 (2012) 46–58.
- [3] D. Hlushkou, K. Hormann, A. Höltzel, S. Khirevich, A. Seidel-Morgenstern, U. Tallarek, Comparison of first and second generation analytical silica monoliths by pore-scale simulations of eddy dispersion in the bulk region, *J. Chromatogr. A* 1303 (2013) 28–38.
- [4] D. Enke, R. Gläser, U. Tallarek, Sol-Gel and Porous Glass-Based Silica Monoliths with Hierarchical Pore Structure for Solid-Liquid Catalysis, *Chem. Ing. Tech.* 88 (2016) 1561–1585.
- [5] M. Ferré, R. Pleixats, M. Wong Chi Man, X. Cattoën, Recyclable organocatalysts based on hybrid silicas, *Green Chem.* 18 (2016) 881–922.
- [6] L. Wang, W. Ding, Y. Sun, The preparation and application of mesoporous materials for energy storage, *Mater. Res. Bull.* 83 (2016) 230–249.
- [7] A.A. Olajire, Synthesis of bare and functionalized porous adsorbent materials for CO₂ capture, *Greenh. Gases Sci. Technol.* 7 (2017) 399–459.
- [8] J.B. Cook, H.-S. Kim, T.C. Lin, S. Robbennolt, E. Detsi, B.S. Dunn, et al., Tuning porosity and surface area in mesoporous silicon for application in Li-ion battery electrodes, *ACS Appl. Mater. Interfaces* 9 (2017) 19063–19073.
- [9] T. Qian, J. Li, Y. Deng, Flower-like hollow porous silica sphere for high-temperature thermal storage, *Appl. Therm. Eng.* 106 (2016) 423–426.
- [10] F. Gritti, G. Guiochon, The current revolution in column technology: How it began, where is it going? *J. Chromatogr. A* 1228 (2012) 2–19.
- [11] F. Gritti, G. Guiochon, Perspectives on the Evolution of the Column Efficiency in Liquid Chromatography, *Anal. Chem.* 85 (2013) 3017–3035.
- [12] C.G. Horvath, B.A. Preiss, S.R. Lipsky, Fast liquid chromatography: an investigation of operating parameters and the separation of nucleotides on pellicular ion exchangers, *Anal. Chem.* 39 (1967) 1422–1428.
- [13] E. Shishkova, A.S. Hebert, J.J. Coon, Now, more than ever, proteomics needs better chromatography, *Cell Syst.* 3 (2016) 321–324.
- [14] J.J. DeStefano, S.A. Schuster, J.M. Lawhorn, J.J. Kirkland, Performance characteristics of new superficially porous particles, *J. Chromatogr. A* 1258 (2012) 76–83.
- [15] A. de Villiers, H. Lauer, R. Szucs, S. Goodall, P. Sandra, Influence of frictional heating on temperature gradients in ultra-high-pressure liquid chromatography on 2.1 mm I.D. columns, *J. Chromatogr. A* 1113 (2006) 84–91.
- [16] F. Gritti, M. Martin, G. Guiochon, Influence of viscous friction heating on the efficiency of columns operated under very high pressures, *Anal. Chem.* 81 (2009) 3365–3384.
- [17] J.J. DeStefano, B.E. Boyes, S.A. Schuster, W.L. Miles, J.J. Kirkland, Are sub-2 μm particles best for separating small molecules? An alternative, *J. Chromatogr. A* 1368 (2014) 163–172.

-
- [18] F. Xie, R.D. Smith, Y. Shen, Advanced proteomic liquid chromatography, *J. Chromatogr. A* 1261 (2012) 78–90.
- [19] G. Guiochon, Monolithic columns in high-performance liquid chromatography, *J. Chromatogr. A* 1168 (2007) 101–168.
- [20] G. Guiochon, F. Gritti, Shell particles, trials, tribulations and triumphs, *J. Chromatogr. A* 1218 (2011) 1915–1938.
- [21] J.J. Kirkland, J.J. DeStefano, The art and science of forming packed analytical high-performance liquid chromatography columns, *J. Chromatogr. A* 1126 (2006) 50–57.
- [22] B.G. Yew, E.C. Drumm, G. Guiochon, Mechanics of column beds: I. Acquisition of the relevant parameters, *AIChE J.* 49 (2003) 626–641.
- [23] B.G. Yew, J. Ureta, R.A. Shalliker, E.C. Drumm, G. Guiochon, Mechanics of column beds: II. Modeling of coupled stress-strain-flow behavior, *AIChE J.* 49 (2003) 642–664.
- [24] J.P.C. Vissers, H.A. Claessens, J. Laven, C.A. Cramers, Colloid Chemical Aspects of Slurry Packing Techniques in Microcolumn Liquid Chromatography, *Anal. Chem.* 67 (1995) 2103–2109.
- [25] J.P.C. Vissers, M.A. Hoeben, J. Laven, H.A. Claessens, C.A. Cramers, Hydrodynamic aspects of slurry packing processes in microcolumn liquid chromatography, *J. Chromatogr. A* 883 (2000) 11–25.
- [26] M.F. Wahab, C.A. Pohl, C.A. Lucy, Colloidal aspects and packing behaviour of charged microparticulates in high efficiency ion chromatography, *J. Chromatogr. A* 1270 (2012) 139–146.
- [27] S. Jung, A. Hölzel, S. Ehlert, J.A. Mora, K. Kraiczek, M. Dittmann, et al., Impact of conduit geometry on the performance of typical particulate microchip packings, *Anal. Chem.* 81 (2009) 10193–10200.
- [28] S. Khirevich, A. Hölzel, S. Ehlert, A. Seidel-Morgenstern, U. Tallarek, Large-scale simulation of flow and transport in reconstructed HPLC-microchip packings, *Anal. Chem.* 81 (2009) 4937–4945.
- [29] S. Bruns, U. Tallarek, Physical reconstruction of packed beds and their morphological analysis: Core-shell packings as an example, *J. Chromatogr. A* 1218 (2011) 1849–1860.
- [30] J.W. Jorgenson, Capillary liquid chromatography at ultrahigh pressures, *Annu. Rev. Anal. Chem.* 3 (2010) 129–150.
- [31] S. Bruns, D. Stoeckel, B.M. Smarsly, U. Tallarek, Influence of particle properties on the wall region in packed capillaries, *J. Chromatogr. A* 1268 (2012) 53–63.
- [32] S. Bruns, J.P. Grinias, L.E. Blue, J.W. Jorgenson, U. Tallarek, Morphology and separation efficiency of low-aspect-ratio capillary ultrahigh pressure liquid chromatography columns, *Anal. Chem.* 84 (2012) 4496–4503.
- [33] S. Bruns, E.G. Franklin, J.P. Grinias, J.M. Godinho, J.W. Jorgenson, U. Tallarek, Slurry concentration effects on the bed morphology and separation efficiency of capillaries packed with sub-2 μm particles, *J. Chromatogr. A* 1318 (2013) 189–197.
- [34] J.H. Knox, G.R. Laird, P.A. Raven, Interaction of radial and axial dispersion in liquid chromatography in relation to the “infinite diameter effect,” *J. Chromatogr. A* 122 (1976) 129–145.
- [35] J.E. Baur, E.W. Kristensen, R.M. Wightman, Radial dispersion from commercial high-performance liquid chromatography columns investigated with microvoltammetric electrodes., *Anal. Chem.* 60 (1988) 2334–2338.
- [36] T. Farkas, J.Q. Chambers, G. Guiochon, Column efficiency and radial homogeneity in liquid chromatography, *J. Chromatogr. A* 679 (1994) 231–245.
- [37] T. Farkas, G. Guiochon, Contribution of the radial distribution of the flow velocity to
-

- band broadening in HPLC columns, *Anal. Chem.* 69 (1997) 4592–4600.
- [38] R.A. Shalliker, B.S. Broyles, G. Guiochon, Physical evidence of two wall effects in liquid chromatography, *J. Chromatogr. A* 888 (2000) 1–12.
- [39] J.J. van Deemter, F.J. Zuiderweg, A. Klinkenberg, Longitudinal diffusion and resistance to mass transfer as causes of nonideality in chromatography, *Chem. Eng. Sci.* 5 (1956) 271–289.
- [40] L. Lapidus, N.R. Amundson, Mathematics of adsorption in beds VI. The effect of longitudinal diffusion in ion exchange and chromatographic columns, *J. Phys. Chem.* 56 (1952) 984–988.
- [41] A.J.P. Martin, R.L.M. Synge, A new form of chromatogram employing two liquid phases, *Biochem. J.* 35 (1941) 1358–1368.
- [42] T.J. Kaiser, J.W. Thompson, J.S. Mellors, J.W. Jorgenson, Capillary-based instrument for the simultaneous measurement of solution viscosity and solute diffusion coefficient at pressures up to 2000 bar and implications for ultrahigh pressure liquid chromatography, *Anal. Chem.* 81 (2009) 2860–2868.
- [43] F. Gritti, G. Guiochon, The van Deemter equation: assumptions, limits, and adjustment to modern high performance liquid chromatography, *J. Chromatogr. A* 1302 (2013) 1–13.
- [44] F. Gritti, G. Guiochon, Perspectives on the evolution of the column efficiency in liquid chromatography, *Anal. Chem.* 85 (2013) 3017–3035.
- [45] J.C. Giddings, Dynamics of chromatography, Part 1: Principles and Theory, Marcel Dekker, New York, 1965.
- [46] F. Gritti, G. Guiochon, General HETP equation for the study of mass-transfer mechanisms in RPLC, *Anal. Chem.* 78 (2006) 5329–5347.
- [47] J.C. Giddings, P.D. Schettler, General nonequilibrium theory of chromatography with complex flow transport, *J. Phys. Chem.* 73 (1969) 2577–2582.
- [48] A. Daneyko, D. Hlushkou, V. Baranau, S. Khirevich, A. Seidel-Morgenstern, U. Tallarek, Computational investigation of longitudinal diffusion, eddy dispersion, and trans-particle mass transfer in bulk, random packings of core-shell particles with varied shell thickness and shell diffusion coefficient, *J. Chromatogr. A* 1407 (2015) 139–156.
- [49] S. Khirevich, A. Höltzel, A. Seidel-Morgenstern, U. Tallarek, Time and length scales of eddy dispersion in chromatographic beds, *Anal. Chem.* 81 (2009) 7057–7066.
- [50] A. Daneyko, S. Khirevich, A. Höltzel, A. Seidel-Morgenstern, U. Tallarek, From random sphere packings to regular pillar arrays: effect of the macroscopic confinement on hydrodynamic dispersion, *J. Chromatogr. A* 1218 (2011) 8231–8248.
- [51] P. Levitz, Toolbox for 3D imaging and modeling of porous media: Relationship with transport properties, *Cem. Concr. Res.* 37 (2007) 351–359.
- [52] Z. Saghi, P.A. Midgley, Electron tomography in the (S)TEM: from nanoscale morphological analysis to 3D atomic imaging, *Annu. Rev. Mater. Res.* 42 (2012) 59–79.
- [53] O. Ersen, I. Florea, C. Hirlimann, C. Pham-Huu, Exploring nanomaterials with 3D electron microscopy, *Mater. Today* 18 (2015) 395–408.
- [54] M.D. Uchic, L. Holzer, B.J. Inkson, E.L. Principe, P. Munroe, Three-dimensional microstructural characterization using focused ion beam tomography, *MRS Bull.* 32 (2007) 408–416.
- [55] S. Bruns, Dreidimensionale Rekonstruktion monolithischer Festphasen mittels konfokaler Lasermikroskopie, Dissertation (2009), Philipps-Universität Marburg, Germany.
- [56] S. Bruns, T. Müllner, M. Kollmann, J. Schachtner, A. Höltzel, U. Tallarek, Confocal

- laser scanning microscopy method for quantitative characterization of silica monolith morphology, *Anal. Chem.* 82 (2010) 6569–6575.
- [57] S.W. Hell, J. Wichmann, Breaking the diffraction resolution limit by stimulated emission: stimulated-emission-depletion fluorescence microscopy, *Opt. Lett.* 19 (1994) 780–782.
- [58] T.A. Klar, E. Engel, S.W. Hell, Breaking Abbe's diffraction resolution limit in fluorescence microscopy with stimulated emission depletion beams of various shapes, *Phys. Rev. E* 64 (2001) 66613.
- [59] E. Abbe, Beiträge zur Theorie des Mikroskops und der mikroskopischen Wahrnehmung., *Arch. F. Mikrosk. Anat.* 9 (1873) 413–468.
- [60] M. Dyba, S.W. Hell, Focal Spots of Size $\lambda/23$ Open Up Far-Field Fluorescence Microscopy at 33 nm Axial Resolution, *Phys. Rev. Lett.* 88 (2002) 163901.
- [61] R. Krueger, Dual-column (FIB-SEM) wafer applications, *Micron* 30 (1999) 221–226.
- [62] V.G.M. Sivel, J. Van Den Brand, W.R. Wang, H. Mohdadi, F.D. Tichelaar, P.F.A. Alkemade, et al., Application of the dual-beam FIB/SEM to metals research, *J. Microsc.* 214 (2004) 237–245.
- [63] W. Denk, H. Horstmann, Serial block-face scanning electron microscopy to reconstruct three-dimensional tissue nanostructure, *PLoS Biol.* 2 (2004) 1900–1909.
- [64] M.D. Uchic, M.A. Groeber, D.M. Dimiduk, J.P. Simmons, 3D microstructural characterization of nickel superalloys via serial-sectioning using a dual beam FIB-SEM, *Scr. Mater.* 55 (2006) 23–28.
- [65] D. Stoeckel, C. Kübel, K. Hormann, A. Höltzel, B.M. Smarsly, U. Tallarek, Morphological analysis of disordered macroporous-mesoporous solids based on physical reconstruction by nanoscale tomography, *Langmuir* 30 (2014) 9022–9027.
- [66] D. Stoeckel, C. Kübel, M.O. Loeh, B.M. Smarsly, U. Tallarek, Morphological analysis of physically reconstructed silica monoliths with submicrometer macropores: effect of decreasing domain size on structural homogeneity, *Langmuir* 31 (2015) 7391–7400.
- [67] Z. Liu, Y.K. Chen-Wiegart, J. Wang, S.A. Barnett, K.T. Faber, Three-phase 3D reconstruction of a LiCoO₂ cathode via FIB-SEM tomography, *Microsc. Microanal.* 22 (2016) 140–148.
- [68] T. Müllner, A. Zankel, C. Mayrhofer, A. Höltzel, Y. Lv, F. Svec, et al., Reconstruction and characterization of polymer-based monolithic stationary phases using serial block-face scanning electron microscopy, *Langmuir* 28 (2012) 16733–16737.
- [69] T. Müllner, A. Zankel, A. Höltzel, F. Svec, U. Tallarek, Morphological properties of methacrylate-based polymer monoliths: from gel porosity to macroscopic inhomogeneities, *Langmuir* 33 (2017) 2205–2214.

Chapter 1

Larger voids in mechanically stable, loose packings of 1.3 μm frictional, cohesive particles: Their reconstruction, statistical analysis, and impact on separation efficiency

Authors

Arved E. Reising, Justin M. Godinho, Kristof Hormann, James W. Jorgenson, and Ulrich Tallarek

State of publication

Published 30 January 2016 in *Journal of Chromatography A*, Vol. 1436, pp. 118–132.

Abstract

Lateral transcolumn heterogeneities and the presence of larger voids in a packing (comparable to the particle size) can limit the preparation of efficient chromatographic columns. Optimizing and understanding the packing process provides keys to better packing structures and column performance. Here, we investigate the slurry-packing process for a set of capillary columns packed with C18-modified, 1.3 μm bridged-ethyl hybrid porous silica particles. The slurry concentration used for packing 75 μm i.d. fused-silica capillaries was increased gradually from 5 to 50 mg/mL. An intermediate concentration (20 mg/mL) resulted in the best separation efficiency. Three capillaries from the set representing low, intermediate, and high slurry concentrations were further used for three-dimensional bed reconstruction by confocal laser scanning microscopy and morphological analysis of the bed structure. Previous studies suggest increased slurry concentrations will result in higher column efficiency due to the suppression of transcolumn bed heterogeneities, but only up to a critical concentration. Too concentrated slurries favour the formation of larger packing voids (reaching the size of the average particle diameter). Especially large voids, which can accommodate particles from >90% of the particle size distribution, are responsible for a decrease in column efficiency at high slurry concentrations. Our work illuminates the increasing difficulty of achieving high bed densities with small, frictional, cohesive particles. As particle size decreases interparticle forces become increasingly important and hinder the ease of particle sliding during column packing. While an optimal slurry concentration is identified with respect to bed morphology and separation efficiency under conditions in this work, our results suggest adjustments of this concentration are required with regard to particle size, surface roughness, column dimensions, slurry liquid, and external effects utilized during the packing process (pressure protocol, ultrasound, electric fields).

1.1 Introduction

The reduction of the mean particle size in packed columns is a consistent goal in liquid chromatography because the minimum plate height and overall column efficiency (plates per meter) scale with the particle diameter [1] (as long as the packing structure and bed homogeneity are conserved independently from the particle size). For example, capillary columns packed with sub-2 μm particles achieve theoretical plate numbers of $\sim 500,000$ per meter, with peak capacities up to 1500 [1,2]. They are of special interest in separations of complex biological samples, where high resolution between analytes is desired before detection. Nevertheless, the use of ever smaller particles amplifies several problems, including extra-column band broadening [3], frictional heating [4–6], back-pressure [7], and radial expansion of the column under high pressure [8]. Further, the reduced particle diameter and the increased back-pressure present major challenges to the formation of a uniform bed structure, with a major contribution to the packed bed's separation efficiency originating from transcolumn heterogeneities introduced during the packing process [7,9]. Gritti and Guiochon [10] estimated that transcolumn dispersion induced by heterogeneities across the column diameter makes up to 70% of the total dispersion for analytical ultrahigh-pressure liquid chromatography (UHPLC) columns. Differences in bed morphology between the column wall region and the bulk packed bed are a main factor [5,11–15].

The work of Shalliker et al. [12], which holds evidence for two different wall effects in chromatographic columns, describes the situation well. The geometrical wall effect caused by the first (~ 5) layers of particles adjacent to the wall is characterized by higher than average external porosity due to ordered packing, since the particles can only touch the wall but not penetrate it. The first particle layer at the wall is a highly ordered monolayer, followed by more imperfect layers with decreasing order until a random particle arrangement is reached. As a result, the local external porosity directly at the column wall tends towards unity, reaches a minimum after approximately a particle radius from the wall, and oscillates over a few particle diameters (d_p) towards the average value found in the column centre (bulk packing region). This packing induces an oscillating radial flow velocity profile in this region [14], with locally higher velocities at radial positions where porosity is increased. This results in an overall higher average flow velocity in this wall region than in the bulk packing region. These macroscopic (wall-to-wall) morphological and velocity heterogeneities result in transcolumn dispersion [13–15]. The second wall effect begins at a radial coordinate $>5 d_p$ from the wall and is due to radial stress exerting forces on the particles against the wall and the friction between the bed and the column wall during the packing process [12,16]. It results in a denser packed intermediate region of $\sim 50 d_p$ from the column wall towards the column centre. Since the capillary columns in the current work have a diameter of $\sim 58 d_p$ (column inner diameter: 75 μm ; average particle diameter, $d_p = 1.3 \mu\text{m}$), their transcolumn bed morphology is affected mostly by the geometrical wall effect.

The formation of a homogeneous bed from pore to transcolumn scale is a key behind efficient chromatography. It was only during the last years that the search for the optimal packing

conditions started to be based on a more detailed understanding of the process itself [12,17–23], in addition to purely empirical optimization. Many parameters influence the packing process and final bed structure. Recent work from our groups addressed experimentally the effects of particle properties such as the width of the particle size distribution (PSD) and the surface roughness [24], different capillary column diameters [25], and conduit geometry in HPLC microchips [26,27] on separation efficiency. Importantly, the chromatographic performance of these packed columns was complemented with the three-dimensional (3D) physical reconstruction [24,25] or simulation [13–15,27] of packing microstructures followed by a detailed analysis of relevant morphological features and resulting (experimental and/or simulated) transport properties.

Nowadays, a portfolio of techniques is available for detailed investigation of the 3D morphology in macroporous–mesoporous chromatographic supports such as packed beds of small mesoporous particles or silica-based and polymeric monoliths. This portfolio [28–34] includes confocal laser scanning microscopy (CLSM) [35], focused ion-beam scanning electron microscopy (FIB-SEM) [36], and serial block-face scanning SEM (SBF-SEM) [37] for the reconstruction of the interstitial macropore space in packed beds [24,25,38] and monoliths [39–44], and scanning transmission electron microscopy (STEM) [45,46] for the reconstruction of the intraparticle or intraskeleton mesopore space [47–50].

Our recent work on establishing morphology–transport relationships for supports used in liquid chromatography has elucidated, for example, the sample volume that actually needs to be reconstructed for a meaningful morphological description [51], has resolved systematic radial variations in the macropore space morphology of packed columns and monoliths to correlate them with particle properties [24,25] or the monolith preparation protocol [43,52], has quantified heterogeneity length scales and structural correlations in these materials [52,53], or has analysed geometrical and topological parameters in silica monoliths to detect changes as their domain size is reduced to submicrometre dimension [52,54,55]. For packed capillary columns, our previous work [24,25] has correlated experimentally observed differences in column efficiency to particle size segregation and bed structural changes in the wall region (mostly, average packing density). Assuming particle properties including surface roughness or the PSD are insignificant, column efficiency is dominated by transcolumn dispersion, i.e., by how well the critical issue of the wall region (local bed density and homogeneity governing fluid flow and dispersion) has been resolved with respect to the bulk packing structure.

In a subsequent study [56], we noticed the importance of the slurry concentration (regarding the final bed morphology) in column packing for three sets of columns, each including one column packed with a low slurry concentration and one packed with a higher concentration. The column packed with a higher concentration showed better efficiency for all three types of particles, i.e., fully porous 1.7 and 1.9 μm bridged-ethyl hybrid (BEH) particles and 1.9 μm Kinetex core-shell particles. We observed that the BEH particles (with a relative standard deviation of their PSD of 12–16%) favoured size segregation at low slurry concentrations, while it was suppressed at higher concentrations. Further, with high slurry concentrations, there was a clear increase in the number of larger voids in the bed structure, which can have a dramatic effect on column efficiency, as illustrated by Schure and Maier [57] with dispersion simulations

in defective packings. They concluded that it is far more important in column packing to prevent defect sites, e.g., larger voids or even gaps, leading to inhomogeneous packing rather than obtaining the highest packing density. For core-shell particles (Kinetex), a slight densification in the wall region was observed at higher slurry concentration, but the number of larger voids showed only a very small increase [56]. Based on these observations, we proposed the operation of two antagonizing effects as the slurry concentration is increased from low to high values: the first one reduces wall effects at higher slurry concentration, which reduces transcolumn bed heterogeneities and associated dispersion; the second one increases the number of larger voids in the bed, which increases chromatographic band broadening. This suggests an intermediate slurry concentration would result in the best performance, that is, with only weak wall effects and yet no critical amount of larger voids.

To test this hypothesis we prepared a set of capillary columns with a series of increasing slurry concentrations. Nine columns having 75 μm i.d. were packed using fully porous 1.3 μm C18 BEH particles at slurry concentrations from 5 to 50 mg/mL. Each column was characterized regarding separation efficiency and three capillary columns representing low, intermediate, and high slurry concentrations were reconstructed three-dimensionally using CLSM for analysis of their efficiency limiting morphological features. The analysis focused on transcolumn heterogeneities as well as the occurrence of larger voids in the bed structure. The purpose of this work is not to conclude definitively on the absolute effect of slurry concentration on bed morphologies. Instead we seek to give description of morphological heterogeneities formed as a function of the slurry concentration, with general implications for column packing.

1.2 Experimental

1.2.1 Chemicals and materials

75 μm i.d. cylindrical fused-silica tubing was purchased from Polymicro Technologies (Phoenix, AZ). The capillaries were packed with C18-modified 1.3 μm BEH particles provided by Waters Corporation (Milford, MA). HPLC grade acetonitrile, acetone (reagent grade), trifluoroacetic acid (TFA), and the test analytes for chromatographic characterization (L-ascorbic acid, hydroquinone, resorcinol, catechol, 4-methyl catechol) were obtained from Fisher Scientific (St. Louis, MO). Kasil frits for the packed capillaries were prepared with potassium silicate from PQ Corporation (Valley Forge, PA) and formamide from Sigma-Aldrich (St. Louis, MO). HPLC grade water for chromatographic experiments was obtained from a Millipore NANOpure water system (Billerica, MA). HPLC grade acetone (staining solvent) was supplied by Fisher Scientific (Loughborough, UK). The fluorescent dye Bodipy 493/503 (Life Technologies, Darmstadt, Germany) was used for staining prior to imaging. Glycerol and dimethylsulfoxide (DMSO) employed for matching the liquid's refractive index to that of the BEH particles were purchased from Carl Roth (Karlsruhe, Germany). HPLC grade water used during refractive index matching came from a Milli-Q gradient purification system (Merck Millipore, Darmstadt, Germany). "Type 0" coverslips were obtained from Gerhard Menzel (Braunschweig, Germany).

1.2.2 Preparation of capillary UHPLC columns

Preparation of the capillary UHPLC columns will be briefly described here and has been described previously in detail [58–62]. Column blanks were fritted using the Kasil method [63]. Here, the capillary tubing was pushed onto a glass microfiber filter (Reeve Angel, Clifton, NJ) wetted with 50/50 (v/v) potassium silicate/formamide. The column blanks were then dried overnight at 50 °C. Slurries with a specific concentration were prepared by mixing a known mass of the particles in a known volume of acetone. The particles were suspended with a 10 min sonication cycle prior to packing using a Cole Parmer Ultrasonic Cleaner 8891 (Vernon Hills, IL).

The slurry was then placed into a packing reservoir and the column blank was secured to the reservoir using an UHPLC fitting. Packing was initiated using acetone as a pushing solvent at 150 bar from a DSHF-300 Haskel pump (Burbank, CA). The packing pressure was increased with a rate of 475 bar per centimetre of packed bed until a final pressure of 2000 bar was reached. The column was allowed to pack until a 38 cm bed length was reached. Then, the packing pressure was slowly released to atmospheric pressure. The column was then connected to a DSXHF-903 Haskel pump (Burbank, CA) using an UHPLC injection apparatus. Each column was flushed for 1 h in 50/50 (v/v) water/acetonitrile with 0.1% TFA at 3500 bar, after which the pressure was gradually released and reinitiated at 700 bar to form a temporary inlet frit with a heated wire stripper from Teledyne Interconnect Devices (San Diego, CA). Columns were then clipped to a ~34 cm bed length and an inlet frit was installed using the Kasil method.

1.2.3 Chromatographic analysis

Column efficiency was tested under isocratic elution conditions using 200 μM of a test mixture (L-ascorbic acid, dead-time marker; hydroquinone, resorcinol, catechol, and 4-methyl catechol) and an UHPLC injection apparatus [58–62]. The mobile phase used for evaluation was 50/50 (v/v) water/acetonitrile with 0.1% TFA. Analytes were detected amperometrically. Electrochemical detection was conducted at an $8 \mu\text{m} \times 300 \mu\text{m}$ carbon fibre microelectrode held at +1.1 V vs. Ag/AgCl reference electrode [64]. This electrode was placed at the outlet of the UHPLC column. Current-to-voltage conversion was conducted using an SR750 current amplifier (Stanford Research Systems, Sunnyvale, CA) with a 10^9 V/A gain and a 3 Hz, 3 dB low-pass bandwidth filter. An Intel Core 2 Duo desktop computer with a 16-bit A/D converter was used to acquire data at 21 Hz. Data were collected with a custom written LabView 6.0 program (National Instruments, Austin, TX).

Columns were analysed over a range of mobile phase velocities to create plots of the plate height H vs. the average mobile phase velocity u_{av} for each analyte in the test mixture. High frequency noise was removed from the chromatograms using a digital frequency filter and low frequency baseline drift was eliminated by background subtraction. Retention times and theoretical plate counts N were determined using an iterative statistical moments algorithm written in Igor Pro 6.0 (Wavemetrics, Inc., Lake Oswego, OR) [65]. Briefly, the program eliminates operator bias by arbitrarily defining the beginning and end of each peak and an iterative marking process is used to mark the limits of integration. The program uses these

values to calculate the first and second central moment. From the second central moment a standard deviation is obtained. Using this value the peak is then marked for $\pm 3\sigma$ from the first moment. The program then calculates new values for the second moment and the standard deviation. If the value of the second moment differs by more than 1% the process is reiterated using the new standard deviation to mark $\pm 3\sigma$ from the peak centre. The process continues until the change in variance is less than 1%. The final values for the moments are then used to calculate N .

1.2.4 Imaging of packing microstructure

Detection windows were created at a distance of 10 cm from the column inlet using a drop of warm sulphuric acid. Columns were flushed with several column volumes of the dye solution in acetone (0.5 mg/mL) to achieve staining of the reversed-phase surface of the particles with the fluorescent dye Bodipy 493/503. Afterwards, the columns were flushed for several hours with refractive index matching liquid, i.e., 70/19/11 (v/v/v) glycerol/DMSO/water, calibrated to a refractive index of $n_D = 1.4582$ using an AR200 digital refractometer (Reichert Analytical Instruments, Depew, NY). Columns were fixed on a microscope slide and transferred to the confocal microscope, a TCS SP5 equipped with a HCX PLAPO 63 \times /1.3 GLYC CORR CS (21 $^\circ$) glycerol immersion objective lens (Leica Microsystems, Wetzlar, Germany). The refractive index matching liquid was used as an embedding medium for the capillaries and as lens immersion medium. The optical setup has been described in detail before [38].

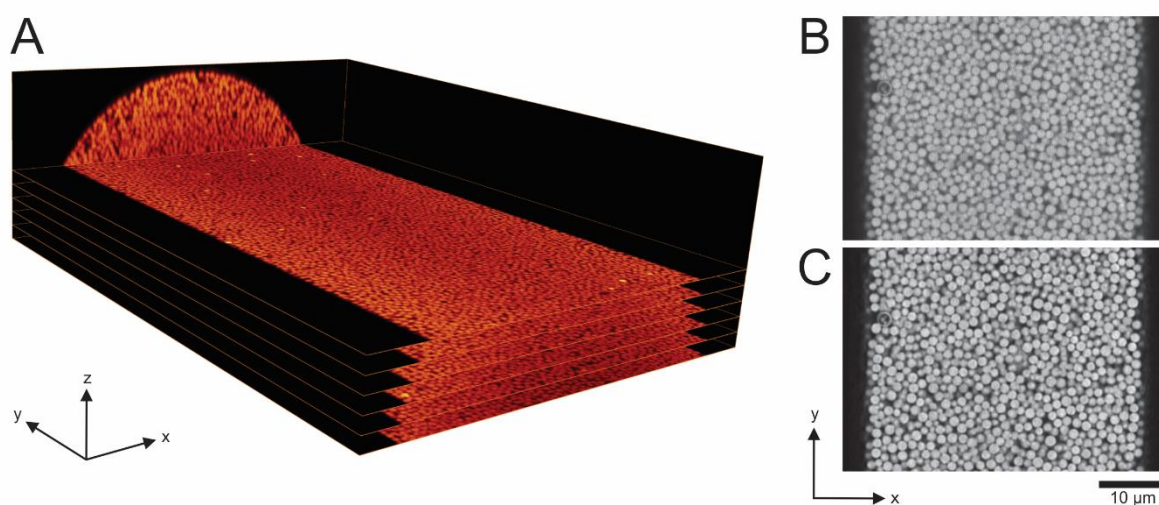


Figure 1.1. Image acquisition and enhancement. (A) Orthoslice view of the raw CLSM images recorded from a 75 μm i.d. capillary column packed with 1.3 μm C18 BEH particles at a slurry concentration of $c_{\text{slurry}} = 10 \text{ mg/mL}$. 307 xy -slices were taken from the top of the stack to the centre of the column. Six of these slices from the column centre towards the column top are shown at a distance of 25 slices (or 3.15 μm). (B, C) Exemplary xy -images of a 75 μm i.d. capillary packed with the 1.3 μm particles at a slurry concentration of $c_{\text{slurry}} = 20 \text{ mg/mL}$ before (B) and after image restoration (C).

Excitation of adsorbed dye was achieved with an Argon laser at 488 nm. The microscope pinhole was set to 0.5 AU. The detection interval was set from 491 to 515 nm. Image slices were acquired perpendicular to the capillary axis, from the top of the column towards the centre. The pixel size within a slice was set to 30 nm and the step size to 126 nm, both complying with the Nyquist sampling criterion. An exemplary orthoslice view from the capillary column packed with a slurry concentration of $c_{\text{slurry}} = 10 \text{ mg/mL}$ is given in Fig. 1.1A, where also the x -, y -, and z -axis are defined as used in the remainder of the discussion.

1.2.5 Image restoration and bed reconstruction

Image quality of the raw images from the microscope was enhanced in several steps. If not stated otherwise, custom-written software was used (written in C# using Microsoft Visual Studio 2008, 2012, and 2013, Microsoft Corporation, Redmond, WA). The following steps were applied for image restoration:

1. Poisson noise was corrected using the PureDenoise plugin for ImageJ [66,67].
2. Intensity variations in an image slice due to different material thickness above the slice at different positions were corrected. A fourth-order polynomial fit was applied to the mean intensity values along the x -axis and used to normalize intensity in the slice.
3. Bleaching of the dye and intensity loss with increasing measurement depth were corrected using a second-order exponential decay for mean intensities in the center of every slice.
4. A deconvolution process was applied to increase contrast and resolution using the Huygens maximum likelihood iterative deconvolution (Scientific Volume Imaging, Hilversum, The Netherlands).
5. If the column was not exactly aligned with the y -axis, the images were rotated to achieve a perfect alignment and simplify the subsequent analysis.

To illustrate the effect of the image restoration process, a raw and a restored image are shown in Fig. 1.1B and C. For a detailed analysis of the morphology, the position and radius of every particle in the reconstructed section have to be determined. The procedure has been previously described in detail [24,25,38]. The following steps were applied:

1. The positions of the particle centres were estimated using ImageJ. A variance filter and an unsharp mask were applied to duplicates of the original image stack. A logical AND operation on the two resulting images provided clusters whose central positions were determined [38].
2. The resulting list of preliminary particle positions was used as input for a fitting algorithm. A number of circles with increasing diameter around the coordinate were analysed until the mean intensity of a circle or the variance within the circle reached a specified threshold. This procedure was repeated with x -, y -, and z -variation around the starting position to determine the largest fitting particle. The resulting “best centre” and the corresponding radius were saved to describe the particle.
3. The fitting procedure was repeated with a variation of threshold parameters to determine the ideal fitting parameters for the specific image stack. The best result was chosen

based on several criteria: (i) best compliance of this PSD with the PSD obtained from SEM data for the particle batch (cf. Section 1.2.7), (ii) minimization of the number of particles showing unrealistic overlap with neighbouring particles, (iii) minimization of the number of isolated particles without contact to neighbouring particles, and (iv) maximization of optical quality by an overlay of the enhanced image stack with the spheres resulting from the fit.

4. Obvious errors were removed from the list of particles manually. This included the removal of particles showing strong overlap and isolated particles as well as an optical control for misfits.
5. Particles that could not be fitted correctly by the algorithm were marked manually. For the column packed with the 40 mg/mL slurry every particle was determined manually because of the limited image quality.
6. The list of particle positions and radii was used to draw an image stack of spheres assuming perfect sphericity.
7. Non-spherical fragments were drawn manually based on the original image stack and added to the sphere image stack to ensure a complete representation of the packing. The resulting binarized image stacks are referred to as “reconstructions” in the remainder of the discussion.

1.2.6 Analysis of the reconstructions

Since many properties of a reconstruction are commonly analysed in relation to the distance from the column wall, the position of the solid capillary wall had to be accurately determined. An xz -image of the mean intensity along the column axis was calculated from the reconstruction. For every z -position, the two first points below the intensity threshold (when viewing from the column centre) were determined and used as wall points. A local polynomial fit was applied to these points to create a continuous description of the column wall. The smallest Euclidean distance to the wall was calculated for every investigated particle coordinate and investigated voxel. Furthermore, the column centre and the exact distance between image slices were determined from the column wall points.

The binarized image stack, the list of particles, and the column wall fit were used to calculate the following properties. Radial profiles of external porosity, $\varepsilon(r)$, were derived from counting black voxels (interparticle void) and white voxels (particles) in cylindrical shells obtained by scaling the shell boundaries around the column centre with a step size of 150 nm. The relative radial porosity $\varepsilon_{\text{rel}}(r) = \varepsilon(r) - \varepsilon_{\text{bulk}}$ was received by subtracting the external porosity in the bulk packing $\varepsilon_{\text{bulk}}$ from the actual porosity for every distance r to the wall ($r = 0$ at the wall). The integral porosity deviation (IPD) was determined as introduced previously [24,25] (cf. Section 1.3.2.1). IPDs were calculated by integration of the relative radial porosity profiles (see later, Fig. 1.7). Two integration limits were used: (i) from $r = 0$ (wall) to $r = 10.5 \mu\text{m}$ ($\equiv 8 d_p$), where bulk behaviour is realized, and (ii) from the first zero transition of $\varepsilon_{\text{rel}}(r)$ (after approximately $1/3 d_p$) to $r = 10.5 \mu\text{m}$, as before. Radially resolved PSDs for the analysis of size segregation were calculated from the determination of the mean particle diameter in cylindrical shells with

a size of 450 nm in 150 nm steps according to the particle centre positions from the column wall towards the centre.

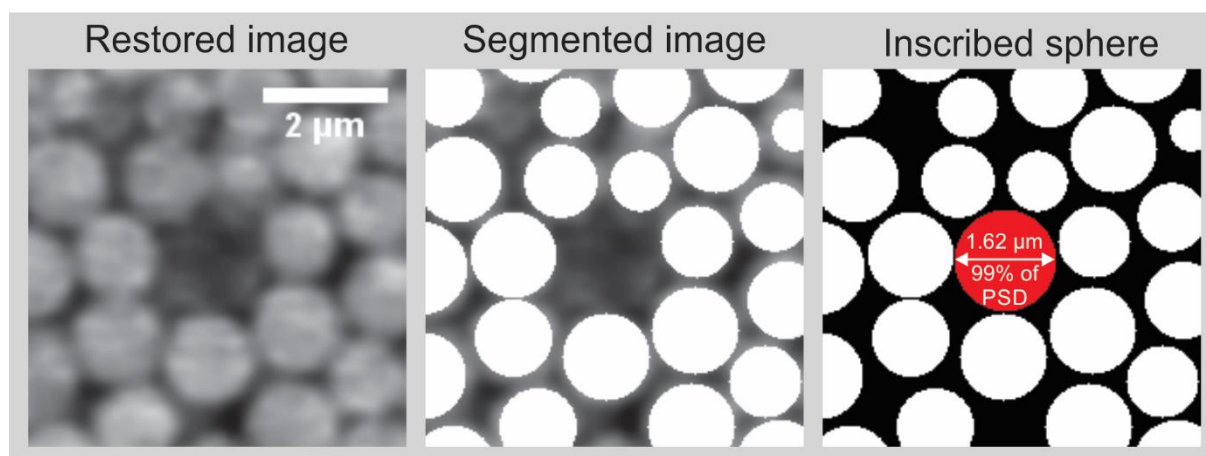


Figure 1.2. Largest void in a reconstruction ($c_{\text{slurry}} = 40 \text{ mg/mL}$). The restored image (left) is used for segmentation. An overlay of the restored image with the segmented image is shown in the center. The larger voids are detected by inscribing spheres in the void space of a reconstruction. The highlighted inscribed sphere (right) has a diameter of $1.62 \mu\text{m}$. Therefore, this void can accommodate 99% of the $1.3 \mu\text{m}$ BEH particles.

Packing voids were identified by inscribing spheres into the reconstruction's void spaces. A void is considered large when the largest inscribed sphere has a diameter of at least $1.08 \mu\text{m}$, corresponding to a threshold of 10% of the SEM-based PSD. Voids are further distinguished into voids which can accommodate spheres with a size from 10–50% of the PSD (1.08 – $1.31 \mu\text{m}$), 50–90% (1.32 – $1.43 \mu\text{m}$), or $\geq 90\%$ ($\geq 1.44 \mu\text{m}$). Figure 1.2 shows the largest void from all three reconstructions (with a diameter of $1.62 \mu\text{m}$, corresponding to 99% of the spheres from the PSD) in three ways: restored image (left), segmented image as an overlay with the restored image (middle), and with the largest inscribed sphere in the reconstructed image (right).

1.2.7 Scanning electron microscopy (SEM)

The BEH particles in the capillary column packed with a slurry concentration of 15 mg/mL were subsequently flushed out of the column with ethanol (applying a pressure of 200 bar) after cutting off the column end. They were gently washed with acetone and ethanol, dried for 12 h at $70 \text{ }^\circ\text{C}$, and carefully deposited onto a carbon film on a SEM sample holder. Loose particles were removed using a stream of compressed air to avoid contamination of the instrument. The sample was then sputtered with platinum for 90 s and transferred into the SEM chamber of a JSM-7500F scanning electron microscope (JEOL, München, Germany). Images were acquired at 5 keV using the lower secondary electron image at a working distance of 8 mm or the secondary electron image at a working distance of 7.6 mm. Image resolution for determination of the PSD was set to 1280×940 pixels with a magnification of 2700-fold. Particle diameters were determined by overlaying circles in the images using the same in-house written program as applied for the CLSM images to ensure maximal comparability.

1.2.8 Pycnometry

Pycnometry measurements [68] were used to confirm the high interparticle porosity of packings found by CLSM imaging. A column packed with $c_{\text{slurry}} = 24$ mg/mL was flushed and characterized as described in Sections 1.1.2.2 and 1.1.2.3. The capillary was then dried at 120 °C and weighed daily using a MICRO GRAM-ATIC balance (Mettler Instrument Corp., Hightown, NC) until the measured mass varied by only 0.0001 g. The column was then filled with 50/50 (v/v) water/acetonitrile until a droplet was visible at the column outlet. This process was repeated three times with fill pressures ranging from 875 to 1400 bar. The density of the mobile phase was determined using two separate volumetric flasks (25 and 10 mL) of which an average density was determined. Weight difference and average liquid density were used to calculate the total porosity of the column, as described in Section 1.3.2.1.

1.3 Results and discussion

1.3.1 Kinetic column performance

Capillaries with inner diameter of 75 μm were packed with slurry concentrations ranging from 5 to 50 mg/mL of fully porous 1.3 μm C18-modified BEH particles and characterized with hydroquinone as analyte in a 50/50 (v/v) water/acetonitrile 0.1% TFA mobile phase. Under these conditions, hydroquinone has a retention factor of $k' = 0.20$ (is weakly retained) and thus reflects kinetic column efficiency. We do not want to take measurements at the dead time due to noise related to the pressure injection. We do however want to measure fluid dynamics and a lightly retained compound is the best choice to do this. Plate height data for 4-methyl catechol (moderately retained) are indeed almost indistinguishable from the hydroquinone data.

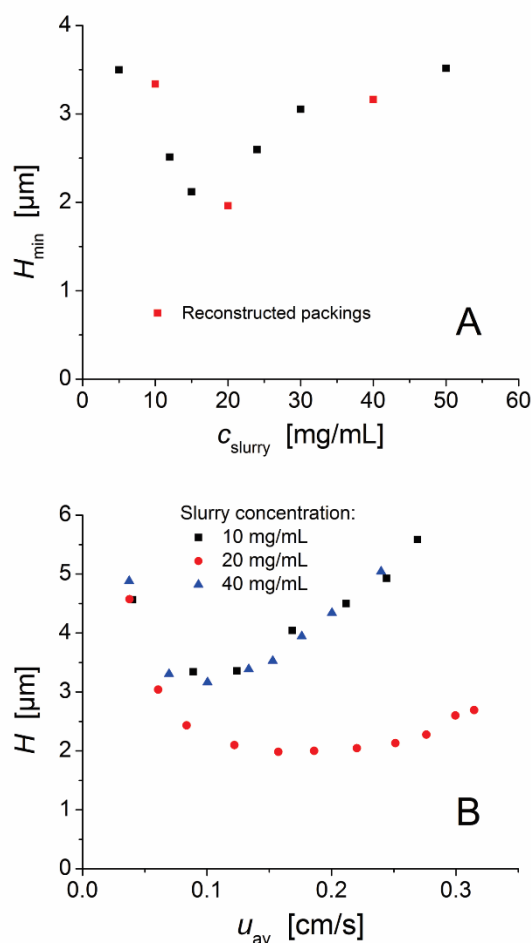


Figure 1.3. Minimum plate heights and full plate height curves. (A) Plate height minima (H_{\min} , extracted from the plate height curves) vs. the slurry concentration for the entire set of the nine capillary columns packed with 1.3 μm C18 BEH particles. (B) Plate height curves for the three columns selected for CLSM-based reconstruction and morphological analysis (plate height H for hydroquinone in a 50/50 (v/v) water/acetonitrile mobile phase, $k' = 0.20$, vs. average mobile phase flow velocity u_{av}).

The minimum plate height H_{\min} was determined from the $H-u_{\text{av}}$ plots for every column and is shown in Fig. 1.3A. Interestingly, the lowest H_{\min} is observed for an intermediate slurry concentration (~ 20 mg/mL), whereas lower and higher slurry concentrations both result in lower efficiencies. Three columns from this set were chosen for studying morphological origins behind the different performances of these packings: (i) the 10 mg/mL column representing low slurry concentration, (ii) the 20 mg/mL column representing ideal intermediate concentration for the actual set of packing conditions in this work (including the 1.3 μm C18 BEH particles, a bed length of ~ 34 cm, 75 μm column i.d., and acetone as slurry solvent), and (iii) the 40 mg/mL column representing high slurry concentration.

Full $H-u_{\text{av}}$ plots for the three selected columns are shown in Fig. 1.3B. The reduced plate heights $h = H/d_p$ are determined for comparison with other columns by using the mean particle diameter d_p . The 20 mg/mL column has a minimum plate height of 1.98 μm , resulting in a reduced minimum plate height of $h_{\min} = H_{\min}/d_p = 1.5$ and a plate count of $N \sim 170,000$ for a

bed length of 34 cm ($\sim 500,000$ N/m), characteristic of a very good column. The two other columns show a higher minimum plate height of ~ 3.2 μm (Fig. 1.3A), resulting in a reduced minimum plate height of ~ 2.4 , still good compared to other recent capillary HPLC studies [22,23,69–75]. Furthermore, the slope of the plate height curve for the 20 mg/mL column is decidedly smaller than for the two other columns (Fig. 1.3B). Following the classical model, it is connected to different mass transfer resistances described by the c -term in the reduced van Deemter equation [10]:

$$h = a + \frac{b}{v} + cv \quad (1.1)$$

The velocity-independent a -term represents eddy dispersion, the b -term the longitudinal diffusion driven by the concentration gradients along the column, and $v = u_{av}d_p/D_m$ is the reduced velocity, where D_m represents the pressure-dependent diffusion coefficient of the analyte in the bulk mobile phase [76]. With Eq. (1.1), the mass transfer resistance term (cv) cannot explain the different slopes of the plate height curves in Fig. 1.3B, since identical particles from the same batch were used for column preparation. Furthermore, eddy dispersion is a more complex phenomenon, which requires actual representation by a velocity-dependent term. A better physico-chemical characterization of the hydrodynamics is achieved by coupling transverse diffusion and spatial velocity fluctuations, as originally proposed by Giddings [10,77]:

$$h = \frac{b}{v} + \sum_{i=1}^3 \frac{2\lambda_i}{1 + \left(\frac{2\lambda_i}{\omega_i}\right)v^{-1}} + cv \quad (1.2)$$

The first term (b/v) and the last one (cv) account, respectively, for longitudinal diffusion along the column and the mass transfer kinetics into and across the fully porous BEH particles used in the current work. Remaining terms in Eq. (1.2) characterize eddy dispersion on different time and length scales and represent the transchannel contribution ($i = 1$), which reflects the velocity profile on the individual pore level between the packing particles; the short-range interchannel contribution ($i = 2$), which refers to the velocity bias on a length scale of ~ 2 particle diameters typical for disordered packings (absent in ordered packings); and the transcolum contribution ($i = 3$) characterizing the velocity heterogeneity over the cross-section of the capillary columns due to wall effects. ω_i and λ_i are structural parameters characteristic of each eddy dispersion contribution.

Capillaries analysed in this work have bed lengths (34 cm) such that the ratio of bed length and column inner diameter is ~ 4500 . Thus, under all mobile phase flow velocities and associated transverse dispersion coefficients [78], full lateral equilibration of hydroquinone molecules is achieved between all velocity extremes over the column cross-section. This is true even for the largest time and length scales related to the transcolum equilibration of wall effects [79]. Under these conditions, the comprehensive Giddings equation, Eq. (1.2), can be expressed in

the following form, as demonstrated by detailed simulation studies of plate height data for bulk (unconfined) and complementary confined packings [14,15,80]:

$$h = \frac{b}{v} + \omega_1 v + \frac{2\lambda_2}{1 + \left(\frac{2\lambda_2}{\omega_2}\right)v^{-1}} + \omega_3 v + cv \quad (1.3)$$

The justified simplifications in Eq. (1.3) with respect to Eq. (1.2) cover transchannel and transcolumn eddy dispersion contributions ($i = 1$ and 3 , respectively), which are now, in Eq. (1.3), represented by simple velocity-dependent terms, indistinguishable from the intraparticle mass transfer resistance term (cv). Importantly, differences in (laterally equilibrated) wall effects of the analyzed columns manifest themselves in different linear slopes, i.e., different ω_3 -terms of the plate height curves at velocities above the plate height minimum (cf. Fig. 1.3B). The transcolumn dispersion contribution can be viewed as a simple mass-transfer resistance term governed by a weakly velocity-dependent [78] transverse dispersion coefficient. This clarified situation will be helpful when the results of the morphological analysis, e.g., wall effects, are correlated to separation efficiency. The relative influence of morphological features identified for this set of capillary columns on the plate height data is discussed in detail in the subsequent sections.

1.3.2 Physical reconstructions and bed morphology

Selected properties of the three reconstructions ($c_{\text{slurry}} = 10, 20, \text{ and } 40 \text{ mg/mL}$) are summarized in Table 1.1. The CLSM-based PSDs are compared with the SEM-based PSD in Fig. 1.4. As a result, all columns show a very similar mean and median particle diameter and a relative standard deviation of the PSDs of $\sim 15\%$. This confirms the quality of the reconstructions and the comparability of the results. The principal repeatability of reconstructions was shown in previous studies on monolithic columns [43,52]. Consequently, we analysed one reconstruction for every column, since imaging and reconstruction are time-consuming, especially for these small particle diameters.

Table 1.1. Properties of the reconstructions and PSDs.

	10 mg/mL	20 mg/mL	40 mg/mL	SEM based
No. of particles	6813	20327	7280	1659
Mean d_p [μm]	1.30	1.30	1.31	1.31
Median [μm]	1.32	1.32	1.32	1.32
$\varepsilon_{\text{bulk}}$ [–]	0.47	0.48	0.50	–

While repeated chromatographic measurements would likely yield slightly different plate height values, we do not believe repetition with additional columns would change the ultimate morphological structures underlying a decrease in performance as one moves away from a 20 mg/mL slurry concentration. Below, we show dominating morphological structures that contribute to decrease in efficiency as the concentration is adjusted. For the work presented,

distinctly different features are attributed to the columns packed with 10 and 40 mg/mL slurry concentrations even though they share likeness in performance (Fig. 1.3B). Through CLSM each column exhibits structural differences that independently explain the decreased performance when compared to the 20 mg/mL column. Our conclusions elucidate morphologies dominant when one packs with a slurry concentration greater or less than the optimal.

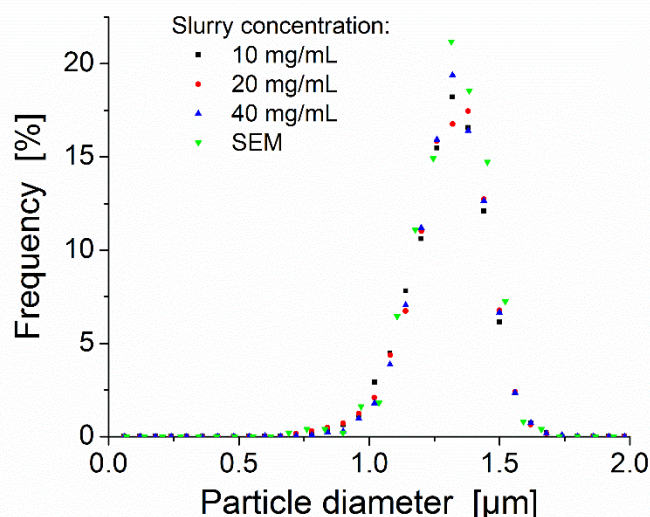


Figure 1.4. Particle size distribution (PSD) analysis for the 1.3 μm BEH particles: CLSM-based PSDs for the reconstructed capillary column beds in comparison with the SEM-based PSD.

Packing and use of 1.3 μm particles in our lab has yielded repeatable performance when similar slurry concentrations are used. In fact, we have found slurry concentration to be the one of the most dominant variables associated with ultimate column performance. We would also point to Fig. 1.3A as further justification of repeatability. Here, a well-defined trend is seen as a function of slurry concentration for a series of columns packed identically except for slurry concentration. Performance markedly improves for all columns packed with slurries close to 20 mg/mL. General agreement in trend of nine packed capillaries is indicative of reproducibility.

1.3.2.1 Packing density, porosity distribution, radial heterogeneity

The simplest way to visualize radial heterogeneities are radial porosity profiles, which display the local porosity $\varepsilon(r)$ in the form of the interstitial void volume fraction as a function of radial position ($r = 0$ at the wall), as shown in Fig. 1.5. The first, highly ordered layer of particles in direct contact with the column wall, characterized by the minimum in $\varepsilon(r)$ at $r \approx 0.5 d_p$ (centre of particles from the first particle layer), is clearly visible for all columns. With increasing distance from the column wall (up to $\sim 5 d_p$), the oscillations relax into random, bulk behaviour. Interestingly, all columns show a high bulk porosity ($\varepsilon_{\text{bulk}} = 0.47\text{--}0.50$, Table 1.1). These values are indeed far away from the random-close packing limit at $\varepsilon_{\text{bulk}} \approx 0.35$, as estimated from

computer simulations for frictionless hard spheres with a similar PSD [81]; these bulk packings are even less dense than the random-loose packing limit for frictional hard spheres suggests [82–87]. From this point of view, the high porosities in Table 1.1 are surprising, since bed collapse and a secondary consolidation may be expected under the extreme conditions in UHPLC unless a significant number of larger voids, created during column packing, remained stable after bed consolidation. However, no sign for bed collapse has been observed. For example, with regards to mechanical bed stability, the 24 mg/mL column was used for pycnometry experiments (see analysis below) approximately two years after initial packing following the unexpected packing density results. Prior to testing the column was visually studied with a microscope for the presence of column damage. Columns packed identically are often used in our lab for LC–MS applications and experience a variety of mobile phases and pressures exceeding 3000 bar. The settling of individual particles, particle assemblies, or even whole parts of the bed would be immediately recognized in (drastically) decreased separation efficiencies.

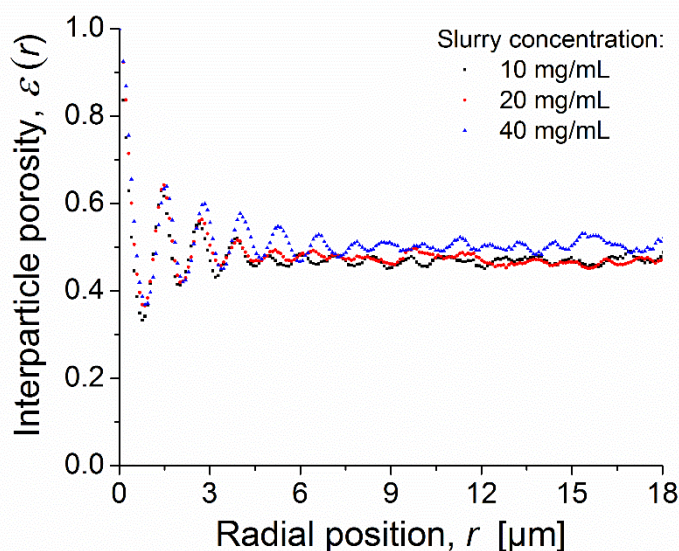


Figure 1.5. Radial porosity profiles ($r=0$ at the column wall). Distribution of the interstitial void volume fraction $\varepsilon(r)$ in the reconstructed sections from the three columns packed with different slurry concentrations.

The reasonability of the obtained bulk porosity values ($\varepsilon_{\text{bulk}} = 0.47\text{--}0.50$) was verified in different ways. First, we note that the PSDs of all three columns correspond well with the PSD obtained by SEM (Fig. 1.4, cf. Table 1.1), which benefits from a much better resolution than CLSM. Second, the absolute number of particles in a reconstruction remains unaffected by small fitting errors. Thus, the numbers of particles determined within each CLSM-based reconstruction together with the SEM-based PSD were used to calculate the volume occupied by this number of particles. The obtained volume was divided by the overall volume of the reconstruction and resulted in practically indistinguishable porosity estimates. Third, the column packed with $c_{\text{slurry}} = 24$ mg/mL was used for a pycnometry experiment, which provided

an average mass difference of $\Delta m = 1.070$ mg between dry and liquid-filled column. The external bed porosity ε_{ext} is determined using the density of the liquid ($\rho_{\text{liquid}} = 0.9070$ g/mL), the specific pore volume of the BEH particles ($V_{\text{pore}} = 0.70$ cm³/g) provided by the manufacturer, the length of the column ($l_{\text{column}} = 33.6$ cm), the internal radius of the column ($r_{\text{column}} = 37.5$ μm), a density of $\rho_{\text{silica}} = 2.00$ g/cm³ for BEH material [88], the volume of the liquid phase V_{liquid} , the total inner column volume V_{column} , the total porosity of the packing $\varepsilon_{\text{total}}$, and the internal porosity $\varepsilon_{\text{intra}}$ of the BEH particles.

$$V_{\text{liquid}} = \frac{\Delta m}{\rho_{\text{liquid}}} \quad (1.4)$$

$$V_{\text{column}} = \pi r_{\text{column}}^2 l_{\text{column}} \quad (1.5)$$

$$\varepsilon_{\text{total}} = \frac{V_{\text{liquid}}}{V_{\text{column}}} \quad (1.6)$$

$$\varepsilon_{\text{intra}} = \frac{V_{\text{pore}}}{V_{\text{pore}} + \rho_{\text{silica}}^{-1}} \quad (1.7)$$

$$\varepsilon_{\text{ext}} = \frac{\varepsilon_{\text{total}} - \varepsilon_{\text{intra}}}{1 - \varepsilon_{\text{intra}}} \quad (1.8)$$

The calculated internal porosity of the particles ($\varepsilon_{\text{intra}} = 0.60$) agrees very well with values reported previously for BEH particles [88]. The calculated external porosity of the packing ($\varepsilon_{\text{ext}} = 0.49$) lies between the values for columns packed with $c_{\text{slurry}} = 20$ mg/mL ($\varepsilon_{\text{ext}} = 0.48$) and $c_{\text{slurry}} = 40$ mg/mL ($\varepsilon_{\text{ext}} = 0.50$), as one may expect (see Table 1.2 for details).

Table 1.2. Determination of the external bed porosity from pycnometry experiments.

Δm^a [mg]	ρ_{liquid} [g/mL]	V_{liquid} [nL]	V_{total} [nL]	$\varepsilon_{\text{total}}$ (Eq. (1.6))	$\varepsilon_{\text{intra}}^b$ (Eq. (1.7))	ε_{ext} (Eq. (1.8))
1.070	0.907	1180	1484	0.795	0.60	0.488

^a Average value from three measurements.

^b Calculated with a specific pore volume of $V_{\text{pore}} = 0.70$ cm³/g provided by Waters Corporation (Milford, MA).

After this independent confirmation of the high bed porosities the question arises how these beds remain mechanically stable. It may be explained by the presence of “larger voids” (here, this term refers to voids ≥ 1.08 μm , which corresponds to sphere sizes of $\geq 10\%$ of the PSD), as discussed in detail in Section 1.3.2.2. However, for the column packed with $c_{\text{slurry}} = 40$ mg/mL the actual volume of voids classified as such larger voids only accounts for approximately 0.6% of the reconstruction. This does not exclude the possible existence of a substantial number of voids below this threshold, which are still larger than those found between particles near the

random-close packing limit. The additional question therefore arises: Which are the forces that keep the particles stuck together in such loose column beds, allowing little rearrangement during bed consolidation? Cohesion between particles is the important phenomenon here and becomes more important as the particle size decreases, particularly towards submicrometre dimension.

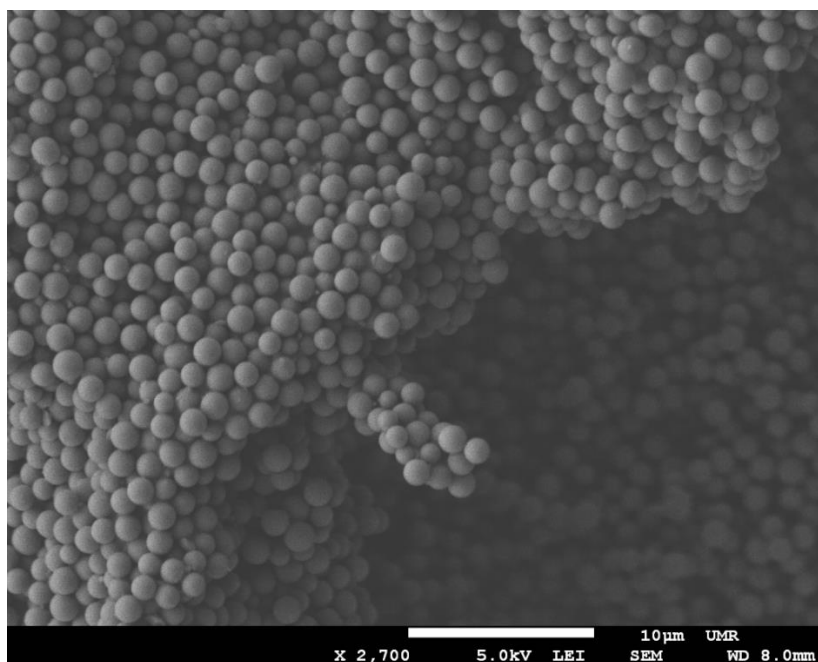


Figure 1.6. SEM picture with exposed parts of a capillary packing, obtained after the prepared and chromatographically characterized bed (15 mg/mL slurry; $H_{\min} = 2.1 \mu\text{m}$) has been extruded from the capillary, dried, mounted onto a sample holder, and exposed to a strong stream of nitrogen gas. The rigid, stable bed structure built by the $1.3 \mu\text{m}$ BEH particles, particularly the firmly anchored packing branch, is indicative of the particles cohesion.

In this work small, frictional, cohesive ($1.3 \mu\text{m}$ C18-modified BEH) particles are used in column packing studies. Because of their surface roughness, the frictional particles show resistance as they try to move against each other. This will result in lower packing densities (higher bed porosities) than with perfectly smooth, frictionless particles. During column packing and bed consolidation the particles experience not only frictional but also cohesive forces. In this regard, van der Waals forces between the nonpolar BEH particles dominate and support the formation of aggregates, especially in more concentrated slurries. These attractive forces are known to increase, eventually significantly, the interparticle void volume fraction of loose but stable packings of such small particles [89–92]. This can explain why the investigated packings show external porosities even above random-loose packing of frictional but cohesionless particles. An important feature of slurrying and packing such fine cohesive particles therefore is the formation of aggregates or agglomerates. This aspect has been studied by Blue and Jorgenson [9] for different slurry solvents using in-solution optical microscopy. Based on their results we expect aggregation to occur to some extent in the acetone slurries

used in the present work. Figure 1.6 indicates the relevance of cohesion between particles during column packing. This SEM picture shows parts of a packing after it has been extruded from the capillary, dried, mounted onto a sample holder, and exposed to a strong stream of nitrogen gas. The retained (particularly anchored), rigid bed structure, even after bed extrusion, together with the so unexpectedly high interparticle porosity and the fact that we have relevant chromatographic data is a testament to the particles cohesion.

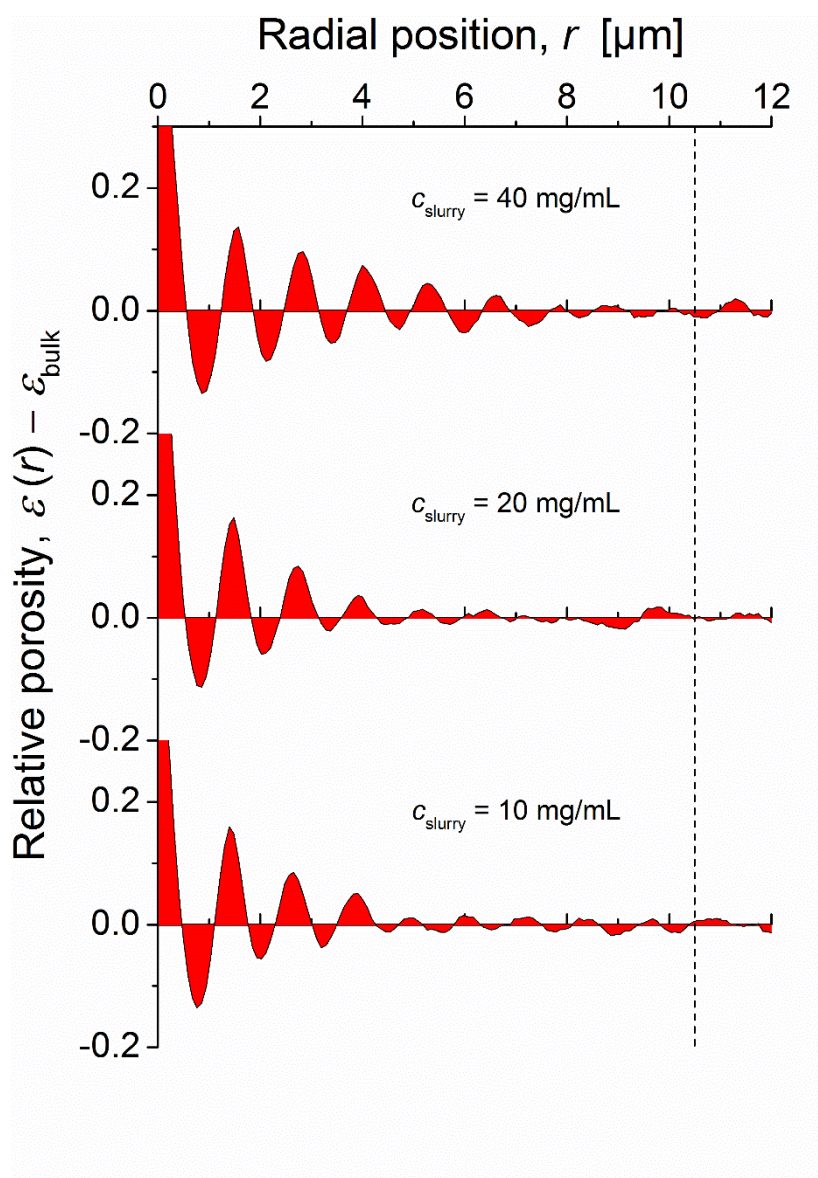


Figure 1.7. Radial distribution of relative porosity, $\varepsilon(r) - \varepsilon_{\text{bulk}}$, used to calculate integral porosity deviations (IPDs) for the three columns packed with different slurry concentrations ($r = 0$ at the column inner wall); the values of $\varepsilon_{\text{bulk}}$ are given in Table 1.1. The dashed line indicates the radial position of $r = 10.5 \mu\text{m}$ ($\equiv 8 d_p$) used in the calculation of the IPDs (see text for details).

To summarize, the slurry packing process in the current work results in unusually high but stable bed porosities. These values are offset by frictional and cohesive forces between the small

particles ($d_p = 1.3 \mu\text{m}$), which impede bed densification requiring particle sliding. The high bulk porosities observed here for the $1.3 \mu\text{m}$ particles ($\varepsilon_{\text{bulk}} = 0.47\text{--}0.50$) continue the trend from our previous work [56] with larger BEH particles packed under similar conditions ($\varepsilon_{\text{bulk}} = 0.44$ for $d_p = 1.7 \mu\text{m}$ and $\varepsilon_{\text{bulk}} = 0.39$ for $d_p = 1.9 \mu\text{m}$). This is an expected trend [89,90], although final bed porosities for given particle properties depend on the actual packing conditions.

The different bulk porosities ($\varepsilon_{\text{bulk}}$, Table 1.1) have implications for eddy dispersion taking place on transchannel and short-range interchannel scales. For microscopically disordered, macroscopically homogeneous (bulk) packings, Daneyko et al. [93] have shown that higher bed porosities result in higher minimum plate heights. Based on that study, an increase of $\sim 10\%$ in the minimum plate height can be estimated due to the change in bulk porosity from 0.47 to 0.50. As a consequence, the increased porosities with higher slurry concentrations may be a factor resulting in less efficient columns but cannot explain the difference of 60% in the reduced minimum plate heights between columns packed with $c_{\text{slurry}} = 20$ and 40 mg/mL ; porosity differences between bulk packing region and wall region are more important.

Table 1.3.

Values of the integral porosity deviation (IPD, cf. Eq. (1.9)).

	10 mg/mL	20 mg/mL	40 mg/mL
IPD ^a	0.148	0.193 ^c	0.156
IPD ^b	0.027	0.042 ^c	0.0017

^a Calculated with integration limits from $r = 0$ to $r = 10.5 \mu\text{m}$ ($\equiv 8 d_p$), cf. Fig. 1.7.

^b Calculated with integration limits from the first zero transition of $\varepsilon_{\text{rel}}(r)$ after $\sim 1/3 d_p$ (instead of $r = 0$) up to $r = 10.5 \mu\text{m}$.

^c Biased by an optical artifact in the image stack.

To get a closer look at the porosity differences between bulk and wall region in the packings, radial relative porosity profiles $\varepsilon_{\text{rel}}(r)$ were calculated as $\varepsilon_{\text{rel}}(r) = \varepsilon(r) - \varepsilon_{\text{bulk}}$. Figure 1.7 focuses on the wall region, since this is the most critical region for heterogeneities induced by the wall with respect to the bulk packing in terms of its structural organization (particle arrangement), mean porosity, and the local porosity distribution [14,24,25,56]. It is observed with all three columns that the porosity statistically fluctuates around its bulk value until the wall region is entered ($r = 0$ at the wall). Near the wall, the porosity profiles show damped oscillations around some mean value that may deviate more or less from the mean value in the bulk [25]. We have previously used the integral porosity deviation (IPD) as scalar measure to quantify heterogeneities in radial porosity profiles [24,25], where local porosity deviations with respect to $\varepsilon_{\text{bulk}}$ are integrated over the column radius r_c (i.e., from $r = 0$ at the wall up to $r = r_c$):

$$\text{IPD} = \int_0^{r_c} (\varepsilon(r) - \varepsilon_{\text{bulk}}) dr \quad (1.9)$$

For the investigated capillary columns the IPD should be positive, since we expect the beds to be packed more loosely in the wall than in the bulk region, as observed before for BEH [25]

and other fully porous particles [24]. IPDs calculated from the profiles in Fig. 1.7 are summarized in Table 1.3. Since not all columns could be reconstructed up to the column centre ($r = r_c$), IPDs are calculated from the column wall ($r = 0$) to $r = 10.5 \mu\text{m}$ (corresponding to a distance of $8 d_p$), after which bulk behaviour is achieved; the contribution of the bulk region to the IPD is zero by definition. IPDs for all three columns vary between 0.15 and 0.2 (first row in Table 1.3) and are comparable to the set of well performing columns from our previous study [25], where poorly performing columns, by contrast, showed an IPD between 0.39 and 0.49. Surprisingly, the 20 mg/mL column with the highest separation efficiency (Fig. 1.3) also shows the highest IPD. To resolve this obvious contradiction, we took a deeper look at the original images, the reconstruction, and the porosity profiles, which revealed that a stage error had occurred during acquisition of this CLSM image stack, altering the z -step size of the affected sections. This results in slight offsets in the affected parts of the radial porosity profile. At the same time, the calculation of the IPD relies on accurate values of the bulk porosity. To avoid misinterpretations, the following discussion focusses on the two other columns. Our analysis of larger voids in Section 1.3.2.2 remains unaffected by this circumstance, since every determined void is individually checked for overlap with non-spherical fragments or overlap with particles. An analysis of the relative porosity $\varepsilon_{\text{rel}}(r)$ in Fig. 1.7 with increasing distance from the wall reveals that the void space between the wall and first particle layer is the main contributor to all IPDs. This may result in relatively high local flow velocities adjacent to the wall depending on packing density and homogeneity, whereas the flow velocity directly at the wall is zero due to the no-slip boundary condition [14]. For retrieving small, but important (if not decisive) differences between these three porosity profiles, a second set of IPDs was calculated (second row in Table 1.3), with the integration limits now set from the first zero transition of $\varepsilon_{\text{rel}}(r)$, which occurs after a distance of about $1/3 d_p$ from the wall, up to $r = 10.5 \mu\text{m}$ ($\equiv 8 d_p$), as before. In this IPD representation, the column packed with $c_{\text{slurry}} = 10 \text{ mg/mL}$ shows an increase in its IPD by an order of magnitude over the column packed with $c_{\text{slurry}} = 40 \text{ mg/mL}$. This highlights a more loosely packed wall region for low than for high slurry concentrations compared to the bulk region of the beds. As a consequence, higher flow velocities occur in the transition region between the stagnant fluid layer directly at the column wall (with local liquid stick) and the bulk packing region, contributing to transcolumn eddy dispersion seen in simulations [13–15] and experiments [24,25]. Since a laterally equilibrated transcolumn contribution is properly represented with the simple velocity-proportional ω_3 -term in Eq. (1.3), the suppression of this effect with higher slurry concentrations is expected to result in a decreased slope of the plate height curves beyond the plate height minimum. While this correlates well with the decreased slope of the 20 mg/mL column over the 10 mg/mL column (Fig. 1.3B), the 40 mg/mL column shows an increased plate height and slope compared to the 20 mg/mL column. Therefore, morphological features in the column wall region and the associated transcolumn eddy dispersion contribution alone cannot explain all differences in separation efficiency we observed for columns packed with different slurry concentrations. Additional morphological features must be identified, which are responsible for the subsequent efficiency decrease at high slurry concentration after the optimal intermediate concentration of 20 mg/mL has been passed

(Fig. 1.3). This search guided us directly (visually) to the analysis of larger voids, whose presence seems to be favoured in packings prepared from high slurry concentration.

1.3.2.2 Analysis of larger voids

Table 1.4. Number of larger voids in the reconstructed column bed sections. ^a

	Size	10 mg/mL	20 mg/mL	40 mg/mL
Voids per reconstruction	$\geq 1.08 \mu\text{m}$	48	256	126
	$\geq 1.32 \mu\text{m}$	1	6	8
	$\geq 1.44 \mu\text{m}$	–	–	3
Voids per 1000 particles	$\geq 1.08 \mu\text{m}$	7.05	12.59	17.31
	$\geq 1.32 \mu\text{m}$	0.15	0.30	1.10
	$\geq 1.44 \mu\text{m}$	–	–	0.41

^a A void is considered as a larger void when the largest inscribed sphere has a diameter of at least $1.08 \mu\text{m}$, which corresponds to a threshold of 10% of the SEM-based PSD.

In our last study, we already compared columns prepared from two different slurry concentrations, while other parameters in the packing protocol remained identical [56]. For all particle types used in that study, i.e., fully porous 1.7 and $1.9 \mu\text{m}$ BEH particles as well as $1.9 \mu\text{m}$ Kinetex core-shell particles, the higher slurry concentration resulted in the more efficient column, but already led to an increased number of larger voids in the final bed structure. We proposed that a gradual increase in the slurry concentration reaches a critical point, after which larger voids severely affect column efficiency and performance should start to decrease. Therefore, we carried out a detailed analysis of the void space for the set of columns in the present study. We refer to a larger void as a spherical void (obtained by inscribing spheres) that can accommodate particles with a minimum diameter of $1.08 \mu\text{m}$, corresponding to a threshold of 10% of the SEM-based PSD. The statistical analysis of the voids is illustrated with Fig. 1.8 and Table 1.4. They are further distinguished into voids which can accommodate spheres with a size from 10–50% of the PSD (1.08 – $1.31 \mu\text{m}$), 50–90% (1.32 – $1.43 \mu\text{m}$), or $\geq 90\%$ ($\geq 1.44 \mu\text{m}$). The vertical lines in Fig. 1.8 indicate these size thresholds. We obtain a clear and continuous increase in the number of voids for higher slurry concentration. Further, very large voids ($\geq 1.44 \mu\text{m}$) only appear in the column prepared with the high slurry concentration of 40 mg/mL . It indicates that the formation of these voids starts at slurry concentrations that already lead to a decrease in column efficiency (cf. Fig. 1.3A), suggesting that the voids are a decisive factor regarding the increase of H_{min} .

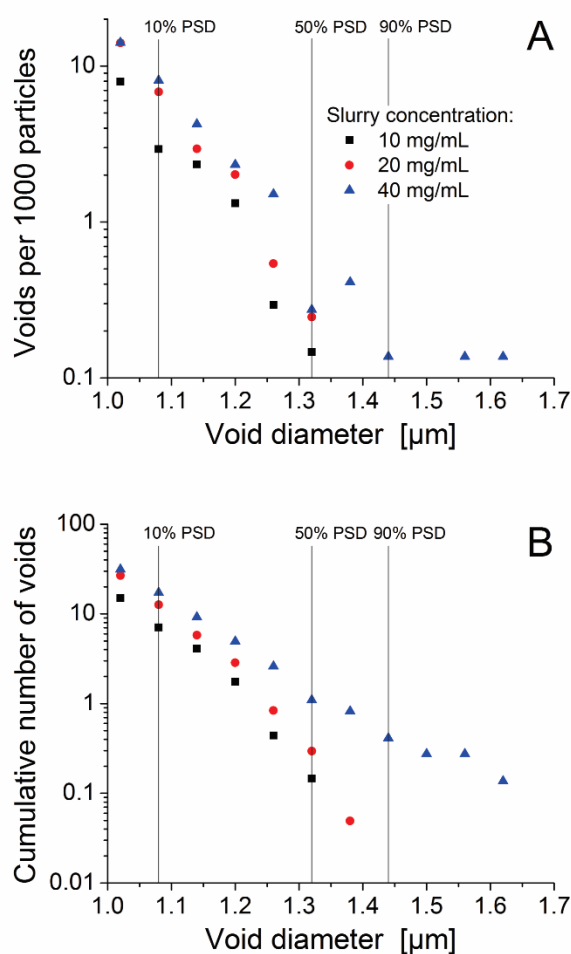


Figure 8. Number of voids for the three reconstructed column bed sections per 1000 packing particles. (A) Absolute and (B) cumulative number of voids depending on their diameter.

3D models of the reconstructions for the 10 mg/mL and 40 mg/mL column beds are shown with optically opaque particles (top panel) and transparent particles (bottom panel) in Fig. 1.9 to visualize important differences. Both the increased number of voids and the formation of larger voids are clearly visible for the high slurry concentration. Several examples of the larger voids in the column packed with $c_{\text{slurry}} = 40$ mg/mL are shown in Fig. 1.10. Interestingly, the voids are surrounded spherically by particles which stabilize each other's positions and prevent access to that void for other particles. This phenomenon is well known from research on granular packings. Several studies analysed the influence of bridges and arches within particle groups [94–100]. They can stabilize additional void space in a packing up to the formation of large voids. This is interesting considering the differences in bulk porosities discussed in Section 1.3.2.1. The formation of more void space with high slurry concentrations can be correlated to the increase in bulk porosity from $\varepsilon_{\text{bulk}} = 0.47$ for the 10 mg/mL column to 0.48 for the 20 mg/mL column (with a slight increase in the number of larger voids) to 0.50 for the 40 mg/mL, accompanied by a strong increase in the number of larger voids (especially with a diameter at

the upper end of the PSD). If voids with a diameter of $0.9\ \mu\text{m}$ and larger are taken into account, they can explain $\sim 50\%$ of the increase in the bulk porosity.

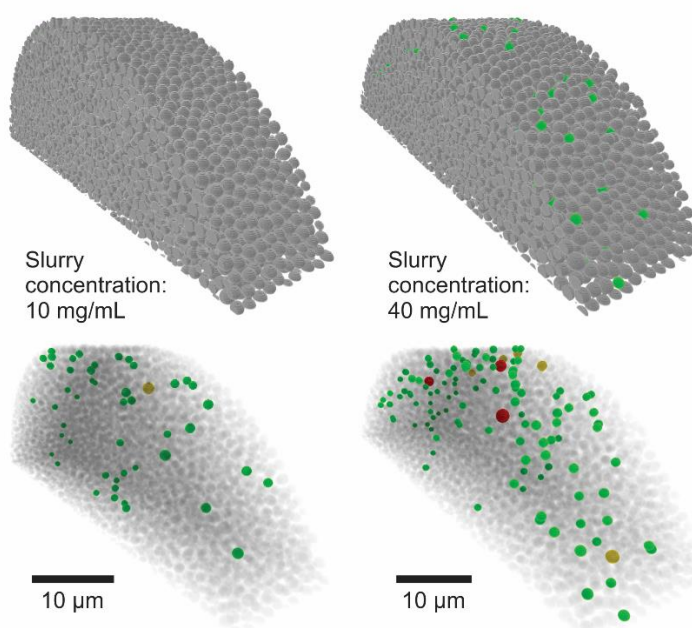


Figure 9. 3D visualization of larger voids in the CLSM-based reconstructions. Shown are 3D renderings of reconstructions for the 10 mg/mL and 40 mg/mL columns, including larger voids in the bed structures; green: voids which can accommodate spheres with a size from 10–50% of the SEM-based PSD ($1.08\text{--}1.31\ \mu\text{m}$), yellow: 50–90% ($1.32\text{--}1.43\ \mu\text{m}$), red: $\geq 90\%$ ($\geq 1.44\ \mu\text{m}$). The top panel shows the structures with optically opaque particles. In the bottom panel, particles appear transparent to highlight the larger voids inside the packings.

A similar effect has been observed when the flow velocity during column packing was varied, but slurry concentration remained constant [18,21]. Two aspects are of special interest. An optimal intermediate packing velocity was found in terms of column efficiency, similar to the optimal slurry concentration in this study [21]. Further, numerical simulations suggested that a slow packing procedure will lead to a denser packed bed [18]. Based on these observations, the time for the rearrangement process of the individual particle seems to be an important factor. It is influenced by both parameters as higher slurry concentration and higher packing velocity reduce the time before an individual particle settles in a fixed position. This leads to the question why and how these larger voids are formed. In addition to the settling process interparticle forces and particle aggregation play an important role. Formation of aggregates depends on the size of the particles, their surface properties, and slurry conditions. Larger voids that form within aggregates already in the slurry may be conserved during bed formation. Furthermore, void space conserved between different settled aggregates is not accessible for other particles. In the literature, it is recommended to avoid particle aggregation to pack efficient columns [20,21,61,101]; especially the risk of capillary clogging is pointed out [22]. On the other hand, Blue and Jorgenson [9] found methanol as an aggregating solvent to result in the most efficient

capillary for 1.1 μm core-shell particles; aggregates observed with in-solution optical microscopy were still below the size of a capillary diameter. It indicates that a certain amount of aggregation can be helpful to suppress systematic radial column heterogeneities, while large aggregates on the size of the column diameter do not pack properly. The study by Angus et al. [19] states that a good slurry solvent should result “in a well dispersed suspension of non-aggregated particles”, but they also mentioned that it is unclear if flocculation of the particles is helpful or not.

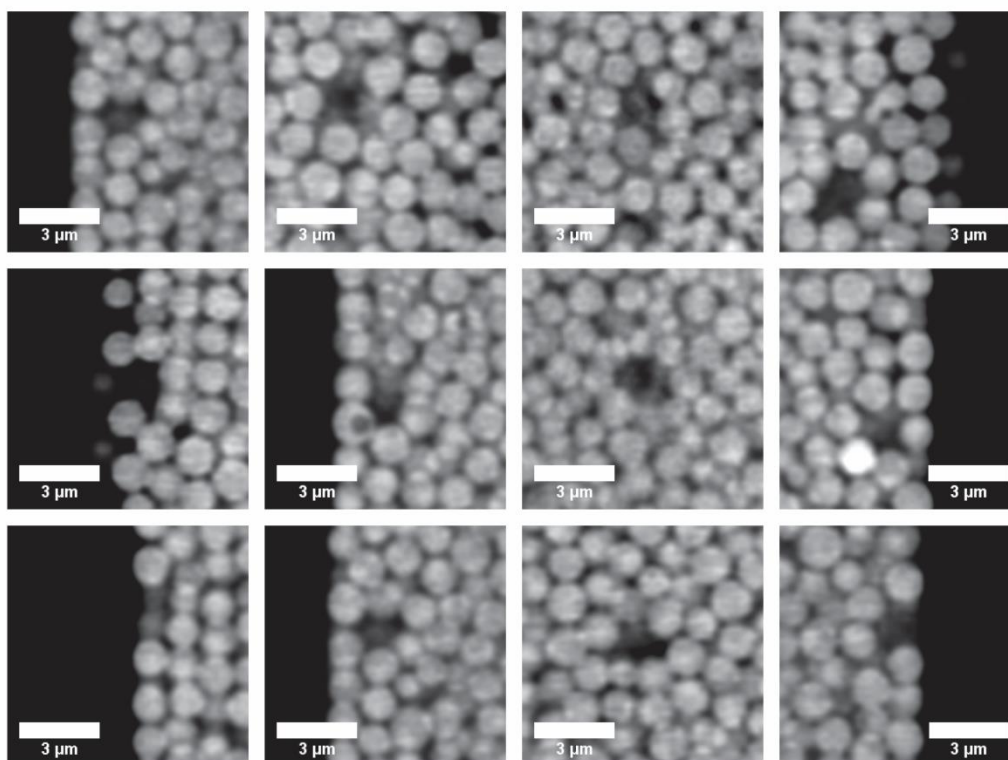


Figure 10. Examples of larger voids (which can accommodate spheres with a size $\geq 1.08 \mu\text{m}$ or $\geq 10\%$ of the SEM-based PSD) identified during bed reconstruction in the column packed with a slurry concentration of 40 mg/mL.

The mere existence of voids can be connected to eddy dispersion contributions already proposed by Giddings [77]. First, the larger voids create wider interstitial flow channels, which results in locally increased velocities. The increased velocity extremes immediately influence eddy dispersion on the two smallest length scales, i.e., transchannel and short-range interchannel eddy dispersion, altering the ω_1 -term and the ω_2 -term in Eq. (1.3). In addition, the distribution of the voids is not uniform. The reconstructions reveal sections which contain a number of larger voids and then sections without such voids. This should result in a long-range interchannel contribution to eddy dispersion, which is similar to the short-range interchannel contribution, but operates on an extended ($\sim 10 d_p$) length scale [77]. A further aspect is the radial distribution of these larger voids. In order to visualize their distribution for a qualitative analysis, a 2D projection of the voids along the y -direction is shown in Fig. 1.11. There is a

clear excess of larger voids in the wall region for both shown columns. This results in additional transcolumn heterogeneity and further increases the ω_3 -term in Eq. (1.3). The simulation work by Schure and Maier [57] already addressed the effect of packing voids on column efficiency. They determined both, the loss of column efficiency due to larger voids, in general, and an increased loss if the larger voids are not randomly distributed. However, the bed mechanics and morphological features of the void distribution were different in [57] compared with the experimental packings in the present work. Schure and Maier *a posteriori* removed a relatively small number of particle clusters from computer-generated bulk packings, which necessarily results in mechanically unstable packings, while we observed a larger number of voids in loose, but mechanically stable packings with a size on the order of d_p . Until now, we observed extremely large voids (which can accommodate 10 or more particles) only for capillary columns packed with $0.9\ \mu\text{m}$ BEH particles (see Fig. 1D in [56]). Schure and Maier [57] concluded that it is far more important to prevent defect sites leading to inhomogeneous packing rather than obtaining the highest packing density, which is not surprising given the current results. Simulations of flow and mass transport with consideration of the observed void distributions, realized by using the physical reconstructions directly as model in the simulations, will provide quantitative insight towards the impact of these voids on separation efficiency.

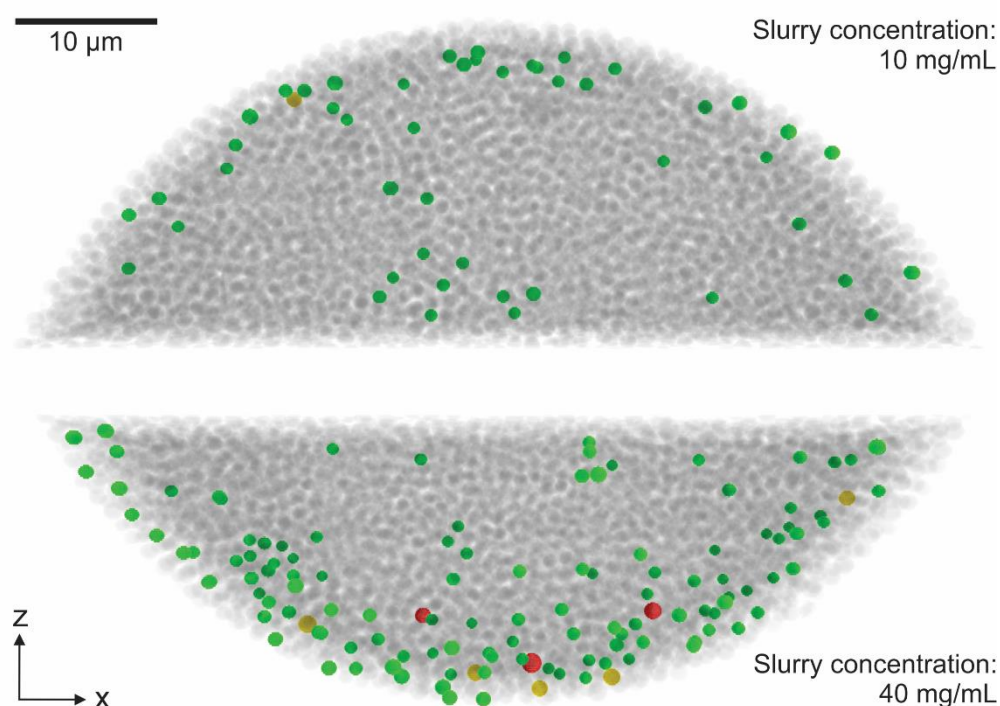


Figure 11. xz -views on the reconstructions of the 10 mg/mL and 40 mg/mL columns, including larger voids in the bed structures; green: voids which can accommodate spheres with a size from 10–50% of the SEM-based PSD ($1.08\text{--}1.31\ \mu\text{m}$), yellow: 50–90% ($1.32\text{--}1.43\ \mu\text{m}$), red: $\geq 90\%$ ($\geq 1.44\ \mu\text{m}$).

An interesting question is how the general increase in void space and the formation of void space can either be prevented, or additional void space be stabilized and distributed homogeneously. In addition to the discussed settling time and particle aggregation in the slurry,

the kinetic impact energy is a well-known factor [18]. If the incoming particles have enough energy, they can induce a rearrangement of already settled particles resulting in higher bed densities. Furthermore, different consolidation techniques have been tested during bed formation or as a subsequent step. In the granular matter community, both tapping and 3D vibrations have been applied to achieve bed densification [102–105]; granular compaction through the collapse of bridges is a phenomenon of industrial relevance [97]. In this line, we have identified the application of ultrasound as essential tool for achieving dense packings in capillary columns [106] and HPLC microchips [107]. It leads to a smoother packing procedure and could induce bed consolidation by up to 10% after packing. Several other groups stated it also as beneficial, especially in terms of long-term column stability [17,71,101]. Application of these techniques during the column packing protocol should result in a steadier settling process and prevent the excessive formation of larger voids in the bed due to strong frictional and cohesive forces especially between small particles, which impede the required particle sliding.

1.4 Conclusions

In this study, we have demonstrated the existence of an optimal slurry concentration for packing columns under specific circumstances, but the work holds more general implications since our analysis addresses fundamental aspects of slurry preparation and stress-strain-flow behaviour relevant to the mechanics of column packing and bed compaction [16].

The ideal slurry concentration is ~ 20 mg/mL for the used packing protocol including $1.3 \mu\text{m}$ BEH particles, $75 \mu\text{m}$ i.d. columns, and a bed length of ~ 34 cm. The explanation for an optimal slurry concentration could be provided through the morphological analysis of a column produced with a low slurry concentration (10 mg/mL), the column produced with an intermediate slurry concentration of 20 mg/mL, which has shown the best chromatographic separation efficiency, and a column produced with a high slurry concentration (40 mg/mL). Two counteracting and counter-developing effects could be discriminated: The local porosity deviation in the wall region from bulk porosity values at low concentration and the increasing formation of larger voids in the bed with increasing slurry concentration. This experimental study confirms our predictions from the previous investigation [56]. The best separation efficiency is achieved as the structural deviations (mainly mean porosity) in the wall region are minimized, while formation of large packing voids does not reach a critical level yet. As discussed in Section 1.3.2.1 and in previous work, this wall effect leads to increasing transcolumn eddy dispersion. The number of larger voids is continuously increasing at higher slurry concentration. In addition, the formation of the largest voids, which can accommodate up to 99% of the particles from the PSD, could only be observed for the high slurry concentration of 40 mg/mL. The effect of the larger voids on column efficiency is more complex. Such voids likely influence transchannel and short-range interchannel dispersion and induce a long-range interchannel contribution (Section 1.3.2.2). Furthermore, an excess of larger voids in the wall region probably results in another transcolumn contribution. For a more detailed understanding of the effects induced by larger voids large-scale flow and transport

simulations in reconstructed beds covering the entire cross-section of the columns should be a powerful tool, as demonstrated before [13–15,27].

In our last study [56], we observed particle size segregation at low slurry concentrations, resulting in more smaller-than-average particles in the wall region. However, the effect could not be seen for the current set of columns, which is unsurprising for two reasons. First, size segregation was already less pronounced for the smaller particles used in that previous work (1.7 vs. 1.9 μm) at a slurry concentration of 3 mg/mL. This could be an indication that smaller particles show similar effects at lower slurry concentration; the particle size in the current study is even smaller. Second, size segregation previously occurred at a very low slurry concentration (3 mg/mL). The smallest concentration for an imaged packing was already 10 mg/mL for the new set of columns. Thus, size segregation occurring at very low slurry concentrations is likely to be suppressed at this point. It is also clear that the optimal slurry concentration strongly depends on the packing parameters, especially the particle diameter. The best column packed with the 1.9 μm particles from our previous study [56] was prepared with $c_{\text{slurry}} = 100$ mg/mL, which is much higher than the concentrations of 1.3 μm particles used in the present study (cf. Fig. 1.3A).

Another interesting aspect is the high external bed porosity in the bulk region of all three columns, reaching values of 0.47–0.50. These porosities are higher than expected with respect to values reported for the random-loose packing limit of frictional, cohesionless particles, or even the random-close packing limit of frictionless particles. The comparison with bulk porosities in columns packed with a similar procedure but different particle diameters [56] is interesting. There is a clear trend towards increasing external bed porosities with decreasing particle diameter: $\varepsilon_{\text{bulk}} = 0.39$ for 1.9 μm BEH particles, $\varepsilon_{\text{bulk}} = 0.44$ for 1.7 μm BEH particles, and $\varepsilon_{\text{bulk}} \approx 0.48$ for 1.3 μm BEH particles. This illuminates the increasing difficulty to achieve high bed densities with packing small, sub-2 μm frictional, cohesive particles, when interparticle forces become so important. Interestingly, all packings remained stable without bed collapse. Several possible explanations have been discussed in Section 1.3.2.1.

On the other hand, even these high external bed porosities (Table 1.1), a positive IPD (Table 1.3), and the presence of larger voids (Table 1.4) still enable excellent separation efficiencies (Fig. 1.3). Are these results contradictory? Actually, they make sense. (1) The optimized experimental setup (injection, frits, detection) engenders negligible extra-column band broadening to the investigated long (34 cm) capillary packings. (2) The small absolute dimension (75 μm) of the capillary column diameters results in fast (on molecular level) transcolumn exchange of analyte molecules between regions with different local flow velocities; any instant and fundamental column cross-sectional longitudinal velocity disparity is terminated quickly by the actual (velocity-dependent) transverse dispersion [78]. (3) The IPD values of all packed capillaries (IPD ~ 0.15), though larger than zero, are still small and should be regarded as characterizing relatively homogeneous packings, cf. Fig. 1.2 and Table 1.1 in [25]. (4) Numerical simulations of plate height curves in computer-generated packings with similar IPD (though at lower bed porosity, $\varepsilon_{\text{ext}} = 0.40$) yielded reduced plate height minima (h_{min}) below unity, cf. Figs. 2, 3, and 6 in [14] for IPDs < 0.15 . Introducing intraparticle porosity

with respect to the nonporous particles used in [14], cf. Fig. 1.6 in [108], and increasing the external porosity (at conserved IPD value) from, for example, $\varepsilon_{\text{ext}} = 0.40$ to 0.46 [93] is expected to offset these h_{min} -values on the order of $0.5 h$. This brings us quite close to the efficiency observed with the weakly retained analyte (hydroquinone, $k' = 0.2$) on the best packed column (20 mg/mL) in the present study ($h_{\text{min}} = 1.5$).

Taken together, this draws a consistent overall picture and confirms previous experimental [25] and simulation [14,93,108] work regarding the relative importance of column packing radial heterogeneity and average packing density. If distributed uniformly over the column cross-section, an increase of external porosity results in a moderate decrease of column efficiency compared with a more localized distribution of interparticle voidage in the (then more loosely packed) wall region, which will increase significantly IPDs and quickly deteriorate column efficiency. With respect to the void analysis and impact of larger voids on column efficiency, we also confirm implications of Schure and Maier [57], i.e., it is far more important to prevent larger voids or even gaps during column packing rather than obtaining the highest packing density. Again, if uniformly distributed over the column cross-section and stable in time, the adverse effect of lower than possible packing density on plate height is (much) smaller than the consequences of local defects or systematic radial packing heterogeneities. As we introduce a stronger radial non-uniformity at lower slurry concentrations or increase the number of larger voids at higher slurry concentrations, the increases in plate height (Fig. 1.3) with respect to the optimal 20 mg/mL slurry concentration for the current set of conditions can be readily explained.

These insights into the packing process provide a chance to achieve even higher efficiencies with capillary columns and column packings, in general. If a homogenous bed structure over the entire column cross-section can be realized and the formation of larger voids prevented at high slurry concentrations, e.g., due to the application of ultrasound, it may be possible to retain the advantages of a high slurry concentration (suppression of both porosity deviations in the wall region and particle size segregation) and avoid disadvantages due to the presence of larger voids.

Acknowledgement

The column preparation work reported in this manuscript was supported by Waters Corporation (Milford, MA).

References

- [1] J.W. Jorgenson, Capillary liquid chromatography at ultrahigh pressures, *Annu. Rev. Anal. Chem.* 3 (2010) 129–150.
- [2] Y. Shen, R. Zhang, R.J. Moore, J. Kim, T.O. Metz, K.K. Hixson, et al., Automated 20 kpsi RPLC-MS and MS/MS with chromatographic peak capacities of 1000-1500 and capabilities in proteomics and metabolomics, *Anal. Chem.* 77 (2005) 3090–3100.

-
- [3] F. Gritti, G. Guiochon, Accurate measurements of the true column efficiency and of the instrument band broadening contributions in the presence of a chromatographic column, *J. Chromatogr. A* 1327 (2014) 49–56.
- [4] L. Nováková, J.L. Veuthey, D. Guiochon, Practical method transfer from high performance liquid chromatography to ultra-high performance liquid chromatography: The importance of frictional heating, *J. Chromatogr. A* 1218 (2011) 7971–7981.
- [5] F. Gritti, M. Martin, G. Guiochon, Influence of viscous friction heating on the efficiency of columns operated under very high pressures, *Anal. Chem.* 81 (2009) 3365–3384.
- [6] A. de Villiers, H. Lauer, R. Szucs, S. Goodall, P. Sandra, Influence of frictional heating on temperature gradients in ultra-high-pressure liquid chromatography on 2.1 mm I.D. columns, *J. Chromatogr. A* 1113 (2006) 84–91.
- [7] J.J. DeStefano, S.A. Schuster, J.M. Lawhorn, J.J. Kirkland, Performance characteristics of new superficially porous particles, *J. Chromatogr. A* 1258 (2012) 76–83.
- [8] F. Gritti, M. Martin, G. Guiochon, Influence of pressure on the properties of chromatographic columns: II. The column hold-up volume, *J. Chromatogr. A* 1070 (2005) 13–22.
- [9] L.E. Blue, J.W. Jorgenson, 1.1 μm superficially porous particles for liquid chromatography. Part II: Column packing and chromatographic performance, *J. Chromatogr. A* 1380 (2015) 71–80.
- [10] F. Gritti, G. Guiochon, Perspectives on the evolution of the column efficiency in liquid chromatography, *Anal. Chem.* 85 (2013) 3017–3035.
- [11] G. Guiochon, T. Farkas, H. Guan-Sajonz, J.-H. Koh, M. Sarker, B.J. Stanley, et al., Consolidation of particle beds and packing of chromatographic columns, *J. Chromatogr. A* 762 (1997) 83–88.
- [12] R.A. Shalliker, B.S. Broyles, G. Guiochon, Physical evidence of two wall effects in liquid chromatography, *J. Chromatogr. A* 888 (2000) 1–12.
- [13] S. Khirevich, A. Höltzel, D. Hlushkou, U. Tallarek, Impact of conduit geometry and bed porosity on flow and dispersion in noncylindrical sphere packings, *Anal. Chem.* 79 (2007) 9340–9349.
- [14] S. Khirevich, A. Höltzel, A. Seidel-Morgenstern, U. Tallarek, Geometrical and topological measures for hydrodynamic dispersion in confined sphere packings at low column-to-particle diameter ratios, *J. Chromatogr. A* 1262 (2012) 77–91.
- [15] A. Daneyko, S. Khirevich, A. Höltzel, A. Seidel-Morgenstern, U. Tallarek, From random sphere packings to regular pillar arrays: Effect of the macroscopic confinement on hydrodynamic dispersion, *J. Chromatogr. A* 1218 (2011) 8231–8248.
- [16] B.G. Yew, J. Ureta, R.A. Shalliker, E.C. Drumm, G. Guiochon, Mechanics of column beds: II. Modeling of coupled stress-strain-flow behavior, *AIChE J.* 49 (2003) 642–664.
- [17] J.P.C. Vissers, H.A. Claessens, J. Laven, C.A. Cramers, Colloid chemical aspects of slurry packing techniques in microcolumn liquid chromatography, *Anal. Chem.* 67 (1995) 2103–2109.
-

-
- [18] J.P.C. Vissers, M.A. Hoeben, J. Laven, H.A. Claessens, C.A. Cramers, Hydrodynamic aspects of slurry packing processes in microcolumn liquid chromatography, *J. Chromatogr. A* 883 (2000) 11–25.
- [19] P.D.A. Angus, C.W. Demarest, T. Catalano, J.F. Stobaugh, Aspects of column fabrication for packed capillary electrochromatography, *J. Chromatogr. A* 887 (2000) 347–365.
- [20] J.J. Kirkland, J.J. DeStefano, The art and science of forming packed analytical high-performance liquid chromatography columns, *J. Chromatogr. A* 1126 (2006) 50–57.
- [21] M.F. Wahab, C.A. Pohl, C.A. Lucy, Colloidal aspects and packing behaviour of charged microparticulates in high efficiency ion chromatography, *J. Chromatogr. A* 1270 (2012) 139–146.
- [22] F. Capriotti, I. Leonardis, A. Cappiello, G. Famiglini, P. Palma, A fast and effective method for packing nano-LC columns with solid-core nano particles based on the synergic effect of temperature, slurry composition, sonication and pressure, *Chromatographia* 76 (2013) 1079–1086.
- [23] S. Fanali, S. Rocchi, B. Chankvetadze, Use of novel phenyl-hexyl core-shell particles in nano-LC, *Electrophoresis* 34 (2013) 1737–1742.
- [24] S. Bruns, D. Stoeckel, B.M. Smarsly, U. Tallarek, Influence of particle properties on the wall region in packed capillaries, *J. Chromatogr. A* 1268 (2012) 53–63.
- [25] S. Bruns, J.P. Grinias, L.E. Blue, J.W. Jorgenson, U. Tallarek, Morphology and separation efficiency of low-aspect-ratio capillary ultrahigh pressure liquid chromatography columns, *Anal. Chem.* 84 (2012) 4496–4503.
- [26] S. Jung, A. Höltzel, S. Ehlert, J.A. Mora, K. Kraiczek, M. Dittmann, et al., Impact of conduit geometry on the performance of typical particulate microchip packings, *Anal. Chem.* 81 (2009) 10193–10200.
- [27] S. Khirevich, A. Höltzel, S. Ehlert, A. Seidel-Morgenstern, U. Tallarek, Large-scale simulation of flow and transport in reconstructed microchip packings. *Anal. Chem.* 81 (2009) 4937–4945.
- [28] P. Levitz, Toolbox for 3D imaging and modeling of porous media: Relationship with transport properties, *Cem. Concr. Res.* 37 (2007) 351–359.
- [29] G. Möbus, B.J. Inkson, Nanoscale tomography in materials science, *Mater. Today*. 10 (2007) 18–25.
- [30] P.R. Shearing, D.J.L. Brett, N.P. Brandon, Towards intelligent engineering of SOFC electrodes: A review of advanced microstructural characterisation techniques, *Int. Mater. Rev.* 55 (2010) 347–363.
- [31] F. Tariq, P.D. Lee, R. Haswell, D.W. McComb, The influence of nanoscale microstructural variations on the pellet scale flow properties of hierarchical porous catalytic structures using multiscale 3D imaging, *Chem. Eng. Sci.* 66 (2011) 5804–5812.
- [32] S. Mitchell, N.-L. Michels, K. Kunze, J. Pérez-Ramírez, Visualization of hierarchically structured zeolite bodies from macro to nano length scales, *Nature Chem.* 4 (2012) 825–831.
-

-
- [33] A.P. Cocco, G.J. Nelson, W.M. Harris, A. Nakajo, T.D. Myles, A.M. Kiss, J.J. Lombardo, W.K.S. Chiu, Three-dimensional microstructural imaging methods for energy materials, *Phys. Chem. Chem. Phys.* 15 (2013) 16377–16407.
- [34] P.P.R.M.L. Harks, F.M. Mulder, P.H.L. Notten, In situ methods for Li-ion battery research: A review of recent developments, *J. Power Sources* 288 (2015) 92–105.
- [35] S. Wilhelm, B. Gröbler, M. Gluch, H. Heinz, *Confocal Laser Scanning Microscopy: Optical Image Formation and Electronic Signal Processing*, Monography, Carl Zeiss, Jena, Germany, 2008.
- [36] L. Holzer, M. Cantoni, Review of FIB-tomography, in: I. Utke, S. Moshkalev, Ph. Russell (Eds.), *Nanofabrication Using Focused Ion and Electron Beams: Principles and Applications*, Oxford University Press, New York, 2012, pp. 410–435.
- [37] A. Zankel, B. Kraus, P. Poelt, M. Schaffer, E. Ingolic, Ultramicrotomy in the ESEM, a versatile method for materials and life sciences, *J. Microsc.* 233 (2009) 140–148.
- [38] S. Bruns, U. Tallarek, Physical reconstruction of packed beds and their morphological analysis: Core-shell packings as an example, *J. Chromatogr. A* 1218 (2011) 1849–1860.
- [39] H. Jinnai, K. Nakanishi, Y. Nishikawa, J. Yamanaka, T. Hashimoto, Three-dimensional structure of a sintered macroporous silica gel, *Langmuir* 17 (2001) 619–625.
- [40] S. Bruns, T. Müllner, M. Kollmann, J. Schachtner, A. Hölzel, U. Tallarek, Confocal laser scanning microscopy method for quantitative characterization of silica monolith morphology, *Anal. Chem.* 82 (2010) 6569–6575.
- [41] H. Koku, R.S. Maier, K.J. Czymmek, M.R. Schure, A.M. Lenhoff, Modeling of flow in a polymeric chromatographic monolith, *J. Chromatogr. A* 1218 (2011) 3466–3475.
- [42] T. Müllner, A. Zankel, C. Mayrhofer, H. Reingruber, A. Hölzel, Y. Lv, et al., Reconstruction and characterization of a polymer-based monolithic stationary phase using serial block-face scanning electron microscopy, *Langmuir* 28 (2012) 16733–16737.
- [43] K. Hormann, T. Müllner, S. Bruns, A. Hölzel, U. Tallarek, Morphology and separation efficiency of a new generation of analytical silica monoliths, *J. Chromatogr. A* 1222 (2012) 46–58.
- [44] P. Aggarwal, V. Asthana, J.S. Lawson, H.D. Tolley, D.R. Wheeler, B.A. Mazzeo, M.L. Lee, Correlation of chromatographic performance with morphological features of organic polymer monoliths. *J. Chromatogr. A* 1334 (2014) 20–29.
- [45] Z. Saghi, P.A. Midgley, Electron tomography in the (S)TEM: From nanoscale morphological analysis to 3D atomic imaging, *Annu. Rev. Mater. Res.* 42 (2012) 59–79.
- [46] J. Zečević, K.P. de Jong, P.E. de Jongh, Progress in electron tomography to assess the 3D nanostructure of catalysts, *Curr. Opin. Solid State Mater. Sci.* 17 (2013) 115–125.
- [47] Y. Yao, K.J. Czymmek, R. Pazhianur, A.M. Lenhoff, Three-dimensional pore structure of chromatographic adsorbents from electron tomography, *Langmuir* 22 (2006) 11148–11157.

-
- [48] E.P.W. Ward, T.J.V. Yates, J.-J. Fernández, D.E.W. Vaughan, P.A. Midgley, Three-dimensional nanoparticle distribution and local curvature of heterogeneous catalysts revealed by electron tomography, *J. Phys. Chem. C* 111 (2007) 11501–11505.
- [49] J. Zečević, C.J. Gommers, H. Friedrich, P.E. de Jongh, K.P. de Jong, Mesoporosity of Zeolite Y: Quantitative three-dimensional study by image analysis of electron tomograms, *Angew. Chem. Int. Ed.* 51 (2012) 4213–4217.
- [50] D. Stoeckel, C. Kübel, K. Hormann, A. Höltzel, B.M. Smarsly, U. Tallarek, Morphological analysis of disordered macroporous–mesoporous solids based on physical reconstruction by nanoscale tomography, *Langmuir* 30 (2014) 9022–9027.
- [51] T. Müllner, A. Zankel, F. Svec, U. Tallarek, Finite-size effects in the 3D reconstruction and morphological analysis of porous polymers, *Mater. Today*. 17 (2014) 404–411.
- [52] S. Bruns, T. Hara, B.M. Smarsly, U. Tallarek, Morphological analysis of physically reconstructed capillary hybrid silica monoliths and correlation with separation efficiency, *J. Chromatogr. A* 1218 (2011) 5187–5194.
- [53] T. Müllner, A. Zankel, Y. Lv, F. Svec, A. Höltzel, U. Tallarek, Assessing structural correlations and heterogeneity length scales in functional porous polymers from physical reconstructions, *Adv. Mater.* 27 (2015) 6009–6013.
- [54] K. Hormann, U. Tallarek, Analytical silica monoliths with submicron macropores: Current limitations to a direct morphology-column efficiency scaling, *J. Chromatogr. A* 1312 (2013) 26–36.
- [55] D. Stoeckel, C. Kübel, M.O. Loeh, B.M. Smarsly, U. Tallarek, Morphological analysis of physically reconstructed silica monoliths with submicrometer macropores: Effect of decreasing domain size on structural homogeneity, *Langmuir* 31 (2015) 7391–7400.
- [56] S. Bruns, E.G. Franklin, J.P. Grinias, J.M. Godinho, J.W. Jorgenson, U. Tallarek, Slurry concentration effects on the bed morphology and separation efficiency of capillaries packed with sub-2 μm particles, *J. Chromatogr. A* 1318 (2013) 189–197.
- [57] M.R. Schure, R.S. Maier, How does column packing microstructure affect column efficiency in liquid chromatography? *J. Chromatogr. A* 1126 (2006) 58–69.
- [58] K.D. Patel, A.D. Jerkovich, J.C. Link, J.W. Jorgenson, In-depth characterization of slurry packed capillary columns with 1.0- μm nonporous particles using reversed-phase isocratic ultrahigh-pressure liquid chromatography, *Anal. Chem.* 76 (2004) 5777–5786.
- [59] U.D. Neue, *HPLC Columns: Theory, Technology and Practice*, Wiley-VCH, New York, 1997.
- [60] J.E. MacNair, K.C. Lewis, J.W. Jorgenson, Ultrahigh-pressure reversed-phase liquid chromatography in packed capillary columns, *Anal. Chem.* 69 (1997) 983–989.
- [61] J.E. MacNair, K.D. Patel, J.W. Jorgenson, Ultrahigh-pressure reversed-phase capillary liquid chromatography: Isocratic and gradient elution using columns packed with 1.0- μm particles, *Anal. Chem.* 71 (1999) 700–708.
- [62] J.S. Mellors, J.W. Jorgenson, Use of 1.5 micron porous ethyl-bridged hybrid particles as a stationary phase support for reversed-phase ultra-high pressure liquid chromatography, *Anal. Chem.* 76 (2004) 5441–5450.
-

-
- [63] A. Maiolica, D. Borsotti, J. Rappsilber, Self-made frits for nanoscale columns in proteomics, *Proteomics* 5 (2005) 3847–3850.
- [64] L.A. Knecht, E.J. Guthrie, J.W. Jorgenson, On-column electrochemical detector with a single graphite fiber electrode for open-tubular liquid chromatography, *Anal. Chem.* 56 (1984) 479–482.
- [65] S. Hsieh, J.W. Jorgenson, Preparation and evaluation of slurry-packed liquid chromatography microcolumns with inner diameters from 12 to 33 microns, *Anal. Chem.* 68 (1996) 1212–1217.
- [66] W.S. Rasband, ImageJ, U. S. National Institutes of Health, Bethesda, MD, <http://imagej.nih.gov/ij/>, 1997–2014.
- [67] F. Luisier, PureDenoise, Biomedical Imaging Group, École Polytechnique Fédéral de Lausanne, <http://bigwww.epfl.ch/algorithms/denoise/>, 2010.
- [68] C.A. Rimmer, C.R. Simmons, J.G. Dorsey, The measurement and meaning of void volumes in reversed-phase liquid chromatography, *J. Chromatogr. A* 965 (2002) 219–232.
- [69] S. Fanali, G. D’Orazio, T. Farkas, B. Chankvetadze, Comparative performance of capillary columns made with totally porous and core-shell particles coated with a polysaccharide-based chiral selector in nano-liquid chromatography and capillary electrochromatography, *J. Chromatogr. A* 1269 (2012) 136–142.
- [70] I. Nischang, Porous polymer monoliths: Morphology, porous properties, polymer nanoscale gel structure and their impact on chromatographic performance, *J. Chromatogr. A* 1287 (2013) 39–58.
- [71] M. Franc, J. Vojta, J. Sobotníková, P. Coufal, Z. Bosáková, Performance and lifetime of slurry packed capillary columns for high performance liquid chromatography, *Chem. Pap.* 68 (2014) 22–28.
- [72] A. Vaast, H. Terry, F. Svec, S. Eeltink, Nanostructured porous polymer monolithic columns for capillary liquid chromatography of peptides, *J. Chromatogr. A* 1374 (2014) 171–179.
- [73] T.J. Causon, I. Nischang, Critical differences in chromatographic properties of silica- and polymer-based monoliths, *J. Chromatogr. A* 1358 (2014) 165–171.
- [74] L.F.M. Coutinho, C.E.D. Nazario, A.M. Monteiro, F.M. Lancas, Novel devices for solvent delivery and temperature programming designed for capillary liquid chromatography, *J. Sep. Sci.* 37 (2014) 1903–1910.
- [75] S. Janků, V. Škeříková, J. Urban, Nucleophilic substitution in preparation and surface modification of hypercrosslinked stationary phases, *J. Chromatogr. A* 1388 (2015) 151–157.
- [76] T.J. Kaiser, J.W. Thompson, J.S. Mellors, J.W. Jorgenson, Capillary-based instrument for the simultaneous measurement of solution viscosity and solute diffusion coefficient at pressures up to 2000 bar and implications for ultrahigh pressure liquid chromatography, *Anal. Chem.* 81 (2009) 2860–2868.
- [77] J.C. Giddings, *Dynamics of Chromatography, Part 1: Principles and Theory*, Marcel Dekker, New York, NY, 1965.
-

-
- [78] A. Daneyko, D. Hlushkou, S. Khirevich, U. Tallarek, From random sphere packings to regular pillar arrays: Analysis of transverse dispersion, *J. Chromatogr. A* 1257 (2012) 98–115.
- [79] E. Hamdan, J.F. Milthorpe, J.C.S. Lai, An extended macroscopic model for solute dispersion in confined porous media, *Chem. Eng. J.* 137 (2008) 614–635.
- [80] S. Khirevich, A. Höltzel, A. Seidel-Morgenstern, U. Tallarek, Time and length scales of eddy dispersion in chromatographic beds, *Anal. Chem.* 81 (2009) 7057–7066.
- [81] V. Baranau, U. Tallarek, Random-close packing limits for monodisperse and polydisperse hard spheres, *Soft Matter* 10 (2014) 3826–3841.
- [82] G.Y. Onoda, E.G. Liniger, Random loose packings of uniform spheres and the dilatancy onset, *Phys. Rev. Lett.* 64 (1990) 2727–2730.
- [83] Z.P. Zhang, L.F. Liu, Y.D. Yuan, A.B. Yu, A simulation study of the effects of dynamic variables on the packing of spheres, *Powder Technol.* 116 (2001) 23–32.
- [84] C. Song, P. Wang, H.A. Makse, A phase diagram for jammed matter, *Nature* 453 (2008) 629–632.
- [85] M. Jerkins, M. Schröter, H.L. Swinney, T.J. Senden, M. Saadatfar, T. Aste, Onset of mechanical stability in random packings of frictional spheres, *Phys. Rev. Lett.* 101 (2008) 018301.
- [86] G.R. Farrell, K.M. Martini, N. Menon, Loose packings of frictional spheres, *Soft Matter* 6 (2010) 2925–2930.
- [87] L.E. Silbert, Jamming of frictional spheres and random loose packing, *Soft Matter* 6 (2010) 2918–2924.
- [88] K.D. Wyndham, J.E. O’Gara, T.H. Walter, K.H. Glose, N.L. Lawrence, B.A. Alden, et al., Characterization and evaluation of C18 HPLC stationary phases based on ethyl-bridged hybrid organic/inorganic particles, *Anal. Chem.* 75 (2003) 6781–6788.
- [89] R.Y. Yang, R.P. Zou, A.B. Yu, Computer simulation of the packing of fine particles, *Phys. Rev. E* 62 (2000) 3900–3908.
- [90] A.B. Yu, C.L. Feng, R.P. Zou, R.Y. Yang, On the relationship between porosity and interparticle forces, *Powder Technol.* 130 (2003) 70–76.
- [91] K.J. Dong, R.Y. Yang, R.P. Zou, A.B. Yu, Role of interparticle forces in the formation of random loose packing, *Phys. Rev. Lett.* 96 (2006) 145505.
- [92] J.M. Valverde, A. Castellanos, Random loose packing of cohesive granular materials, *Europhys. Lett.* 75 (2006) 985–991.
- [93] A. Daneyko, A. Höltzel, S. Khirevich, U. Tallarek, Influence of the particle size distribution on hydraulic permeability and eddy dispersion in bulk packings, *Anal. Chem.* 83 (2011) 3903–3910.
- [94] L.A. Pughaloni, G.C. Barker, Structure and distribution of arches in shaken hard sphere deposits, *Physica A* 337 (2004) 428–442.
- [95] R. Arévalo, D. Maza, L.A. Pughaloni, Identification of arches in two-dimensional granular packings, *Phys. Rev. E* 74 (2006) 021303.
- [96] G. Mallol, J.L. Amorós, M.J. Orts, D. Llorens, Densification of monomodal quartz particle beds by tapping, *Chem. Eng. Sci.* 63 (2008) 5447–5456.
-

-
- [97] A. Mehta, Spatial, dynamical and spatiotemporal heterogeneities in granular media, *Soft Matter* 6 (2010) 2875–2883.
- [98] A. Garcimartín, I. Zuriguel, L.A. Pugnaloni, A. Janda, Shape of jamming arches in two-dimensional deposits of granular materials, *Phys. Rev. E* 82 (2010) 031306.
- [99] M.C. Jenkins, M.D. Haw, G.C. Barker, W.C.K. Poon, S.U. Egelhaaf, Finding bridges in packings of colloidal spheres, *Soft Matter* 7 (2011) 684–690.
- [100] C.M. Carlevaro, L.A. Pugnaloni, Arches and contact forces in a granular pile, *Eur. Phys. J. E* 35 (2012) 44.
- [101] R.A. Shalliker, B.S. Broyles, G. Guiochon, Evaluation of the secondary consolidation of columns for liquid chromatography by ultrasonic irradiation, *J. Chromatogr. A* 878 (2000) 153–163.
- [102] C.X. Li, X.Z. An, R.Y. Yang, R.P. Zou, A.B. Yu, Experimental study on the packing of uniform spheres under three-dimensional vibration, *Powder Technol.* 208 (2011) 617–622.
- [103] C. Lozano, G. Lumay, I. Zuriguel, R.C. Hidalgo, A. Garcimartín, Breaking arches with vibrations: The role of defects, *Phys. Rev. Lett.* 109 (2012) 068001.
- [104] C. Lozano, I. Zuriguel, A. Garcimartín, Stability of clogging arches in a silo submitted to vertical vibrations, *Phys. Rev. E* 91 (2015) 062203.
- [105] S. Kiesgen de Richter, C. Hanotin, P. Marchal, S. Leclerc, F. Demeurie, N. Louvet, Vibration-induced compaction of granular suspensions, *Eur. Phys. J. E* 38 (2015) 74.
- [106] S. Ehlert, T. Rösler, U. Tallarek, Packing density of slurry-packed capillaries at low aspect ratios, *J. Sep. Sci.* 31 (2008) 1719–1728.
- [107] S. Ehlert, K. Kraiczek, J.A. Mora, M. Dittmann, G.P. Rozing, U. Tallarek, Separation efficiency of particle-packed HPLC microchips, *Anal. Chem.* 80 (2008) 5945–5950.
- [108] A. Daneyko, D. Hlushkou, V. Baranau, S. Khirevich, A. Seidel-Morgenstern, U. Tallarek, Computational investigation of longitudinal diffusion, eddy dispersion, and trans-particle mass transfer in bulk, random packings of core–shell particles with varied shell thickness and shell diffusion coefficient, *J. Chromatogr. A* 1407 (2015) 139–156.

Chapter 2

Bed morphological features associated with an optimal slurry concentration for reproducible preparation of efficient capillary ultrahigh pressure liquid chromatography columns

Authors

Arved E. Reising, Justin M. Godinho, James W. Jorgenson, and Ulrich Tallarek

State of publication

Published 4 May 2017 in *Journal of Chromatography A*, Vol. 1504, pp. 71–82.

Abstract

Column wall effects and the formation of larger voids in the bed during column packing are factors limiting the achievement of highly efficient columns. Systematic variation of packing conditions, combined with three-dimensional bed reconstruction and detailed morphological analysis of column beds, provide valuable insights into the packing process. Here, we study a set of sixteen 75 μm i.d. fused-silica capillary columns packed with 1.9 μm , C18-modified, bridged-ethyl hybrid silica particles slurried in acetone to concentrations ranging from 5 to 200 mg/mL. Bed reconstructions for three of these columns (representing low, optimal, and high slurry concentrations), based on confocal laser scanning microscopy, reveal morphological features associated with the implemented slurry concentration, that lead to differences in column efficiency. At a low slurry concentration, the bed microstructure includes systematic radial heterogeneities such as particle size-segregation and local deviations from bulk packing density near the wall. These effects are suppressed (or at least reduced) with higher slurry concentrations. Concomitantly, larger voids (relative to the mean particle diameter) begin to form in the packing and increase in size and number with the slurry concentration. The most efficient columns are packed at slurry concentrations that balance these counteracting effects. Videos are taken at low and high slurry concentration to elucidate the bed formation process. At low slurry concentrations, particles arrive and settle individually, allowing for rearrangements. At high slurry concentrations they arrive and pack as large patches (reflecting particle aggregation in the slurry). These processes are discussed with respect to column packing, chromatographic performance, and bed microstructure to help reinforce general trends previously described. Conclusions based on this comprehensive analysis guide us towards further improvement of the packing process.

2.1 Introduction

Capillary columns with bed lengths up to one meter packed with sub-2 μm particles can achieve impressive separation efficiencies, with theoretical plate numbers of $\sim 500,000$ per meter [1,2]. However, effective utilization of these small particles and capillary columns is plagued by a number of challenges addressing high column backpressure [3], extra-column band broadening [4–6], frictional heating [7–9], and radial expansion of the column under high pressure [10]. The small column inner diameter, the long column bed, and the small particle diameter result in additional challenges to achieve a homogenous bed structure with the packing process. Main morphological features that limit separation efficiency are larger voids in the bed, large enough to accommodate whole particles [2], and transcolumen heterogeneities, which operate over the column cross-section and become the major contributor to chromatographic band broadening for capillary and analytical columns [2,11–18].

Detailed knowledge of the bed structure in chromatographic columns is key to understanding column performance. During the last decades, column packing started to not only be based on empirical optimization of the packing protocol, but also on an understanding of the process itself [14,19–24]. A number of important parameters and their often-complex influences were identified and correlated with the separation efficiency. These include the width and shape of the particle size distribution (PSD) and surface properties of the particles [6,11], the inner diameter of capillary columns [12], the conduit geometry, in particular, of HPLC microchips [25,26], and the slurry concentration [2,13]. Modern three-dimensional (3D) imaging techniques provide insights into the relationship between morphological properties of porous materials and their performance in targeted applications [27–31]. 3D reconstructions of column beds as well as computer-generated packings have been used to analyse and simulate the effect of bed morphology on relevant transport properties [32–37].

In a very recent study [2], we identified an optimal slurry concentration within a given set of packing parameters for 1.3 μm fully porous bridged-ethyl hybrid (BEH) silica particles packed into 75 μm i.d. capillary columns (~ 30 cm bed length) and explored bed morphological features for selected columns to explain their different separation efficiencies. We proposed an optimal slurry concentration would depend on the packing conditions and is highly influenced by the actual parameters of the packing protocol. For further investigation of optimal packing conditions, we prepared a new set of sixteen columns (75 μm i.d., ~ 45 cm bed length) packed with conventional 1.9 μm BEH silica particles at slurry concentrations from 5 to 200 mg/mL. Videos were recorded during column packing to illustrate the different bed formation processes at low and high slurry concentration. Based on chromatographic characterization, three columns (representing low, intermediate, and high slurry concentration) were selected for 3D reconstruction of their packing microstructure using confocal laser scanning microscopy (CLSM). Transcolumen heterogeneities at low slurry concentrations could be identified as efficiency-limiting factors from the analysis of radial porosity profiles and the radial distribution of the mean particle diameter (d_p). We also investigated the presence of larger voids in the packings that can accommodate a particle of the size of d_p . Characteristic features of the packings were correlated with separation efficiencies and visual observations from the packing process. The results are used to shape our knowledge of the packing process, to confirm general

trends on the optimal slurry concentration in dependence of the packing protocol, and to suggest possibilities for optimization of the packing process towards higher separation efficiencies. In fact, the insights gained from this detailed study in combination with our previous work already allowed us to improve the packing procedure and create extremely efficient capillary columns [38].

2.2 Experimental

2.2.1 Chemicals and materials

75 μm i.d. cylindrical fused-silica tubing was purchased from Polymicro Technologies (Phoenix, AZ). Capillaries were packed with C18-modified 1.9 μm BEH silica particles provided by Waters Corporation (Milford, MA). HPLC grade acetonitrile, acetone (reagent grade), trifluoroacetic acid (TFA), and the test analytes for chromatographic characterization (L-ascorbic acid, hydroquinone, resorcinol, catechol, 4-methyl catechol) came from Fisher Scientific (St. Louis, MO). Kasil frits for packed capillaries were prepared with potassium silicate from PQ Corporation (Valley Forge, PA) and formamide from Sigma-Aldrich (St. Louis, MO). HPLC grade water for chromatographic experiments was obtained from a Millipore NANOpure water system (Billerica, MA). HPLC grade acetone (staining solvent) was supplied by Fisher Scientific (Loughborough, UK). Fluorescent dye BODIPY 493/503 (Life Technologies, Darmstadt, Germany) was used for staining prior to imaging. Glycerol and dimethyl sulfoxide (DMSO) employed for matching the liquid's refractive index to that of the BEH particles were purchased from Carl Roth (Karlsruhe, Germany). HPLC grade water used during refractive index matching came from a Milli-Q gradient purification system (Merck Millipore, Darmstadt, Germany).

2.2.2 Preparation of capillary UHPLC columns

The packing of the capillary UHPLC columns will be only briefly described here, since it has been explained in great detail before [39–43]. Column blanks were fritted using the Kasil method [44]. Capillary tubing was pushed onto a glass microfiber filter (Reeve Angel, Clifton, NJ) wetted with 50/50 (v/v) potassium silicate/formamide. The column blanks were then dried overnight at 50 °C. Resulting frits were ~ 125 μm in length. Particle slurries were prepared by mixing a known mass of the particles in a known volume of acetone. Acetone was chosen because C18-modified BEH particles slurry well in this solvent and to mirror previous studies for comparison [2,13,38]. The following slurry concentrations were used: 5, 20, 40, 60, 80, 100, 120, 140, 160, 180, and 200 mg/mL. The particles were suspended with a 10 min sonication cycle prior to packing using a Cole Parmer Ultrasonic Cleaner 8891 (Vernon Hills, IL). The slurry was then placed into a packing reservoir containing a magnetic stirrer for agitation during packing. The column blank was secured to the reservoir using an UHPLC fitting. Packing was initiated using acetone as pushing solvent at 150 bar from a DSHF-300 Haskel pump (Burbank, CA). Packing pressure was immediately raised to 2000 bar when 2 cm of column were packed. Columns were allowed to pack until a bed length of 50 cm was reached. The time required for

this bed length decreased substantially with increasing slurry concentration: it took ~6800 seconds for the 5 mg/mL slurry and only ~250 seconds with 200 mg/mL. Packing pressure was then slowly released to atmospheric pressure and the column was connected to a DSXHF-903 Haskel pump using an UHPLC injection apparatus. Each column was flushed for 1 h in 50/50 (v/v) water/acetonitrile with 0.1% TFA at 3500 bar, after which pressure was gradually released and reinitiated at 700 bar to form a temporary inlet frit with a heated wire stripper from Teledyne Interconnect Devices (San Diego, CA). Packed columns were clipped to a ~45 cm bed length and an inlet frit was installed using the Kasil method.

2.2.3 Acquisition of videos during the packing process

The packing process was observed with a Wolfe oil immersion microscope equipped with a 100x oil immersion objective (Carolina Biological Supply Company, Burlington, NC). Videos were output through a USB 2.0 S-Video and composite video capture cable (StarTech.com, Lockbourne, OH) and recorded using GrabBee software (VideoHome Technology Corp., New Taipei City, Taiwan). Acquisition of the videos started after ~10 cm of the bed were generated. During the capturing time a few centimetres of bed formed at maximum.

2.2.4 Chromatographic characterization

Column efficiency was analysed under isocratic elution conditions using 200 μM of a test mixture (L-ascorbic acid, dead-time marker; hydroquinone, resorcinol, catechol, and 4-methyl catechol in the mobile phase) and an UHPLC injection apparatus [39–42]. The mobile phase used for evaluation was 50/50 (v/v) water/acetonitrile with 0.1% TFA. The analytes were detected amperometrically. Electrochemical detection was realized at a $8 \mu\text{m} \times 300 \mu\text{m}$ carbon fibre microelectrode held at +1.1 V vs. Ag/AgCl reference electrode [45]. This electrode was placed at the outlet of the UHPLC column. Current-to-voltage conversion was conducted with an SR750 current amplifier (Stanford Research Systems, Sunnyvale, CA) with 10^9 V/A gain and 3 Hz, 3 dB low-pass bandwidth filter. An Intel Core 2 Duo desktop computer with 16-bit A/D converter was used to acquire data at 21 Hz. Data were collected with a custom-written LabView 6.0 program (National Instruments, Austin, TX). Columns were analysed over a range of mobile phase velocities to create plots of the plate height H vs. the average mobile phase velocity u_{av} for each analyte in the test mixture. High frequency noise was removed from chromatograms using a digital frequency filter, low frequency baseline drift was eliminated by background subtraction. Retention times and theoretical plate counts N were determined using an iterative statistical moments algorithm ($\pm 3 \sigma$) written in Igor Pro 6.0 (Wavemetrics, Inc., Lake Oswego, OR) [46].

2.2.5 Imaging of packing microstructure

The three selected columns were prepared for CLSM imaging following established procedures [2,12,47,48]. Detection windows on the packed columns were created at about 2/3 of the packed bed length from the inlet (i.e., after ~30 cm) using a drop of warm sulphuric acid. Columns were flushed with at least 10 bed volumes of dye solution in acetone (0.5 mg/mL) to achieve

sufficient staining of the reversed-phase surface of the particles with the fluorescent dye BODIPY 493/503. Afterwards, columns were flushed for at least 10 h at 500 bar with refractive index matching liquid, i.e., 70/19/11 (v/v/v) glycerol/DMSO/water, calibrated to a refractive index of $n_D = 1.4582$ using an AR200 digital refractometer (Reichert Analytical Instruments, Depew, NY). After sealing the column ends with nail polish to avoid air intrusion and partly evaporation of matching liquid, the columns were fixed on a microscope slide and transferred to the confocal microscope (Leica TCS SP5, equipped with a HCX PL APO 63x/1.3 GLYC CORR CS (21°) glycerol immersion objective lens, Leica Microsystems, Wetzlar, Germany). The refractive index matching liquid was used as an embedding medium for the samples and as lens immersion medium. The optical setup has been described in detail before [48]. Excitation of the dye at 488 nm was achieved using an Argon laser. The microscope pinhole was set to 0.5 AU and the detection interval from 491 to 515 nm. Image slices were acquired perpendicular to the capillary axis. Pixel size within a stack was set to 30 nm and the step size between slices to 126 nm, both complying with the Nyquist sampling criterion. Example slices of the image stack acquired for the column packed at a slurry concentration of 20 mg/mL are shown as ortho-slice image in Fig. 2.1A.

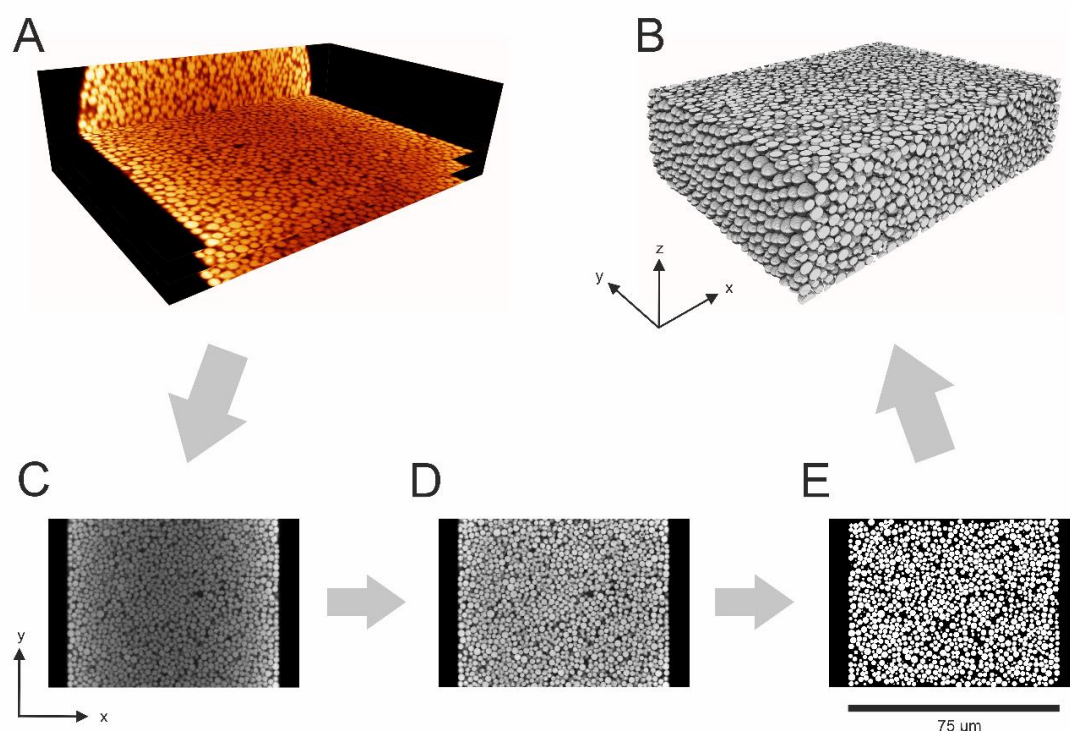


Fig. 2.1. Illustration of the reconstruction process for the capillary column packed with 1.9 μm BEH silica particles at a slurry concentration of 20 mg/mL. (A) Orthoslice view of CLSM raw images from the capillary (as seen at the microscope), three of the acquired slices are shown exemplarily with a distance of 4 μm between them. (B) 3D rendering of the final reconstruction (75 $\mu\text{m} \times 55 \mu\text{m} \times 20 \mu\text{m}$). (C–E) Reconstruction process demonstrated for the central slice of the column from the raw image (C) via the restored image (D) to the reconstructed image (E).

2.2.6 Image restoration and bed reconstruction

The restoration and reconstruction process is illustrated in Fig. 2.1, which also provides the definition of the axes used for the remainder of the discussion. Image quality of the raw images (Fig. 2.1A and C) from the microscope was enhanced in a multiple-step process following established procedures [2,12,47,48]. If not stated otherwise, custom software written in C# using Microsoft Visual Studio 2008, 2012, and 2013 (Microsoft Corporation, Redmond, WA) was used. The following steps were applied for image restoration:

1. A deconvolution process was applied to increase contrast and resolution and also to remove Poisson noise from the images using Huygens maximum likelihood iterative deconvolution (Scientific Volume Imaging, Hilversum, The Netherlands).
2. If the column was not exactly aligned with the y -axis, the images were rotated to achieve a perfect alignment using ImageJ [49].
3. Intensity variations in an image slice due to different material thickness above the slice and non-uniform detector sensitivity were corrected. A fourth-order polynomial fit was applied to mean values along the x - and y -axis to normalize intensity in the slice.
4. Bleaching of dye and intensity loss at increasing measurement depth were corrected using a second-order exponential decay for mean intensities in the centre of every slice.
5. Shifts in x -direction between images were corrected using the position of the column wall in every slice as reference.
6. Errors in the width of the z -step due to a defect in the sample table and external vibrations were corrected by identifying affected slices based on an autocorrelation script designed in MATLAB R2014b (The MathWorks, Inc., Natick, MA) applied to neighbouring slices and on identification of z -dependent irregularities in mean intensities of the slices after the first reconstruction process (described in the following paragraph). The reconstruction process was repeated after correction to avoid artefacts.

An example slice from the restored image stack is shown in Fig. 2.1D. To provide a detailed representation of the structure for further analysis, the position and radius of every particle in the reconstructed section have to be determined. The applied procedure has been described in detail before [2,11–13,48]. Briefly, the following steps were applied:

1. Positions of the particle centres were estimated using ImageJ [49]. A variance filter was applied to a duplicate of the stack and an unsharp mask was applied to another duplicate, both followed by application of a threshold. A logical AND operation of the two resulting images provided a stack showing only centres of the particles as white. This stack was used to calculate initial particle positions [12]. The resulting list was cleaned from positions with a very small radius, positions close to image borders, positions in dark spots, and positions very close to each other.
2. The provided list of initial particle positions was used as input for a fitting algorithm. A number of circles with increasing diameter around the coordinate was analysed until mean intensity of a circle or the variance within the circle reached a specified threshold. This procedure was repeated with x -, y -, and z -variation around the initial position to

determine the largest fitting particle. The resulting “best centre” and corresponding radius were saved to describe the particle.

3. The fitting procedure was repeated several times with a variation of threshold parameters to determine the ideal set of fitting parameters for the individual image stack. The best set of parameters was chosen based on several criteria: (i) best compliance of the resulting PSD with the PSD recorded from scanning electron microscopy (SEM) data (cf. Section 2.2.8), (ii) minimization of the number of particles showing unrealistic overlap with neighbouring particles, (iii) minimization of the number of particles lacking contact with neighbouring particles, and (iv) maximization of optical quality using an overlay of the enhanced image stack with the spheres resulting from the fit.
4. Obvious errors were removed from the list. This included the removal of particles showing strong overlap and isolated particles, as well as an optical control for misfits.
5. Remaining particles that could not be determined correctly by the algorithm were marked manually.
6. The resulting list of particle positions and particle radii was used to draw an image stack of spheres assuming perfect sphericity.
7. Non-spherical fragments were drawn manually based on the original image stack and added to the sphere image stack to ensure a complete representation of the packing. The resulting binarized image stacks are referred to as “reconstructions” in the remainder of the paper. A reconstructed slice and a 3D-rendering of the reconstructed stack are shown in Fig. 2.1E and Fig. 2.1B, respectively.

2.2.7 Analysis of reconstructions

For accurate analysis of a reconstruction the exact distance between slices, the exact position of the column wall, and the centre of the column have to be determined. An xz -image of mean intensity along the column axis was calculated from the reconstruction. For every z -position, the first two points below a specified intensity threshold (viewing from the central x -position of each slice) were determined as wall points. An ellipse fit was applied to the list of wall points in MATLAB R2014b providing centre coordinates, radius, and the exact distance between slices.

The binarized image stack, the list of particles, and the calculated parameters for each column were used to analyse the following properties. Radial profiles of the external porosity, $\varepsilon(r)$, were derived by counting black voxels (the interparticle void) and white voxels (particles) in cylindrical shells obtained by scaling shell boundaries around the column centre with a shell size of 270 nm and a step size of 90 nm. Relative radial porosity profiles $\varepsilon_{\text{rel}}(r) = \varepsilon(r) - \varepsilon_{\text{bulk}}$ were prepared by subtracting the bulk porosity value $\varepsilon_{\text{bulk}}$ from the local porosity profile $\varepsilon(r)$, with $r = 0$ at the wall. The integral porosity deviation (IPD) introduced in [11,12] was calculated by integration of the relative porosity profiles. Several integration limits were used to identify and analyse different regions, as discussed in detail in Section 2.3.2.1. Radial profiles of the mean particle diameter d_p were derived by assigning each particle according to its centre coordinate to a cylindrical shell obtained by scaling the shell boundaries around the column

centre with a shell size of 5.5 μm and a step size of 90 nm. Packing voids were identified by inscribing spheres into the void space of a reconstruction, as introduced before in [2].

2.2.8 Scanning electron microscopy

The BEH particles in the capillary packed at a slurry concentration of 5 mg/mL were subsequently flushed out of the column with ethanol as the pushing solvent, after cutting off the column end and applying a pressure of 200 bar. The particles were washed four times with a mixture of ethanol and acetone, including a drying step between each washing step. Afterwards, particles were dried for three days and mounted onto a carbon film on a sample holder. Loose particles were removed by a stream of compressed air. The sample was sputtered with platinum for 90 s and transferred into the SEM chamber of a JSM-7500F scanning electron microscope (JEOL, München, Germany). Images were acquired using either the lower secondary electron image at a working distance of 8 mm or the secondary electron image at a working distance of 5 mm. Image resolution was set to 1280 \times 940 pixels with 3000x magnification for PSD determination. Particle diameters were extracted by overlaying circles in the images using the same in-house written software as applied to the CLSM images to ensure maximal comparability.

2.3 Results and discussion

2.3.1 Kinetic performance of the packed columns

A set of sixteen capillary columns (75 μm i.d.) was packed with fully porous 1.9 μm C18-modified BEH silica particles applying slurry concentrations (c_{slurry}) from 5 to 200 mg/mL. Bed lengths were \sim 45 cm. Column packing was repeated to investigate reproducibility for slurry concentrations of 20, 80, and 140 mg/mL. Columns were characterized under isocratic elution conditions using 50/50 (v/v) water/acetonitrile with 0.1% TFA as the eluent. Hydroquinone is weakly retained under these conditions ($k' = 0.20$) and is thus a suitable indicator of the fluid dynamics in the packings and the actual interparticle flow heterogeneity. The minimum plate height H_{min} for hydroquinone on the set of columns is summarized in Fig. 2.2A. Data for 4-methyl catechol, a moderately retained analyte, is nearly indistinguishable. The figure shows that packing reproducibility depends on slurry concentration and improves strongly from 20 to 140 mg/mL. This improvement culminates in the practically indistinguishable column efficiencies at $c_{\text{slurry}} = 140$ mg/mL ($H_{\text{min}} = 2.83$ μm), before plate heights increase for $c_{\text{slurry}} > 160$ mg/mL. The figure communicates that high separation efficiency ($H_{\text{min}} < 3$ μm) is reproducibly observed when using high slurry concentrations of about 140–160 mg/mL for column packing.

To identify and analyse bed morphological features responsible for the differences in column efficiencies (Fig. 2.2A), three columns were selected for physical reconstruction and morphological analysis. The selected columns include one 20 mg/mL column to represent low slurry concentration, one of the two 140 mg/mL columns with nearly identical performance, representing optimal intermediate slurry concentration, and the 200 mg/mL column for a too-high slurry concentration. Full plate height plots ($H-u_{\text{av}}$) of these columns are shown in

Fig. 2.2B. The 140 mg/mL column has a reduced minimum plate height, calculated with the Sauter mean particle diameter (d_s), of $h_{\min} = H_{\min}/d_s = 1.40$ and a plate count of $N = 1.59 \times 10^5$ (corresponding to 3.53×10^5 N/m), characteristic of a highly efficient column. The other two columns show higher minimum reduced plate heights, i.e., a h_{\min} of 2.17 for 20 mg/mL and of 1.78 for 200 mg/mL, as well as a stronger slope of their $H-u_{\text{av}}$ plots towards high velocities.

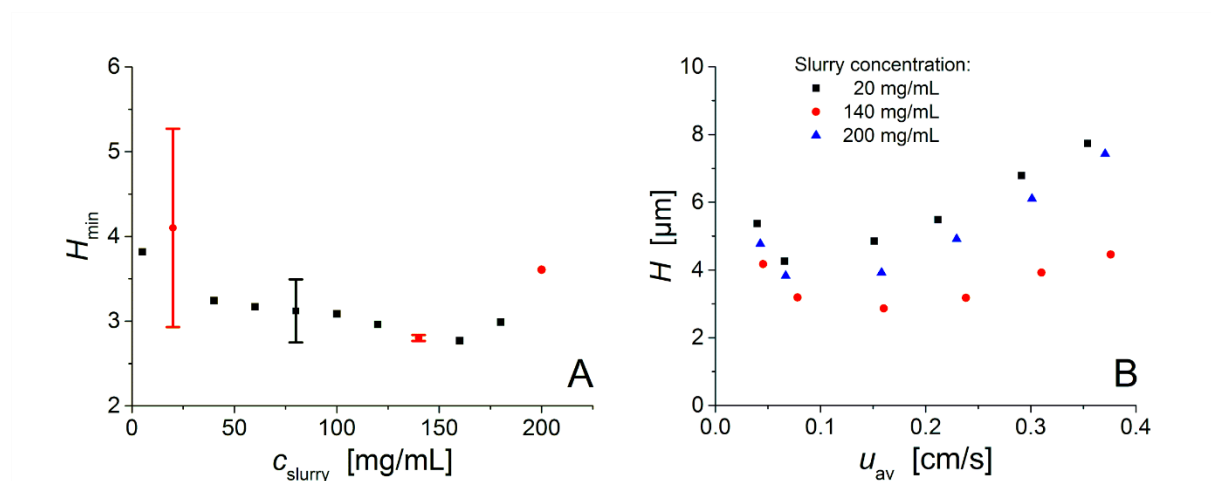


Fig. 2.2. Column efficiency as a function of the slurry concentration (c_{slurry}). (A) Plate height minima H_{\min} (extracted from the full plate height curves) vs. the slurry concentration c_{slurry} for the entire set of sixteen capillary columns packed with $1.9 \mu\text{m}$ C18-modified BEH silica particles applying c_{slurry} from 5 to 200 mg/mL. Data with error bars indicate packing reproducibility. Red circles denote the three slurry concentrations at which columns were selected for CLSM-based reconstruction and analysis of bed microstructure. (B) Plate height curves of the columns selected for reconstruction and morphological analysis: plate height for hydroquinone in 50/50 (v/v) water/acetonitrile mobile phase ($k' = 0.2$) vs. the average mobile flow velocity.

Capillary columns analysed in this study have a ratio of bed length to column diameter (L_{bed}/d_c) of ~ 6000 . Under these conditions, the transient longitudinal dispersion coefficient at a given velocity reaches its asymptotic (long-time) limit and becomes constant [50], i.e., full lateral equilibration of analytes between all scales of flow heterogeneities over the column cross-section can be assumed. A detailed physico-chemical characterization of the hydrodynamics in the packings is realized with the Giddings equation [51]. Giddings developed a plate height equation by analogy to conductors in parallel, applying the random-walk relationship to a model of eddy dispersion incorporating the coupling between transverse diffusion and spatial velocity fluctuations (i.e., diffusion and flow mechanisms). The Giddings equation provides a description of individual contributions to the plate height due to eddy dispersion operating on different time and length scales [2,12,16,51]:

$$h = \frac{b}{v} + \sum_{i=1}^3 \frac{2\lambda_i}{1 + \left(\frac{2\lambda_i}{\omega_i}\right)v^{-1}} + cv \quad (2.1)$$

In Eq. (2.1), $v = u_{av}d_S/D_m$ denotes the reduced velocity and D_m is the pressure-dependent diffusion coefficient of the analyte in the bulk mobile phase. The b -term accounts for longitudinal diffusion along the column, the c -term for the mass transfer kinetics into and across the fully porous BEH particles used in this study. The remaining three terms $h_{eddy,i}$ in Eq. (2.1) describe eddy dispersion on different time and length scales, where ω_i and λ_i are structural parameters characteristic of each contribution. The term for $i = 1$ represents the transchannel contribution in individual channels between particles, the term for $i = 2$ represents the short-range interchannel contribution due to biases in the average interstitial velocity on the scale of ~ 2 particle diameters, and the term for $i = 3$ represents the transcolumn contribution due to packing inhomogeneities operating over the entire column cross-section.

Another parameter characteristic of each eddy dispersion contribution is the reduced transition velocity $v_{1/2,i} = 2\lambda_i/\omega_i$ at which the corresponding plate height term $h_{eddy,i}$ in Eq. (2.1) reaches half of its limiting value and thereafter starts to flatten noticeably [51]. At high velocities $h_{eddy,i}$ approaches the constant value $2\lambda_i$, whereas at low velocities $h_{eddy,i}$ approaches $\omega_i v$ and is thus proportional to velocity. From our previous analysis we obtained the following values for the transition velocities characterizing the three eddy dispersion contributions in Eq. (2.1): $v_{1/2,1} \approx 200$ (transchannel), $v_{1/2,2} \approx 4$ (short-range interchannel), and $v_{1/2,3} > 200$ (transcolumn) [34,52]. The reduced transition velocity is a rough dividing point between the dominance of diffusion and flow mechanisms of lateral exchange in a packing at lower and higher velocities, respectively. The high transition velocities for the transchannel and transcolumn contributions indicate that over a wide range of reduced velocities, certainly in chromatographic practice with $v < 30$ (as in this work), these effects lose their coupling characteristics between diffusion and flow mechanisms of eddy dispersion. They reduce to simple mass transfer velocity-proportional terms, i.e., with $(2\lambda_i/\omega_i) \gg v$, the transchannel and transcolumn contributions can be expressed just as $\omega_i v$. Of the three eddy dispersion contributions only the short-range interchannel dispersion retains its coupling characteristic and Eq. (2.1) can be simplified as follows:

$$h \approx \frac{b}{v} + \omega_1 v + \frac{2\lambda_2}{1 + \left(\frac{2\lambda_2}{\omega_2}\right)v^{-1}} + \omega_3 v + cv \quad (2.2)$$

Eq. (2.2) implies that the slope of the $H-u_{av}$ plots at velocities beyond the plate height minimum (cf. Fig. 2.2B) can be connected to three different terms, in general: The transchannel and transcolumn eddy dispersion terms ($\omega_1 v$ and $\omega_3 v$) and intraparticle mass transfer resistance (cv). However, the mass transfer contribution cannot be responsible for differences in column efficiency in this entire set of columns, since they were packed with the same batch of particles. That is, diffusion into and across porous particles results in essentially the same cv -term for column packings prepared using just different slurry concentrations. Further, significant changes in the transchannel eddy dispersion contribution ($\omega_1 v$) are also unlikely due to the identical PSD and a relatively small variation in the bulk porosity (cf. Section 2.3.2.1 and Table 2.1). Comparable packing densities result in a similar shape and size of the interparticle flow channels, which engenders similar transchannel eddy dispersion. Consequently, the different slopes of the $H-u_{av}$ plots at velocities beyond the plate height minimum in Fig. 2.2B

must be connected to differences in packing microstructure affecting the entire column cross-section, as reflected by the transcolum eddy dispersion contribution ($\omega_3 v$). That is, different qualities of column wall effects (resulting from the widely different slurry concentrations used for column packing) move into the focus of our study to explain the varying efficiencies documented in Fig. 2.2 via $\omega_3 v$ in Eq. (2.2).

2.3.2 Bed reconstruction and morphological analysis

General properties of the three CLSM-based reconstructions are summarized in Table 2.1. CLSM-based PSDs from reconstructed sections are compared with the PSD obtained by SEM analysis in Fig. 2.3. All four data sets show a highly similar PSD, mean particle diameter and Sauter mean diameter, as well as a relative standard deviation of the PSD of $\sim 15\%$, which has been observed before with similar particles [13]. It forms a consistent picture regarding the width and shape of the underlying PSD in terms of these different analysis methods (SEM, CLSM) and is considered a prerequisite to subsequent, meaningful analysis.

Table 2.1. Properties of the reconstructions and particle size distributions.

Slurry concentration, c_{slurry}	20 mg/mL	140 mg/mL	200 mg/mL	SEM
No. of particles	11409	9846	11708	1244
Mean diameter d_p [μm]	1.93	1.93	1.94	1.91
Sauter diameter d_s [μm]	2.01	2.02	2.03	2.02
$\varepsilon_{\text{bulk}}$ [-]	0.444	0.453	0.458	–

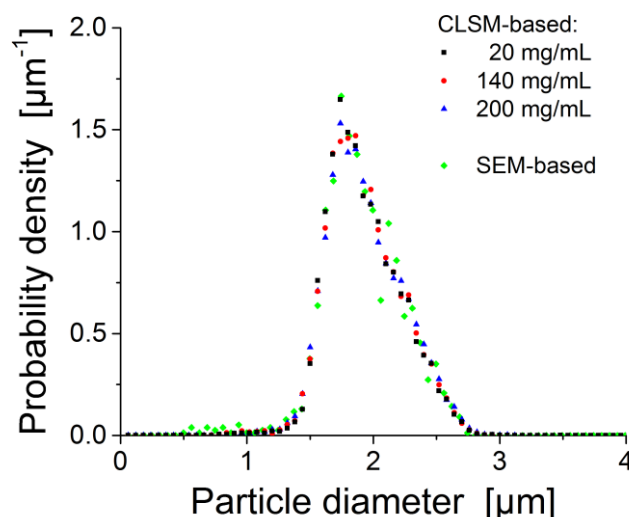


Fig. 2.3. Particle size distribution (PSD) analysis for the 1.9 μm BEH silica particles. CLSM-based PSDs for the reconstructed packings in comparison with the SEM-based PSD derived after particle extrusion from the column packed at a slurry concentration of 5 mg/mL.

2.3.2.1 Packing density, porosity distribution, radial heterogeneity

The radial porosity profiles $\varepsilon(r)$, shown in Fig. 2.4, display the local interstitial void volume fraction as a function of the radial position, with $r = 0$ at the column wall. The bulk porosity values for the three reconstructions ($\varepsilon_{\text{bulk}}$) range from 0.444 to 0.458 (cf. Table 2.1), i.e., they slightly increase with slurry concentration but are generally very close. On the other hand, all these bulk porosities are well above the random-close packing limit of $\varepsilon_{\text{bulk}} \sim 0.35$ estimated from computer simulations for frictionless hard spheres with a similar relative standard deviation of the PSD of $\sim 15\%$ [53]. These values are close to the random-loose packing limit for frictional hard spheres at ~ 0.45 [54–59]. Still, the values found here for the $1.9 \mu\text{m}$ BEH silica particles remain below the $\varepsilon_{\text{bulk}}$ -values of 0.47–0.50 observed in our previous study with $1.3 \mu\text{m}$ BEH silica particles [2]. In that study, we addressed the importance of frictional and cohesive forces between small particles to obtain dense and stable packings. Similarly, the $1.9 \mu\text{m}$ BEH silica particles in the present work have no perfectly smooth surface and cohesion is important for particles smaller than $10 \mu\text{m}$ [60–64]. It can lead to formation of loose but stable beds with relatively high interparticle porosities. A further important aspect is the number of larger voids that can accommodate particles from a given PSD (for a discussion of larger voids, see Section 2.3.2.2). If a void size of $\geq 1.38 \mu\text{m}$ ($= 1\%$ of the PSD) is considered, then 2% of the bed porosity can be accounted for by such voids for the 200 mg/mL column, while only 0.9% of the bed porosity can be explained for the 20 mg/mL column.

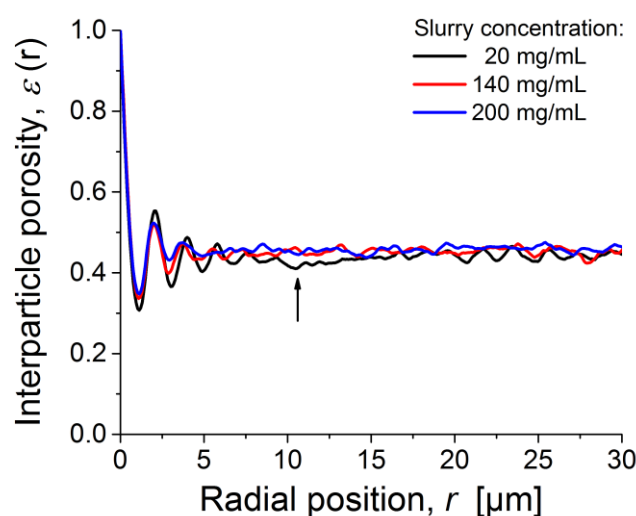


Fig. 2.4. Radial distribution of interparticle porosity $\varepsilon(r)$ for the three reconstructed columns packed at different slurry concentration. For the 20 mg/mL column, the arrow indicates a locally densified (denser-than-average) packing region between the more ordered particle layers near the column wall and the bulk packing region.

Oscillations in porosity profiles (Fig. 2.4) close to the column wall cover the first 3–6 layers of more regularly arranged (ordered) particles, starting with the first layer in touch with the column wall, represented by the minimum in $\varepsilon(r)$ at $r \approx 0.5 d_p$. With increasing distance from the wall oscillations relax into a random porosity distribution characteristic of bulk packing.

Interestingly, at increasing slurry concentration both amplitude and duration of the oscillations decrease resulting in a reduced effect on the associated flow heterogeneity [33]. Further, a closer look at the $\varepsilon(r)$ -profile for the 20 mg/mL column reveals a local dip at a distance of $\sim 10 \mu\text{m}$ from the wall reflecting locally increased packing density (highlighted by the arrow in Fig. 2.4). To quantify deviations from the nearly constant porosity in the bulk packing region ($\varepsilon_{\text{bulk}}$), relative porosity profiles $\varepsilon_{\text{rel}}(r)$ are calculated, $\varepsilon_{\text{rel}}(r) = \varepsilon(r) - \varepsilon_{\text{bulk}}$ (Fig. 2.5). This function can be divided into two regions for the 140 and 200 mg/mL columns. The vertical solid lines in Fig. 2.5 highlight these regions: the wall-affected region with porosity oscillations and the bulk packing region. For the 20 mg/mL column, a third region appears between oscillations and bulk (cf. arrow in Fig. 2.4). It is characterized by a lower-than-average porosity representing a higher-than-average density. To quantify these effects by a scalar measure, we determined the integral porosity deviation (IPD) as follows [11,12]:

$$\text{IPD} = \int_{r_1}^{r_2} (\varepsilon(r) - \varepsilon_{\text{bulk}}) dr \quad (2.3)$$

For global IPD values, the integration in Eq. (2.3) is done from the column wall ($r_1 = 0$) to the column centre, with the column radius r_c as upper limit ($r_2 = r_c$). To obtain a more detailed view on local porosity fluctuations, several integration limits were applied (based on the spatial extension of characteristic regions in the porosity profiles). These limits are visualized with the vertical lines in Fig. 2.5, and the resulting local IPD values between limits are given. All three columns show a similar contribution (~ 0.16 – 0.17) to the global IPD due to the significantly higher-than-average porosity in the region representing the gap between the first layer of particles and the hard column wall (first region). These high porosities lead to increased local velocities, in general, but there is a stagnant layer with zero velocity directly at the wall (no-slip boundary condition), which reduces this effect of increased porosity next to the wall. This interplay (and resulting picture) is illustrated, e.g., in Figs. 7 and 8 in [33]. Since IPD values for this region are very close in all three columns, it suggests also a similar effect on band broadening.

The second region spans from the first zero transition of $\varepsilon_{\text{rel}}(r) = \varepsilon(r) - \varepsilon_{\text{bulk}}$ to the end of the wall region, where bulk behaviour and $\varepsilon_{\text{bulk}}$ is reached (marking the onset of the third region). Here, all three columns show lower porosity than in the bulk region, i.e., negative IPD values, which (in contrast to the first region) results in locally decreased velocities with respect to the bulk packing. The peculiarity of this denser region depends on slurry concentration and reveals a clear trend. With increasing slurry concentration from 20 to 200 mg/mL (bottom to top in Fig. 2.5), the radial extension of the second region decreases from $\sim 16 \mu\text{m}$ (bottom) to $\sim 6 \mu\text{m}$ (top), the IPD value changes from -0.21 to ca. -0.05 , and the amplitude of porosity oscillations due to the more ordered particle layers near the wall decreases. Both regions identified in Fig. 2.5 determine the transcolum flow heterogeneity and eddy dispersion represented by the linear ω_3 -term in Eq. (2.2). While the first region is similar for all columns, i.e., independent of slurry concentration, we expect differences in column efficiency to be dominated by the different second wall region and resulting differences in the ω_3 -term.

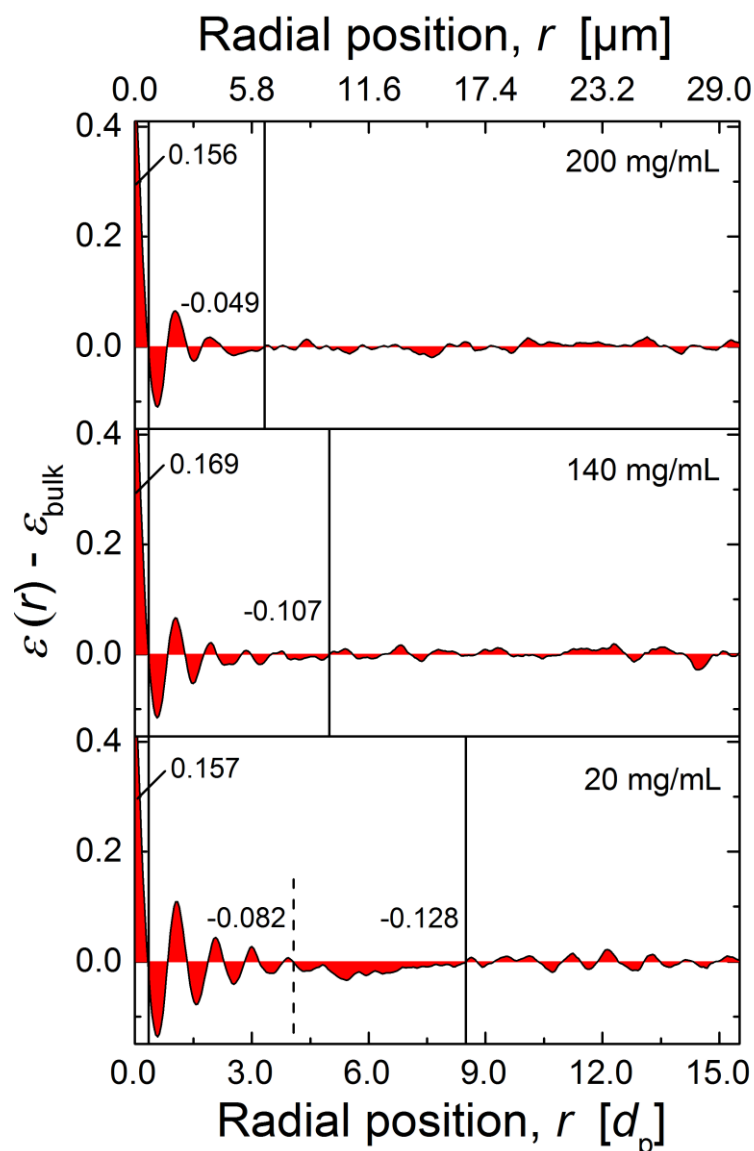


Fig. 2.5. Radial distribution of the relative porosity $\varepsilon(r) - \varepsilon_{\text{bulk}}$ ($r = 0$ at the column wall). Calculated integral porosity deviation (IPD) values (cf. Eq. (2.3)) for different regions are provided as numbers, vertical lines visualize associated integration limits. Regions from left to right: gap between hard column wall and first layer of particles; particle layers near the wall with decreasing order towards centre of the column; transition region in the 20 mg/mL column with higher-than-average packing density; bulk region). The values of $\varepsilon_{\text{bulk}}$ are given in Table 2.1.

Since both deviations from bulk porosity in the wall region and the radial extension of this region decrease with increasing slurry concentration, the column efficiency loss due to transcolumn eddy dispersion contribution will also be reduced. Based exclusively on this argument and data in Fig. 2.5, the 200 mg/mL column should show the highest and the 20 mg/mL column the lowest separation efficiency. But this is not the case, as Fig. 2.2 has proven. Indeed, the 140 mg/mL column is the best performing one and the other two columns are comparable in their (reduced) performance.

Interestingly, for the column packed at 20 mg/mL slurry concentration (bottom panel in Fig. 2.5) the wall region is significantly extended beyond the more ordered particle layers, before bulk porosity is attained, i.e., before the porosity profile becomes flat. This phenomenon is absent for the other two columns packed at much higher slurry concentration. A further division of the densely packed second region in the 20 mg/mL column is between the ordered and random particle layers and indicated by the dashed line in Fig. 2.5. Both (sub)regions are more densely packed than the bulk of the bed with negative IPD values of -0.082 and -0.128. However, while the region close to the wall exhibits porosity oscillations indicative of more ordered particle layers, the region further from the wall does not reveal any oscillatory behaviour, which suggests random (in addition to denser than average) packing.

This phenomenon observed here in the wall region of the 20 mg/mL column is similar to the two wall effects seen in analytical columns; it just occurs on the smaller capillary scale. Shalliker et al. [14] identified a geometrical wall effect in the form of the more ordered particle layers directly at the column wall (also seen in Fig. 2.5 for all three columns) and a second wall effect, which is known as important contribution to band broadening in analytical columns [16–18]. The second wall effect (in the case of analytical columns) is described as a densified region with a radial extension of $\sim 50 d_p$ and is caused by radial stress exerting forces on the particles against the wall and friction between bed and wall during the packing process. Not unexpectedly, this effect is smaller in a capillary than in an analytical column. But the characteristics of the wall effect in the 20 mg/mL column revealed by Fig. 2.5 are qualitatively similar to the wall effects in analytical columns, highlighting similarities in the dynamic processes occurring during bed formation.

Another important aspect regarding the generation of transcolumn heterogeneities, which we have noticed in previous studies [12,13], is the systematic discrimination of particles according to their size during the column packing procedure. Therefore, we analysed mean particle size in a locally resolved manner (Fig. 2.6). 140 and 200 mg/mL columns have a mostly flat profile, while the 20 mg column shows strong size-segregation, an effect we observed previously in combination with dilute slurries [12,13]. In this particular case, up to 5% larger-than-average particles are found in direct vicinity of the column wall, up to $r \approx 5 \mu\text{m}$. Further beyond, a region with up to 4% smaller-than-average particle diameters is located (until $r \approx 15 \mu\text{m}$). It coincides with the region of lower-than-average porosity in the radial porosity profile (Fig. 2.5). In addition to the effects associated with deviations from bulk porosity, the size segregation will locally alter the transchannel and the short-range interchannel contribution to eddy dispersion, because the size of individual channels between particles depends on particle diameter. However, the associated transcolumn heterogeneity in flow and transport is the most severe consequence of these effects, since it affects the longest time and largest length scales, with the entire column diameter as reference.

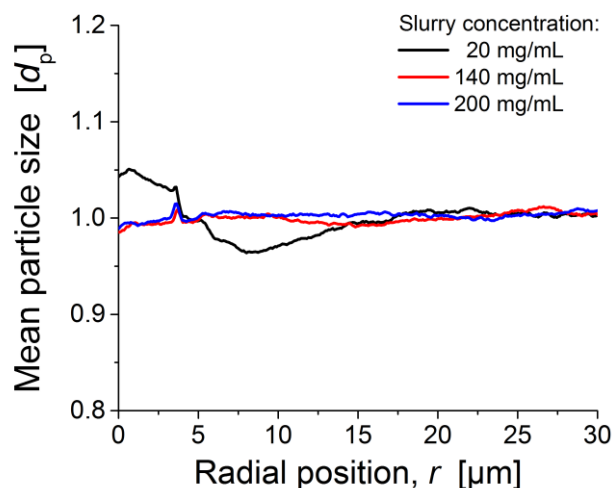


Fig. 2.6. Radial distribution of mean particle diameter for the three reconstructed columns packed at different slurry concentrations.

The transcolum heterogeneities in porosity (Fig. 2.5) and particle size (Fig. 2.6) are a straightforward explanation for the observed efficiency difference between 20 and 140 mg/mL columns (Fig. 2.2). On the other hand, these heterogeneities cannot explain the difference between 140 and 200 mg/mL columns, since both appear mostly homogenous radially and the wall effect is even further reduced from 140 to 200 mg/mL (Fig. 2.5). Thus, additional morphological features have to be identified to explain this adverse effect on column efficiency that accompanies a too-high slurry concentration. Larger voids, with a size comparable to the average particle size, are a known structural feature in columns packed at high slurry concentration [2,13]. Thus, they are a potential candidate to explain the poorer performance of the 200 mg/mL column. We quantify number and size of voids in the three reconstructions in the subsequent section. A comparison of the results from the present work regarding porosity profiles and size-segregation effects with our previous works [2,11–13,48] follows in the Conclusions, after we have analysed the distribution of larger voids in the packings and investigated the bed formation process (Section 2.3.2.3).

2.3.2.2 Analysis of larger voids

During our last studies [2,13], we identified larger voids that can accommodate particles of the size of the mean diameter as limiting separation efficiency of columns packed with high slurry concentrations. Both number and size of these voids increased with slurry concentration. Consequently, we performed a void analysis similar to our previous study on slurry concentration effects with 1.3 μm BEH silica particles [2]. The identified voids are distinguished into voids that can accommodate spheres with a size from 10–50% of the PSD (1.56–1.85 μm), 50–90% (1.86–2.27 μm), or $\geq 90\%$ (≥ 2.28 μm). The statistical analysis of the results is presented in Table 2.2 and Fig. 2.7, which also displays the size thresholds by vertical lines. The number of voids that can accommodate particles with a size of at least 10% of the PSD (i.e., a particle size ≥ 1.56 μm) increases by a factor of ~ 4 when the slurry concentration is

increased from 20 to 200 mg/mL. In addition, the size of the voids increases. For example, the formation of very large voids, which could contain particles with a size of at least 90% of the PSD (i.e., a particle size $\geq 2.28 \mu\text{m}$), occurs only for the 200 mg/mL column. To visualize differences between the packings, a two-dimensional projection of the voids along the y -direction is presented in Fig. 2.8. In addition to the previously stated observations, this view reveals an inhomogeneous distribution of voids for the 20 mg/mL column: There are almost no larger voids in the locally densified packing region between the ordered particle layers and the bulk packing region (cf. Section 2.3.2.3).

Table 2.2. Analysis of larger voids in the three reconstructions.

	Void size	20 mg/mL	140 mg/mL	200 mg/mL
Voids per reconstruction	$\geq 1.56 \mu\text{m}$	88	199	332
	$\geq 1.86 \mu\text{m}$	2	3	39
	$\geq 2.28 \mu\text{m}$	0	0	5
Voids per 1000 particles	$\geq 1.56 \mu\text{m}$	7.71	20.21	28.36
	$\geq 1.86 \mu\text{m}$	0.18	0.30	3.33
	$\geq 2.28 \mu\text{m}$	–	–	0.43

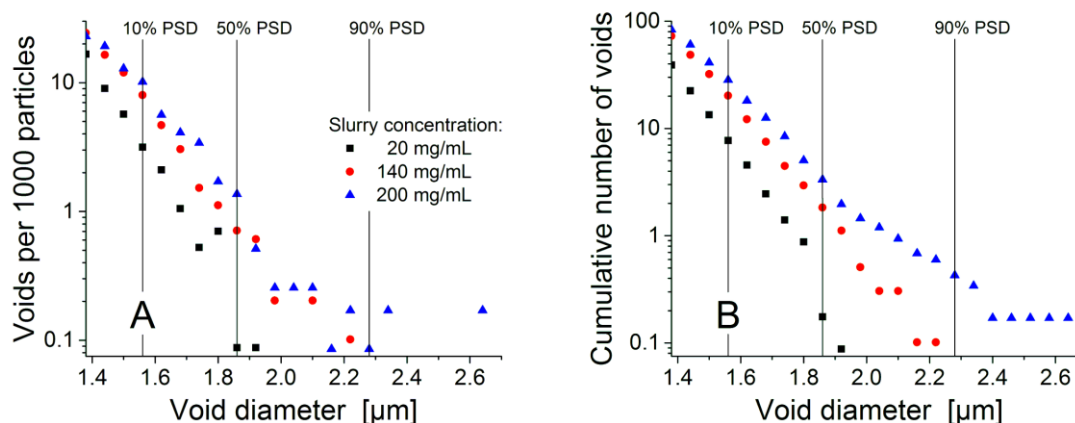


Fig. 2.7. Number of voids in the reconstructed column beds per 1000 particles. (A) Absolute and (B) cumulative number of voids depending on their diameter.

The presence of larger voids, in general, can contribute to band broadening in several ways. A void increases the width of the interstitial flow channel and, thus, leads to a locally higher flow velocity [35]. This can be connected to a modulation of transchannel eddy dispersion in the individual flow channels (ω_1 -term in Eq. (2.2)) and also to a modification of the short-range interchannel contribution between neighbouring flow channels due to the increased velocity extremes (ω_2 -term in Eq. (2.2)). In addition, the actual distribution of the voids plays an important role. If the voids are not distributed homogeneously over the column cross-section, as for the 20 mg/mL column, they engender another transcolumn contribution to band broadening (ω_3 -term in Eq. (2.2)). Voids could also be distributed inhomogeneously in the bulk region

resulting in separated void-free and void-rich regions. Then a long-range interchannel contribution would result. Simulations by Schure and Maier underscore losses in efficiency due to voids [36]. To summarize, the radially inhomogeneous distribution of the (few) voids in the 20 mg/mL column is yet another aspect explaining its poorer performance compared to the 140 mg/mL column, while the substantial increase in the number and size of voids can explain the (again poor) performance of the 200 mg/mL column. The best column efficiency is realized at a slurry concentration that optimally balances radial heterogeneities against void formation, which in the current work is represented by the 140 mg/mL column.

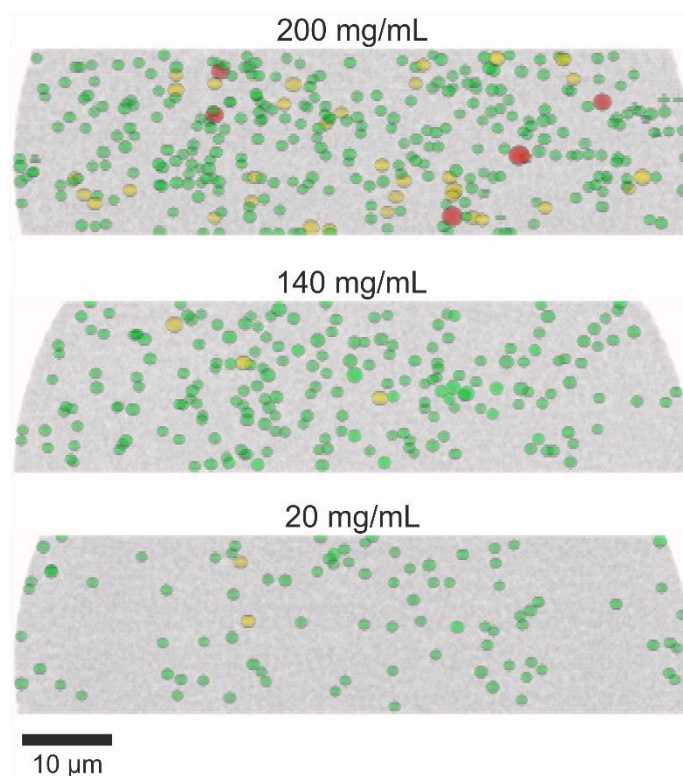


Fig. 2.8. *xz*-views of the reconstructed column beds highlighting larger voids. Green: Voids that can accommodate spheres with a size from 10–50% of the SEM-based PSD (1.56–1.85 μm), yellow: voids that can accommodate spheres with a size from 50–90% of the SEM-based PSD (1.86–2.27 μm), and red: voids that can accommodate spheres with a size of $\geq 90\%$ of the SEM-based PSD (≥ 2.28 μm).

The same general trends have been observed in our recent study with 1.3 μm BEH silica particles [2], where best column efficiency was reached at a different slurry concentration (~ 20 mg/mL), but radial heterogeneities and the presence of voids were similarly identified as morphological origin(s) behind different column efficiencies in dependence of slurry concentration. In that study, we came up with suggestions on how the larger voids at high slurry concentration could be generated and stabilized, and how their number in a packing could be minimized. This discussion is continued here with the subsequent section, which focuses on the bed formation process.

2.3.2.3 Investigation of bed formation

In our recent study with 1.3 μm BEH silica particles [2] we already discussed particle aggregation during column packing as a potentially useful tool to achieve bed structures generating high column efficiency. Blue and Jorgenson [65] analysed particle aggregation in different slurry solvents using in-solution microscopy and found that the most efficient column also showed the strongest particle aggregation in the slurry. Conclusions based on the free-slurry behaviour need to be considered with care, as slurry flow and the actual pressure distribution can substantially modify conditions during the packing process. Therefore, we acquired videos of the capillary column packing for two slurry concentrations (10 and 100 mg/mL) to monitor bed formation and extract useful, complementary information. Example images from these videos are presented in Fig. 2.9 and the videos are supplied as supplementary material.

As the videos and selected snapshots in Fig. 2.9 illustrate, bed formation proceeds in a very different way for these two samples (slurry concentrations). At the lower slurry concentration of 10 mg/mL (videos 1–3), the particles arrive individually as a continuous stream in the centre of the column, forming a cone-like structure, and settle along the flanks of the cone. The shape of the cone appears to be conserved and the cone just grows while the additional particles arrive. At the higher slurry concentration (100 mg/mL, videos 4 and 5), the bed formation is less continuous and much faster. This is expected, because the slurry flow rate is comparable but more particles arrive in the same time-frame. This makes it more difficult to observe bed formation, although some conclusions can be drawn. First, the particles do not arrive individually any longer, but come in huge patches, which represent large aggregates. Second, the bed front is not shaped as regular cone (seen for 10 mg/mL) but changes substantially, sometimes showing the bed front closer to the column centre, sometimes closer to the wall. These observations imply the presence of substantial particle aggregation during column packing already at 100 mg/mL slurry concentration, i.e., below the optimal concentration. Thus, aggregation can also be assumed at higher slurry concentrations including the optimum for column packing.

The observations from the videos allow conclusions regarding the origin of the structural features we identified and discussed in Sections 2.3.2.1 and 2.3.2.2. At low slurry concentration particles arrive individually and have enough time to settle, an important factor for the final bed density and bed structure [21,22]. Furthermore, later particles impact onto already settled particles and may move them out of their position, which induces resettling. This can also be an aspect behind the observed size-segregation (Fig. 2.6) and local densification (Fig. 2.5), since it gives a chance for discrimination of individual particles during the settling process. At high slurry concentration, the particles arrive in large patches and the bed formation occurs quickly. This strongly reduces the settling time for an individual particle. Especially at the border between these large patches defects can be formed and conserved.

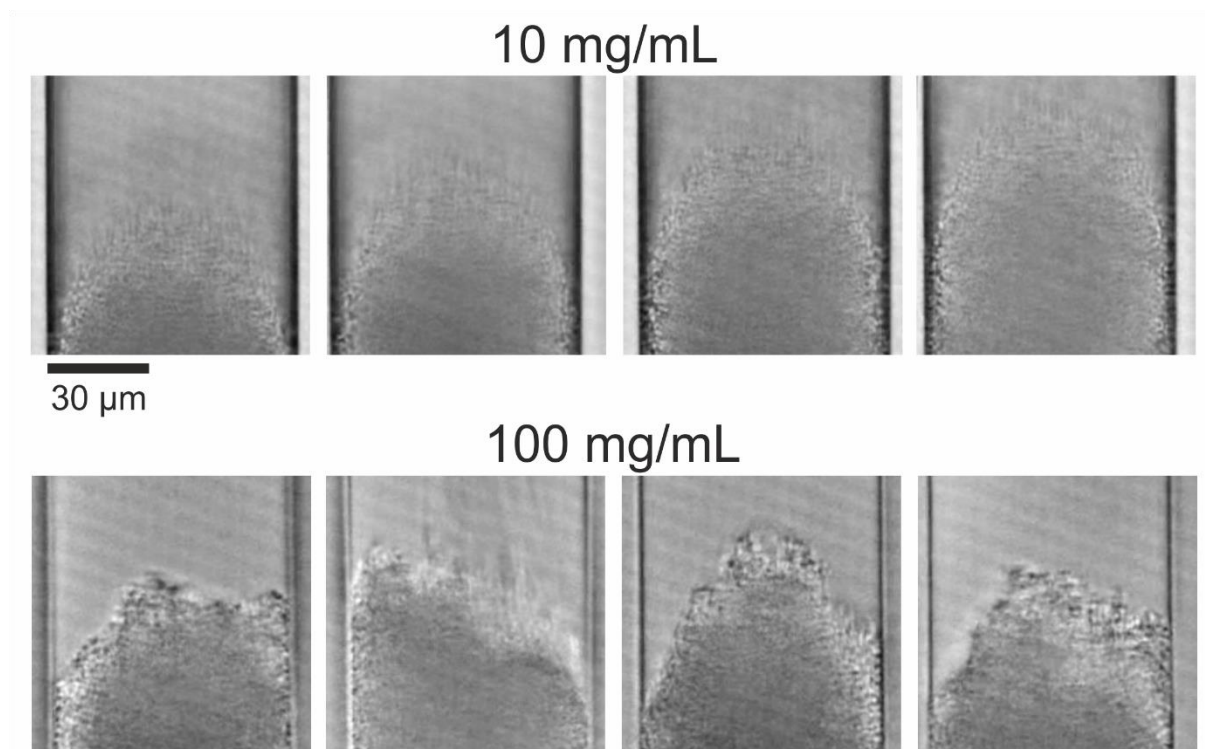


Fig. 2.9. Exemplary frames from the videos taken during the formation of the column beds for slurry concentrations of 10 and 100 mg/mL. At the lower slurry concentration (top row), the bed is formed by a stream of individually arriving particles resulting in a cone-like shape of the bed front. At the higher slurry concentration (bottom row), particles arrive in large patches causing fluctuations in the shape of the actual bed front.

2.4 Conclusions

We identified an optimal slurry concentration for reproducible packing of highly efficient capillary columns. We found a substantially different optimal slurry concentration compared to our recent work with 1.3 μm BEH particles [2], but very similar trends in the resulting morphological properties of the columns and their relative importance as a function of the slurry concentration. This demonstrates the complexity of the packing process, but also the similarity of relevant morphological features. Morphological properties analysed in CLSM-based reconstructions and video-based observations of bed formation were used to understand packing process-related structural characteristics of columns and explain their separation efficiencies.

For the applied packing protocol (1.9 μm BEH silica particles, acetone slurry, 75 μm i.d. columns, and a bed length of ~ 45 cm), the optimal slurry concentration to reproducibly pack highly efficient columns ranges from 140 to 160 mg/mL, while optimal slurry concentration was 20 mg/mL for 1.3 μm BEH silica particles with a 75 μm column i.d. and ~ 30 cm bed length. This may be explainable with the smaller particle size (1.3 vs. 1.9 μm), which enhances the importance of cohesive forces between particles and the tendency of particle aggregation, thus

relegating optimal conditions for the best column packing to lower slurry concentrations to avoid the excessive generation of larger voids in the final packing.

CLSM-based 3D reconstructions were prepared and analysed with respect to their morphological features to find explanation for the observed differences in column efficiency as a function of the slurry concentration. Our observations reveal counteracting effects, similar to phenomena that we have identified in previous studies [2,11–13,48] regarding the morphology of packed columns: radial packing heterogeneities dominant at low slurry concentration and formation of larger voids in the bed dominant at high slurry concentration. Three radial effects in the packing microstructure are elucidated in the column packed at 20 mg/mL. These microstructures are already suppressed with a 140 mg/mL slurry: (i) a denser region between more ordered particle layers near the column wall and the bulk packing region, similar to the second wall effect in analytical columns (Fig. 2.5), (ii) a particle-size segregation effect (Fig. 2.6), and (iii) an inhomogeneous distribution of larger voids over the column cross-section (Fig. 2.8).

Size-segregation has been seen before with 1.9 μm BEH silica particles, but only in the enrichment of smaller-than-average particles in vicinity of the column wall [12,13]. The denser packing region observed for the 20 mg/mL column in Fig. 2.5 with a locally negative IPD-value of -0.128 is not only similar to the more extended, densified wall-packing region in analytical columns [14,17,18], but was also observed in capillary columns packed with different types of core-shell particles (Kinetex, Halo, Poroshell) [11,48]. The current study confirms, e.g., by Fig. 2.5, that the general effect of wall packing deviations from the bulk packing behaviour (uniformly random) decreases with increasing slurry concentration. This remains true even beyond the point when size-segregation and a densified transition region are already suppressed (140 \rightarrow 200 mg/mL, Figs. 2.4–2.6).

The existence of larger voids (with a size similar to the mean particle diameter) in the bed was also observed for fully porous and core-shell particles before [2,13,48]. An increase in both number and size of formed voids at increasing slurry concentration was already seen for the 1.3 μm BEH silica particles [2]. Based on these findings, we proposed particle aggregation in the slurry as a key factor behind the formation of larger voids. To obtain insight into the column bed formation, videos were acquired for slurry concentrations of 10 and 100 mg/mL, revealing substantial and not unexpected differences in bed formation. At low slurry concentration, the bed is formed by individually settling particles, allowing for particle rearrangements (which will be necessary to observe size-segregation in the final bed), whereas the large patches of particles smashing onto the top of the bed in the case of high slurry concentration indicate a substantial particle aggregation in the slurry (which depends on slurry concentration, the particle size and resulting interparticle forces, among other aspects like the slurry solvent).

Results of this study, and our previous work, suggest an approach to reproducibly reach even higher separation efficiencies. Reduction of wall effects continues with further increase of the slurry concentration even beyond the optimal slurry concentration (Fig. 2.5). The increasing presence of larger voids then starts to limit column efficiency. Thus, if the formation of these voids (number and size) could be prevented, the application of even higher slurry concentrations (higher than the optimal 140 mg/mL seen in this work) could pave the way for much higher

separation efficiencies. As discussed in our recent study [2], the application of ultrasound during packing bears potential in reducing significant void formation and improving long-term column stability [20,66–69]. In fact, our preliminary efforts in column packing using these insights allowed the combination of very high slurry concentration and ultrasound during column packing to prepare extremely efficient one-meter long capillary columns. These columns boast with a plate count of ~500,000 over one meter of packed bed and a reduced plate height near unity [38]. Following this avenue can lead us to the realization of great improvements in one-dimensional separations of very complex samples.

Acknowledgement

The authors would like to thank Waters Corporation (Milford, MA), the National Institutes of Health (Grant #5U24DK097153), and the National Institute of Diabetes and Digestive and Kidney Diseases (NIDDK) (Grant #1R01DK101473) for support of the work reported in this manuscript

Appendix A. Supplementary data

Supplementary data associated with this article can be found, in the online version, at <http://dx.doi.org/10.1016/j.chroma>.

References

- [1] J.W. Jorgenson, Capillary liquid chromatography at ultrahigh pressures, *Annu. Rev. Anal. Chem.* 3 (2010) 129–150.
- [2] A.E. Reising, J.M. Godinho, K. Hormann, J.W. Jorgenson, U. Tallarek, Larger voids in mechanically stable, loose packings of 1.3 μm frictional, cohesive particles: Their reconstruction, statistical analysis, and impact on separation efficiency, *J. Chromatogr. A* 1436 (2016) 118–132.
- [3] J.J. DeStefano, S.A. Schuster, J.M. Lawhorn, J.J. Kirkland, Performance characteristics of new superficially porous particles, *J. Chromatogr. A* 1258 (2012) 76–83.
- [4] F. Gritti, G. Guiochon, Accurate measurements of the true column efficiency and of the instrument band broadening contributions in the presence of a chromatographic column, *J. Chromatogr. A* 1327 (2014) 49–56.
- [5] F. Gritti, T. Farkas, J. Heng, G. Guiochon, On the relationship between band broadening and the particle-size distribution of the packing material in liquid chromatography: Theory and practice, *J. Chromatogr. A* 1218 (2011) 8209–8221.
- [6] S. Fanali, G. D’Orazio, T. Farkas, B. Chankvetadze, Comparative performance of capillary columns made with totally porous and core-shell particles coated with a polysaccharide-based chiral selector in nano-liquid chromatography and capillary electrochromatography, *J. Chromatogr. A* 1269 (2012) 136–142.
- [7] A. de Villiers, H. Lauer, R. Szucs, S. Goodall, P. Sandra, Influence of frictional heating on temperature gradients in ultra-high-pressure liquid chromatography on 2.1 mm I.D. columns, *J. Chromatogr. A* 1113 (2006) 84–91.

-
- [8] J.J. DeStefano, B.E. Boyes, S.A. Schuster, W.L. Miles, J.J. Kirkland, Are sub-2 μm particles best for separating small molecules? An alternative, *J. Chromatogr. A* 1368 (2014) 163–172.
- [9] F. Gritti, M. Martin, G. Guiochon, Influence of viscous friction heating on the efficiency of columns operated under very high pressures, *Anal. Chem.* 81 (2009) 3365–3384.
- [10] F. Gritti, M. Martin, G. Guiochon, Influence of pressure on the properties of chromatographic columns: II. The column hold-up volume, *J. Chromatogr. A* 1070 (2005) 13–22.
- [11] S. Bruns, D. Stoeckel, B.M. Smarsly, U. Tallarek, Influence of particle properties on the wall region in packed capillaries, *J. Chromatogr. A* 1268 (2012) 53–63.
- [12] S. Bruns, J.P. Grinias, L.E. Blue, J.W. Jorgenson, U. Tallarek, Morphology and separation efficiency of low-aspect-ratio capillary ultrahigh pressure liquid chromatography columns, *Anal. Chem.* 84 (2012) 4496–4503.
- [13] S. Bruns, E.G. Franklin, J.P. Grinias, J.M. Godinho, J.W. Jorgenson, U. Tallarek, Slurry concentration effects on the bed morphology and separation efficiency of capillaries packed with sub-2 μm particles, *J. Chromatogr. A* 1318 (2013) 189–197.
- [14] R.A. Shalliker, B.S. Broyles, G. Guiochon, Physical evidence of two wall effects in liquid chromatography, *J. Chromatogr. A* 888 (2000) 1–12.
- [15] F. Gritti, G. Guiochon, Theoretical and experimental impact of the bed aspect ratio on the axial dispersion coefficient of columns packed with 2.5 μm particles, *J. Chromatogr. A* 1262 (2012) 107–121.
- [16] F. Gritti, G. Guiochon, Perspectives on the evolution of the column efficiency in liquid chromatography, *Anal. Chem.* 85 (2013) 3017–3035.
- [17] F. Gritti, G. Guiochon, Relationship between trans-column eddy diffusion and retention in liquid chromatography: Theory and experimental evidence, *J. Chromatogr. A* 1217 (2010) 6350–6365.
- [18] J.A. Abia, K.S. Mriziq, G.A. Guiochon, Radial heterogeneity of some analytical columns used in high-performance liquid chromatography, *J. Chromatogr. A* 1216 (2009) 3185–3191.
- [19] J.J. Kirkland, J.J. DeStefano, The art and science of forming packed analytical high-performance liquid chromatography columns, *J. Chromatogr. A* 1126 (2006) 50–57.
- [20] J.P.C. Vissers, H.A. Claessens, J. Laven, C.A. Cramers, Colloid chemical aspects of slurry packing techniques in microcolumn liquid chromatography, *Anal. Chem.* 67 (1995) 2103–2109.
- [21] J.P.C. Vissers, M.A. Hoeben, J. Laven, H.A. Claessens, C.A. Cramers, Hydrodynamic aspects of slurry packing processes in microcolumn liquid chromatography, *J. Chromatogr. A* 883 (2000) 11–25.
- [22] M.F. Wahab, C.A. Pohl, C.A. Lucy, Colloidal aspects and packing behaviour of charged microparticulates in high efficiency ion chromatography, *J. Chromatogr. A* 1270 (2012) 139–146.
- [23] F. Capriotti, I. Leonardis, A. Cappiello, G. Famiglini, P. Palma, A fast and effective method for packing nano-lc columns with solid-core nano particles based on the synergic
-

- effect of temperature, slurry composition, sonication and pressure, *Chromatographia* 76 (2013) 1079–1086.
- [24] S. Fanali, S. Rocchi, B. Chankvetadze, Use of novel phenyl-hexyl core-shell particles in nano-LC, *Electrophoresis* 34 (2013) 1737–1742.
- [25] S. Jung, A. Hölzel, S. Ehlert, J.A. Mora, K. Kraiczek, M. Dittmann, et al., Impact of conduit geometry on the performance of typical particulate microchip packings, *Anal. Chem.* 81 (2009) 10193–10200.
- [26] S. Khirevich, A. Hölzel, S. Ehlert, A. Seidel-Morgenstern, U. Tallarek, Large-scale simulation of flow and transport in reconstructed HPLC-microchip packings, *Anal. Chem.* 81 (2009) 4937–4945.
- [27] G. Van Tendeloo, S. Bals, S. Van Aert, J. Verbeeck, D. Van Dyck, Advanced electron microscopy for advanced materials, *Adv. Mater.* 24 (2012) 5655–5675.
- [28] G. Sundaramoorthi, M. Hadwiger, M. Ben-Romdhane, A.R. Behzad, P. Madhavan, S.P. Nunes, 3D membrane imaging and porosity visualization, *Ind. Eng. Chem. Res.* 55 (2016) 3689–3695.
- [29] P. Levitz, Toolbox for 3D imaging and modeling of porous media: Relationship with transport properties, *Cem. Concr. Res.* 37 (2007) 351–359.
- [30] O. Ersen, I. Florea, C. Hirlimann, C. Pham-Huu, Exploring nanomaterials with 3D electron microscopy, *Mater. Today* 18 (2015) 395–408.
- [31] T. Müllner, K.K. Unger, U. Tallarek, Characterization of microscopic disorder in reconstructed porous materials and assessment of mass transport-relevant structural descriptors, *New J. Chem.* (2016) 3993–4015.
- [32] S. Khirevich, A. Hölzel, D. Hlushkou, U. Tallarek, Impact of conduit geometry and bed porosity on flow and dispersion in noncylindrical sphere packings, *Anal. Chem.* 79 (2007) 9340–9349.
- [33] S. Khirevich, A. Hölzel, A. Seidel-Morgenstern, U. Tallarek, Geometrical and topological measures for hydrodynamic dispersion in confined sphere packings at low column-to-particle diameter ratios, *J. Chromatogr. A* 1262 (2012) 77–91.
- [34] A. Daneyko, S. Khirevich, A. Hölzel, A. Seidel-Morgenstern, U. Tallarek, From random sphere packings to regular pillar arrays: Effect of the macroscopic confinement on hydrodynamic dispersion, *J. Chromatogr. A* 1218 (2011) 8231–8248.
- [35] A. Daneyko, D. Hlushkou, V. Baranau, S. Khirevich, A. Seidel-Morgenstern, U. Tallarek, Computational investigation of longitudinal diffusion, eddy dispersion, and trans-particle mass transfer in bulk, random packings of core-shell particles with varied shell thickness and shell diffusion coefficient, *J. Chromatogr. A* 1407 (2015) 139–156.
- [36] M.R. Schure, R.S. Maier, How does column packing microstructure affect column efficiency in liquid chromatography? *J. Chromatogr. A* 1126 (2006) 58–69.
- [37] H. Liasneuski, D. Hlushkou, S. Khirevich, A. Hölzel, U. Tallarek, S. Torquato, Impact of microstructure on the effective diffusivity in random packings of hard spheres, *J. Appl. Phys.* 116 (2014) 034904.
- [38] J.M. Godinho, A.E. Reising, U. Tallarek, J.W. Jorgenson, Implementation of high slurry concentration and sonication to pack high-efficiency, meter-long capillary ultrahigh

- pressure liquid chromatography columns, *J. Chromatogr. A* 1462 (2016) 165–169.
- [39] K.D. Patel, A.D. Jerkovich, J.C. Link, J.W. Jorgenson, In-depth characterization of slurry packed capillary columns with 1.0- μm nonporous particles using reversed-phase isocratic ultrahigh-pressure liquid chromatography, *Anal. Chem.* 76 (2004) 5777–5786.
- [40] J.E. MacNair, K.C. Lewis, J.W. Jorgenson, Ultrahigh-pressure reversed-phase liquid chromatography in packed capillary columns, *Anal. Chem.* 69 (1997) 983–989.
- [41] J.E. MacNair, K.D. Patel, J.W. Jorgenson, Ultrahigh-pressure reversed-phase capillary liquid chromatography: Isocratic and gradient elution using columns packed with 1.0- μm particles, *Anal. Chem.* 71 (1999) 700–708.
- [42] J.S. Mellors, J.W. Jorgenson, Use of 1.5 micron porous ethyl-bridged hybrid particles as a stationary phase support for reversed-phase ultra-high pressure liquid chromatography, *Anal. Chem.* 76 (2004) 5441–5450.
- [43] U.D. Neue, *HPLC Columns: Theory, Technology, and Practice*, Wiley-VCH, New York, 1997.
- [44] A. Maiolica, D. Borsotti, J. Rappsilber, Self-made frits for nanoscale columns in proteomics, *Proteomics* 5 (2005) 3847–3850.
- [45] L.A. Knecht, E.J. Guthrie, J.W. Jorgenson, On-column electrochemical detector with a single graphite fiber electrode for open-tubular liquid chromatography, *Anal. Chem.* 56 (1984) 479–482.
- [46] S. Hsieh, J.W. Jorgenson, Preparation and evaluation of slurry-packed liquid chromatography microcolumns with inner diameters from 12 to 33 microns, *Anal. Chem.* 68 (1996) 1212–1217.
- [47] S. Bruns, T. Müllner, M. Kollmann, J. Schachtner, A. Höltzel, U. Tallarek, Confocal laser scanning microscopy method for quantitative characterization of silica monolith morphology, *Anal. Chem.* 82 (2010) 6569–6575.
- [48] S. Bruns, U. Tallarek, Physical reconstruction of packed beds and their morphological analysis: Core-shell packings as an example, *J. Chromatogr. A* 1218 (2011) 1849–1860.
- [49] W.S. Rasband, ImageJ, U. S. National Institutes of Health, Bethesda, MD, <http://imagej.nih.gov/ij/>, 1997–2016.
- [50] E. Hamdan, J.F. Milthorpe, J.C.S. Lai, An extended macroscopic model for solute dispersion in confined porous media, *Chem. Eng. J.* 137 (2008) 614–635.
- [51] J.C. Giddings, *Dynamics of chromatography, Part 1: Principles and Theory*, Marcel Dekker, New York, 1965.
- [52] S. Khirevich, A. Höltzel, A. Seidel-Morgenstern, U. Tallarek, Time and length scales of eddy dispersion in chromatographic beds, *Anal. Chem.* 81 (2009) 7057–7066.
- [53] V. Baranau, U. Tallarek, Random-close packing limits for monodisperse and polydisperse hard spheres, *Soft Matter* 10 (2014) 3826–3841.
- [54] G.Y. Onoda, E.G. Liniger, Random loose packings of uniform spheres and the dilatancy onset, *Phys. Rev. Lett.* 64 (1990) 2727–2730.
- [55] Z.P. Zhang, L.F. Liu, Y.D. Yuan, A.B. Yu, A simulation study of the effects of dynamic variables on the packing of spheres, *Powder Technol.* 116 (2001) 23–32.
- [56] C. Song, P. Wang, H.A. Makse, A phase diagram for jammed matter, *Nature* 453 (2008)

- 629–632.
- [57] M. Jerkins, M. Schröter, H.L. Swinney, T.J. Senden, M. Saadatfar, T. Aste, Onset of mechanical stability in random packings of frictional spheres, *Phys. Rev. Lett.* 101 (2008) 018301.
- [58] G.R. Farrell, K.M. Martini, N. Menon, Loose packings of frictional spheres, *Soft Matter* 6 (2010) 2925–2930.
- [59] L.E. Silbert, Jamming of frictional spheres and random loose packing, *Soft Matter* 6 (2010) 2918–2924.
- [60] R.Y. Yang, R.P. Zou, A.B. Yu, Computer simulation of the packing of fine particles, *Phys. Rev. E* 62 (2000) 3900–3908.
- [61] A.B. Yu, C.L. Feng, R.P. Zou, R.Y. Yang, On the relationship between porosity and interparticle forces, *Powder Technol.* 130 (2003) 70–76.
- [62] K.J. Dong, R.Y. Yang, R.P. Zou, A.B. Yu, Role of interparticle forces in the formation of random loose packing, *Phys. Rev. Lett.* 96 (2006) 145505.
- [63] J.M. Valverde, A. Castellanos, Random loose packing of cohesive granular materials, *Europhys. Lett.* 75 (2007) 985–991.
- [64] W. Liu, S. Li, A. Baule, H.A. Makse, Adhesive loose packings of small dry particles, *Soft Matter* (2015) 6492–6498.
- [65] L.E. Blue, J.W. Jorgenson, 1.1 μm superficially porous particles for liquid chromatography. Part II: Column packing and chromatographic performance, *J. Chromatogr. A* 1380 (2015) 71–80.
- [66] M. Franc, J. Sobotníková, P. Coufal, Z. Bosáková, Comparison of different types of outlet frits in slurry-packed capillary columns, *J. Sep. Sci.* 37 (2014) 2278–2283.
- [67] R.A. Shalliker, B.S. Broyles, G. Guiochon, Evaluation of the secondary consolidation of columns for liquid chromatography by ultrasonic irradiation, *J. Chromatogr. A* 878 (2000) 153–163.
- [68] S. Ehlert, T. Rösler, U. Tallarek, Packing density of slurry-packed capillaries at low aspect ratios, *J. Sep. Sci.* 31 (2008) 1719–1728.
- [69] S. Ehlert, K. Kraiczek, J.A. Mora, M. Dittmann, G.P. Rozing, U. Tallarek, Separation efficiency of particle-packed HPLC microchips, *Anal. Chem.* 80 (2008) 5945–5950.

Chapter 3

Implementation of High Slurry Concentration and Sonication to Pack High-Efficiency, Meter-Long Capillary Ultrahigh Pressure Liquid Chromatography Columns

Authors

Justin M. Godinho, Arved E. Reising, Ulrich Tallarek, and James W. Jorgenson

State of publication

Published 1 August 2016 in *Journal of Chromatography A*, Vol. 1462, pp. 165–169.

Abstract

Slurry packing capillary columns for ultrahigh pressure liquid chromatography is complicated by many interdependent experimental variables. Previous results have suggested that combination of high slurry concentration and sonication during packing would create homogeneous bed microstructures and yield highly efficient capillary columns. Herein, the effect of sonication while packing very high slurry concentrations is presented. A series of six, 1 meter x 75 μm internal diameter columns were packed with 200 mg/mL slurries of 2.02 μm bridged-ethyl hybrid silica particles. Three of the columns underwent sonication during packing and yielded highly efficient separations with reduced plate heights as low as 1.05.

3.1 Introduction

The benefits of sub-2 μm chromatographic supports have largely focused separation technologies towards ultrahigh pressure liquid chromatography (UHPLC) [1]. Theoretically, sorbents on this scale provide higher separation efficiencies and shorter separation times. True benefit from these materials is dependent, however, on homogeneous packing of the sorbent into a column. This is complicated by the smaller particle's requirement of significantly increased packing pressure and presents a major challenge in the creation of a uniform bed structure. As packing material continues in the direction of smaller particles, dispersion due to transcolumn heterogeneity becomes significantly more important. This type of dispersion is estimated to account for up to 70% of the total dispersion for small molecules in UHPLC columns [2].

Packing that results in a well performing column requires the formation of a homogeneous bed structure across all scales, from transchannel to transcolumn, within the column [3]. Study of

“optimal” packing conditions has led to more detailed understanding of the physical process [4–14]. Unfortunately this process is dynamic and highly influenced by many interdependent parameters. The results of these studies have yielded many opinions on the “art” of column packing as opposed to the science. More recently, collaboration between our groups has examined certain packing parameters including the effects of particle properties, capillary column diameter and slurry concentration [15–17]. Most importantly these studies have been informed by three-dimensional reconstructions via confocal laser scanning microscopy (CLSM) of the packing microstructure. These renderings have allowed for detailed expositions of morphological features corresponding to specific packing conditions, which are then related to explain the column’s kinetic performance.

Morphological heterogeneity between a column’s wall region and bulk packing is often the main contributor to poor column performance [18–23]. Previous studies have indicated that the differences in these regions are dependent on slurry concentration [16, 17]. Detailed understanding of the packing microstructure has guided empirical packing studies to obtain well performing columns. For example, our initial results suggest that there is a specific “intermediate” slurry concentration capable of balancing the antagonizing effects associated with a low or high slurry concentration for each particle diameter [16]. Further study of this proposition confirmed balancing of packing defects and demonstrated that increasing slurry concentration suppresses wall effects and reduces transcolumn bed heterogeneities through prevention of both locally high porosity and particle size segregation [17].

We further noticed that even though slurry concentrations higher than “optimal” continue to suppress wall effects, the columns perform poorly [17]. The benefits of high slurry concentrations eventually begin to diminish as the number and size of packing voids in the bed structure increases. Giddings suggested voids would impact eddy dispersion negatively and contribute significantly to chromatographic band broadening [3]. Voids increase velocity extremes and eddy dispersion on both transchannel and short-range interchannel scales. The detriment of incorporated voids was also illustrated with dispersion simulations that resulted in stating the column’s overall performance is more dependent on reduction of large voids than obtaining high packing densities [24].

The conclusions to our most recent study propose that even higher efficiency UHPLC columns may result from formation of a homogenous bed structure across the entire column through the combination of high slurry concentration and sonication to prevent the formation of larger voids [17]. To date sonication has been used in column packing, but only to limited effect and not in association with very high slurry concentrations [25–29]. Reduction of the total number of voids should allow for realization of more homogeneous and highly efficient columns.

To test this a set of 6 capillary columns, all 1 meter in length x 75 μm internal diameter (i.d.), were packed with 200 mg/mL slurries. Three of the columns were packed with the application of sonication and three were not. Columns packed with sonication yielded performance with reduced plate heights approaching 1 and a realized (instead of extrapolated as often reported) 470,000 plates/meter.

3.2 Materials and Methods

3.2.1 Chemicals and materials

75 μm i.d. cylindrical fused-silica tubing was purchased from Polymicro Technologies (Phoenix, AZ). The capillaries were packed with C18-modified bridged-ethyl hybrid (BEH) silica particles provided by Waters Corporation (Milford, MA) with a Sauter diameter of 2.02 μm . The Sauter diameter was calculated from a scanning electron microscope (SEM) based particle size distribution obtained from the measurement of ~ 1200 C18-modified 1.9 μm BEH particles from the same batch using a JSM-7500F SEM (Joel, München, Germany). HPLC grade acetonitrile, acetone (reagent grade), trifluoroacetic acid (TFA), and the test analytes for chromatographic characterization (L-ascorbic acid, hydroquinone, resorcinol, catechol, 4-methyl catechol) were obtained from Fisher Scientific (St. Louis, MO). Kasil frits for the packed capillaries were prepared with potassium silicate from PQ Corporation (Valley Forge, PA) and formamide from Sigma–Aldrich (St. Louis, MO). HPLC grade water for chromatographic experiments was obtained from a Millipore NANOpure water system (Billerica, MA).

3.2.2 Preparation of capillary UHPLC columns

Preparation of the capillary UHPLC columns has been described previously in detail [8–14]. Modifications to the procedure will be highlighted here. Column blanks (160 cm x 75 μm i.d.) were fritted using the Kasil method [30]. The extra 60 cm was needed to over pack slightly to allow for bed compression (~ 10 cm) as well as to reach from the packing vessel to the sonication bath (~ 50 cm). In order to prepare outlet frits, the ends of capillaries were depressed onto a glass microfiber filter (Reeve Angel, Clifton, NJ) wetted with 50/50 (v/v) potassium silicate/formamide. The column blanks were then dried overnight at 50° C and the resulting frits were ~ 125 μm in length. Slurries were prepared by mixing a known mass of the particles in a known volume of acetone (to achieve 200 mg/mL) and suspended with a 10 min sonication cycle using a Cole Parmer Ultrasonic Cleaner 8891 (Vernon Hills, IL).

Prior to packing, the inlet to the column blank was fixed within a UHPLC fitting. The outlet was threaded through the top of a piece of shipping foam padding that was cut to fit snugly within the sonication bath's included basket. The portion of capillary blank to be packed (in this case ~ 108 cm) was pulled through the top of the foam entirely. This portion of the column blank was then coiled and taped to the bottom of the foam padding to keep it in place. To ensure the created outlet frit did not lose integrity due to sonication, it was threaded back through the shipping foam padding (from the bottom side, in which the majority of the capillary was taped) until the frit and 2 cm of outlet end of the column blank protruded from the top of the foam padding. This arrangement corresponded to the outlet of column blank being 2 cm above the water line in the sonication bath. The slurry was then placed into a packing reservoir and the inlet of the column blank was secured to the reservoir using the already affixed UHPLC fitting. The foam supporting the coiled capillary was placed into the sonication bath, ensuring that the desired final length (already coiled and secured to the bottom of the foam) remained submerged under water and that the 2 cm of the blanks outlet, including the installed frit, remained above

the water line. Sonication during packing was conducted with an Elmasonic P 60 H (Elma Schmidbauer GmbH, Singen, Germany) sonication bath. The sonication bath was set to sweep mode at 80 kHz. Packing was initiated using acetone as a pushing solvent at 150 bar from a DSHF-300 Haskel pump (Burbank, CA). The packing pressure was immediately increased to 2070 bar when the 2 visible cm of bed had been packed. The maximum packing pressure was chosen to maintain consistency between these experiments and previously reported packing studies [15–17]. The column was allowed to pack until the formed bed was visible outside the packing foam, which meant the 108 cm of bed had been packed. The temperature of the bath was kept at 30° C by adding a small amount of ice as necessary and measured using the sonication bath's temperature readout on the display. After the desired length was reached, the packing pressure was slowly released to atmospheric pressure. The column was then connected to a DSXHF-903 Haskel pump (Burbank, CA) using an UHPLC injection apparatus. Each column was flushed for 1 h in 50/50 (v/v) water/acetonitrile with 0.1% TFA at 3500 bar, after which the pressure was gradually released and reinitiated at 700 bar to form a temporary inlet frit with a heated wire stripper from Teledyne Interconnect Devices (San Diego, CA). Columns were then clipped to a 100 cm bed length and an inlet frit was installed using the Kasil method.

3.2.3. Chromatographic analysis

Column efficiency was tested under isocratic elution conditions using a 200 μM test mixture (L-ascorbic acid, dead-time marker; hydroquinone, resorcinol, catechol, and 4-methyl catechol) and an UHPLC injection apparatus [9]. The mobile phase used for evaluation was 50/50 (v/v) water/acetonitrile with 0.1% TFA. Analytes were detected amperometrically. Electrochemical detection was conducted at a 8 $\mu\text{m} \times 300 \mu\text{m}$ carbon fibre microelectrode held at +1.1 V vs. Ag/AgCl reference electrode [31]. This electrode was placed at the outlet of the UHPLC column. Current-to-voltage conversion was conducted using an SR750 current amplifier (Stanford Research Systems, Sunnyvale, CA) with a 109 V/A gain and a 3 Hz, 3 dB low-pass bandwidth filter. An Intel Core 2 Duo desktop computer with a 16-bit A/D converter was used to acquire data at 21 Hz. Data were collected with a custom-written LabView 6.0 program (National Instruments, Austin, TX).

Columns were analysed over a range of mobile phase velocities to create plots of the plate height H vs. the average mobile phase velocity u_{av} for each analyte in the test mixture. Reduced plate height curves ($h = H/d_p$ vs. $v = u_{av}d_p/D_m$) were calculated using the particles' Sauter diameter ($d_p = 2.02 \mu\text{m}$) and D_m , the pressure-dependent diffusion coefficient of an analyte in the bulk mobile phase [32]. High frequency noise was removed from the chromatograms using a digital frequency filter and low frequency baseline drift was eliminated by background subtraction. Retention times and theoretical plate counts N were determined using an iterative statistical moments ($\pm 3\sigma$) algorithm written in Igor Pro 6.0 (Wavemetrics, Inc., Lake Oswego, OR) [11].

3. Results and Discussion

Studied here are six capillaries packed at a very high slurry concentration. Previous studies of 100 mg/mL slurries yielded relatively well performing capillary columns with minimum reduced plate height (h_{\min}) values near 1.5 [10,16]. For this experiment a concentration of 200 mg/mL was chosen to ensure excess to an intermediate slurry concentration, enhanced suppression of radial defects and a high number of large packing voids, wherein the cumulative effects of these voids would be expected to yield relatively poor chromatographic efficiency. Three of the capillaries within this study underwent sonication and three did not. For the sake of consistency, all six were placed in the same orientation within the sonication bath during packing, whether sonication was applied or not.

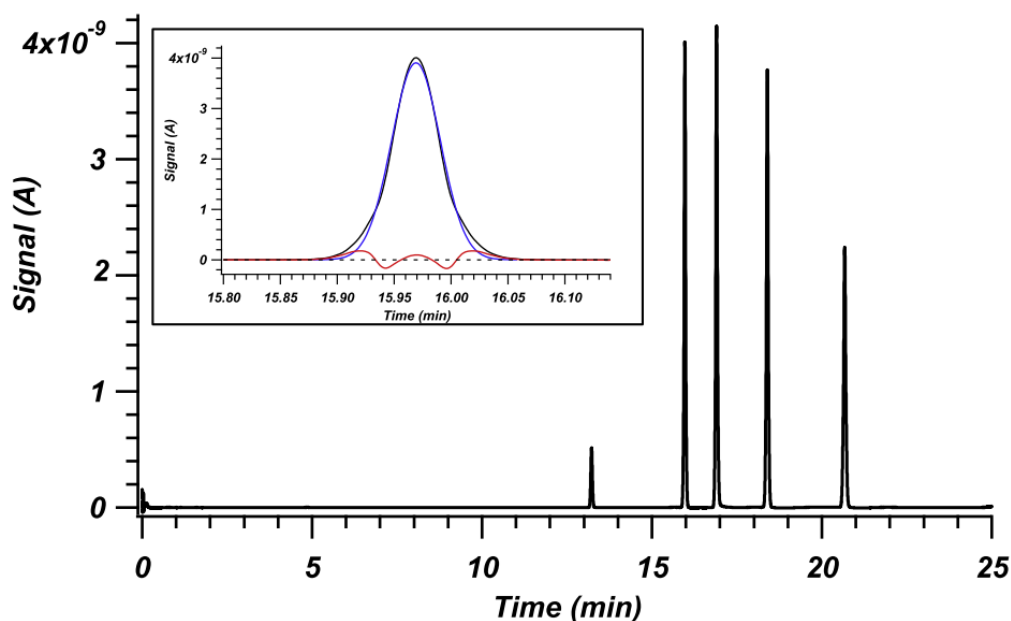


Fig. 3.1. Example chromatogram for one of the three columns packed with sonication and run at 1630 bar. This column is represented by red triangles in Figs. 2 and 3. Peaks from left to right are L-ascorbic acid, hydroquinone, resorcinol, catechol and 4-methyl catechol. The inset presents an enlargement of the hydroquinone peak used for the reduced plate height curves in Fig. 2. The experimental data is plotted in black, the Gaussian fit in blue and the residuals are plotted in red. A black dashed line is overlaid at 0 signal for reference.

Plotted in Figure 3.1 is an example chromatogram showing the performance of one of the three columns packed with sonication. Inset in Figure 3.1 is an enlargement of the hydroquinone peak, overlaid with a Gaussian fit and residuals. Iterative statistical moments ($\pm 3\sigma$) were used for plate counts of all reported data. These plate counts are more conservative than those calculated by full width at half height and Gaussian fit methods. For example the inset hydroquinone peak would have plate counts of 558,000 using full width at half height and 556,000 using a Gaussian fit. Reduced plate height h for these plate determination methods would be 0.88. Figure 3.2 plots the reduced van Deemter fits ($h = a + b/v + cv$) for hydroquinone for each of the six columns. Most notably the six columns fall into two distinct groups, those

that underwent the application of sonication and those that did not. The consistency of the columns that underwent sonication is very high. Overall efficiency of these columns approaches a reduced plate height of 1.05. Columns that were not exposed to sonication did not exhibit similarly high reproducibility in reduced parameters and showed poorer performance with h_{\min} between 1.8 and 2.2.

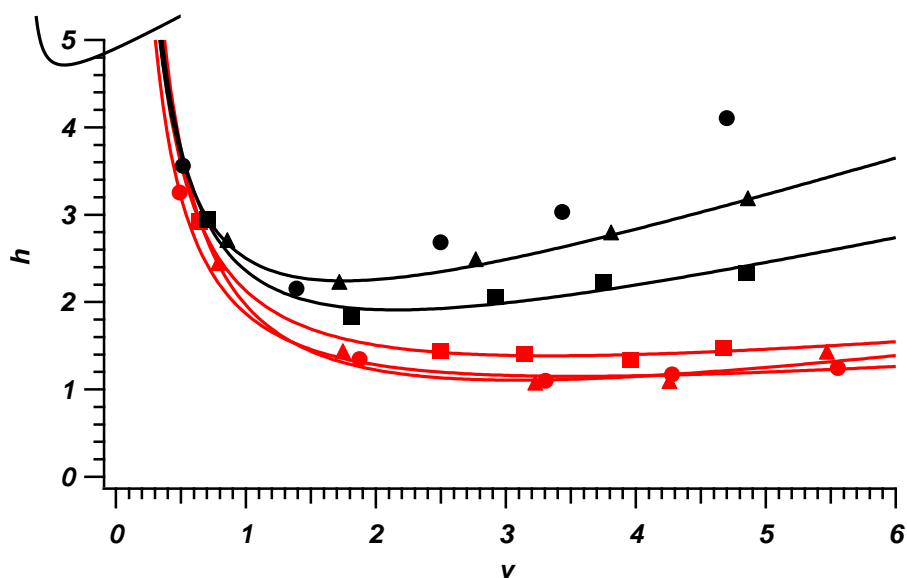


Fig. 3.2. Plot of reduced van Deemter fits for hydroquinone on each of the 6, 1-m long columns. Columns packed with sonication are presented in red while columns prepared without sonication are plotted in black. Marker shapes (circles, squares and triangles) distinguish each column within the parameters represented by colour.

Figure 3.3 plots u_{av} vs. pressure normalized for column length. The data naturally falls into two groups separated by column packing procedure. Higher average velocities for ascorbic acid are apparent for those columns prepared with sonication. Regarding the known effects of high slurry concentrations and their tendency to incorporate very wide void size distributions [17], we can interpret these results as similar to a packing prepared with a highly polydisperse particle size distribution (one significantly broader and more skewed than that of the packed BEH material: the utilized BEH material exhibits approximately 15% relative standard deviation for the particle size distribution). Based on Figure 3.2 we know that the columns packed with sonication have a more homogeneous bed structure due to the improved efficiency. This translates into substantially narrowed distribution of sizes for local interstitial void fractions with respect to the columns that did not undergo sonication. This homogenization of the bed microstructure leads to higher observed velocity and permeability for the dead time marker through the column. Simulations yielded similar results in which a reduced width and tail in the interstitial void volume distribution improved hydraulic permeability [33]. Packing columns with very high slurry concentration and sonication boosts separation efficiency while improving mobile phase permeability. That is, a narrower width and more uniform distribution of interparticle void volumes produces more uniform and less tortuous flow paths. Whereas an ultrasound-induced homogenization of the packing microstructure over the column cross-

section can explain both, higher separation efficiency and permeability, the permeability might additionally benefit from a slightly lower packing density.

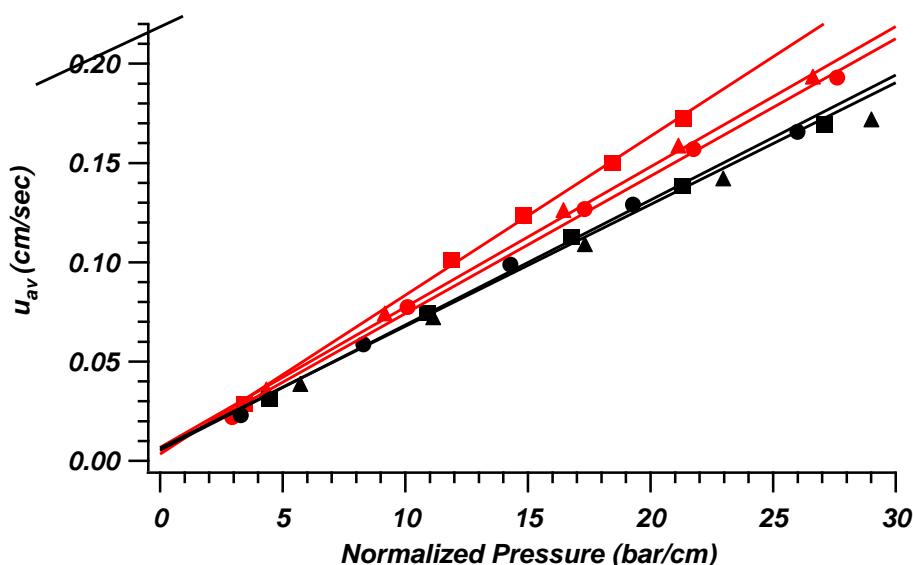


Fig. 3.3. Plot of the linear velocity of the dead time marker, L-ascorbic acid, against pressure drop normalized for column length. Columns packed with sonication are presented in red while columns prepared without sonication are plotted in black. Marker shapes (circles, squares and triangles) distinguish each column within the parameters represented by color.

The performance of columns undergoing sonication far exceeds reports of other highly efficient capillary columns [10]. However, these results are not unexpected. First, the experimental setup has been optimized to limit extra-column band broadening as injection, detection and unpacked bed (frits) produce negligible extra-column band broadening. Second, it is known that reduced plate heights can approach values below 1.5 for very low aspect ratio capillaries (column-to-particle diameter ratios $d_c/d_p < 20$) [9,15]. In this case d_c/d_p is 37.1, nearly twice that value. No theoretical basis exists for this limitation on minimum plate height. Transcolumn exchange of an analyte molecule on the 75 μm dimension of the capillary diameter is fast and any exchange between different regions of local flow velocity is quickly terminated by transverse dispersion [34]. Third, from past CLSM studies we know that the integral porosity deviation approaches zero as slurry concentration increases (indicative of wall region in a bed that attains average packing density as the bulk region of that bed) [17]. The very high slurry concentrations utilized here should further suppress localized heterogeneities. Finally, simulations of plate height in computer-generated packing have yielded reduced plate heights below unity [22].

4. Conclusions

The results presented here highlight the beneficial effects of two packing variables: very high slurry concentration and sonication. The remarkable performance of these columns, which far exceeds previous separation efficiencies seen in our lab and elsewhere for fully porous particles packed into capillary columns, leads us to believe that we have successfully mitigated the

incorporation of packing voids while suppressing radial heterogeneity previously identified at a capillary column's wall. Packed capillary columns with performance approaching reduced plate heights of 1 offer new frontiers into the use of UHPLC columns. When packed to a meter long and producing 500,000 theoretical plates, the opportunity for fast separations at high pressure with very high peak capacities could greatly improve one-dimensional separations of very complex samples. The fundamental study of slurry packing as a function of slurry concentration has given insight into the packing process and guided studies to greatly improve slurry packing of capillary columns.

Acknowledgements

The authors would like to thank Waters Corporation (Milford, MA), the National Institute of Health (Grant #5U24DK097153) and the National Institute of Diabetes and Digestive and Kidney Diseases (NIDDK) (Grant #1R01DK101473-01A1) for support of the work reported in this manuscript.

References

- [1] J.W. Jorgenson, Capillary liquid chromatography at ultrahigh pressures, *Annu. Rev. Anal. Chem.* 3 (2010) 129–150.
- [2] F. Gritti, G. Guiochon, Perspectives on the evolution of the column efficiency in liquid chromatography, *Anal. Chem.* 85 (2013) 3017–3035.
- [3] J.C. Giddings, *Dynamics of Chromatography, Part I: Principles and Theory*. Marcel Dekker, New York, N.Y., 1965.
- [4] J.P.C. Vissers, H.A. Claessens, J. Laven, C.A. Cramers, Colloid chemical aspects of slurry packing techniques in microcolumn liquid chromatography, *Anal. Chem.* 67 (1995) 2103–2109.
- [5] J.P.C. Vissers, M.A. Hoeben, J. Laven, H.A. Claessens, C.A. Cramers, Hydrodynamic aspects of slurry packing processes in microcolumn liquid chromatography, *J. Chromatogr. A* 883 (2000) 11–25.
- [6] P.D.A. Angus, C.W. Demarest, T. Catalano, J.F. Stobaugh, Aspects of column fabrication for packed capillary electrochromatography, *J. Chromatogr. A* 887 (2000) 347–365.
- [7] J.J. Kirkland, J.J. DeStefano, The art and science of forming packed analytical high-performance liquid chromatography columns, *J. Chromatogr. A* 1126 (2006) 50–57.
- [8] L.E. Blue, J.W. Jorgenson, 1.1 μm superficially porous particles for liquid chromatography. Part II: Column packing and chromatographic performance, *J. Chromatogr. A* 1380 (2015) 71–80.
- [9] J.W. Treadway, K.D. Wyndham, J.W. Jorgenson, Highly efficient capillary columns packed with superficially porous particles via sequential column packing, *J. Chromatogr. A* 1422 (2015) 345–349.
- [10] E.G. Franklin, Utilization of Long Columns Packed with Sub-2 μm Particles Operated at High Pressures and Elevated Temperatures for High-Efficiency One-Dimensional Liquid Chromatographic Separations. Ph.D. Dissertation, The University of North Carolina at Chapel Hill, 2012.
- [11] S. Hsieh, J.W. Jorgenson, Preparation and evaluation of slurry-packed liquid chromatography microcolumns with inner diameters from 12 to 33 μm , *Anal. Chem.* 68 (1996) 1212–1217.
- [12] J.S. Mellors, J.W. Jorgenson, Use of 1.5- μm porous ethyl-bridged hybrid particles as a stationary-phase support for reversed-phase ultrahigh-pressure liquid chromatography, *Anal. Chem.* 76 (2004) 5441–5450.
- [13] K.D. Patel, A.D. Jerkovich, J.C. Link, J.W. Jorgenson, In-depth characterization of slurry packed capillary columns with 1.0- μm nonporous particles using reversed-phase isocratic ultrahigh-pressure liquid chromatography, *Anal. Chem.* 76 (2004) 5777–5786.
- [14] R.T. Kennedy, J.W. Jorgenson, Preparation and evaluation of packed capillary liquid chromatography columns with inner diameters from 20 to 50 micrometers, *Anal. Chem.* 61 (1989) 1128–1135.

-
- [15] S. Bruns, J.P. Grinias, L.E. Blue, J.W. Jorgenson, U. Tallarek, Morphology and separation efficiency of low-aspect-ratio capillary ultrahigh pressure liquid chromatography columns, *Anal. Chem.* 84 (2012) 4496–4503.
- [16] S. Bruns, E.G. Franklin, J.P. Grinias, J.M. Godinho, J.W. Jorgenson, U. Tallarek, Slurry concentration effects on the bed morphology and separation efficiency of capillaries packed with sub-2 μm particles, *J. Chromatogr. A* 1318 (2013) 189–197.
- [17] A.E. Reising, J.M. Godinho, K. Hormann, J.W. Jorgenson, U. Tallarek, Larger voids in mechanically stable, loose packings of 1.3 μm frictional, cohesive particles: Their reconstruction, statistical analysis, and impact on separation efficiency, *J. Chromatogr. A* 1436 (2016) 118–132.
- [18] F. Gritti, M. Martin, G. Guiochon, Influence of viscous friction heating on the efficiency of columns operated under very high pressures, *Anal. Chem.* 81 (2009) 3365–3384.
- [19] G. Guiochon, T. Farkas, H. Guan-Sajonz, J.-H. Koh, M. Sarker, B.J. Stanley, et al., Consolidation of particle beds and packing of chromatographic columns, *J. Chromatogr. A* 762 (1997) 83–88.
- [20] R.A. Shalliker, B.S. Broyles, G. Guiochon, Physical evidence of two wall effects in liquid chromatography, *J. Chromatogr. A* 888 (2000) 1–12.
- [21] S. Khirevich, A. Hölzel, D. Hlushkou, U. Tallarek, Impact of conduit geometry and bed porosity on flow and dispersion in noncylindrical sphere packings, *Anal. Chem.* 79 (2007) 9340–9349.
- [22] S. Khirevich, A. Hölzel, A. Seidel-Morgenstern, U. Tallarek, Geometrical and topological measures for hydrodynamic dispersion in confined sphere packings at low column-to-particle diameter ratios, *J. Chromatogr. A* 1262 (2012) 77–91.
- [23] A. Daneyko, S. Khirevich, A. Hölzel, A. Seidel-Morgenstern, U. Tallarek, From random sphere packings to regular pillar arrays: Effect of the macroscopic confinement on hydrodynamic dispersion, *J. Chromatogr. A* 1218 (2011) 8231–8248.
- [24] M.R. Schure, R.S. Maier, How does column packing microstructure affect column efficiency in liquid chromatography? *J. Chromatogr. A* 1126 (2006) 58–69.
- [25] S. Roulin, R. Dmoch, R. Carney, K.D. Bartle, P. Myers, M.R. Euerby, C. Johnson, Comparison of different packing methods for capillary electrochromatography columns, *J. Chromatogr. A* 887 (2000) 307–312.
- [26] P. Koivisto, R. Danielsson, K.E. Markides, Factors affecting the preparation of packed capillary columns in supercritical carbon dioxide media, *J. Microcolumn Sep.* 9 (1997) 97–103.
- [27] F. Capriotti, I. Leonardis, A. Cappiello, G. Famiglini, P. Palma, A fast and effective method for packing nano-LC columns with solid-core nano particles based on the synergic effect of temperature, slurry composition, sonication and pressure, *Chromatographia* 76 (2013) 1079–1086.
- [28] S. Ehlert, K. Kraiczek, J.A. Mora, M. Dittmann, G.P. Rozing, U. Tallarek, Separation efficiency of particle-packed HPLC microchips, *Anal. Chem.* 80 (2008) 5945–5950.
-

-
- [29] M.J. Wirth, S. Ranasinghe Kodithuwakkuge, C. Yerneni, R. Birdsall, Method of packing chromatographic columns. WO2011127044 A2, Oct. 13, 2011.
- [30] A. Maiolica, D. Borsotti, J. Rappsilber, Self-made frits for nanoscale columns in proteomics, *Proteomics* 5 (2005) 3847–3850.
- [31] L.A. Knecht, E.J. Guthrie, J.W. Jorgenson, On-column electrochemical detector with a single graphite fiber electrode for open-tubular liquid chromatography, *Anal. Chem.* 56 (1984) 479–482.
- [32] T.J. Kaiser, J.W. Thompson, J.S. Mellors, J.W. Jorgenson, Capillary-based instrument for the simultaneous measurement of solution viscosity and solute diffusion coefficient at pressures up to 2000 bar and implications for ultrahigh pressure liquid chromatography, *Anal. Chem.* 81 (2009) 2860–2868.
- [33] D. Vidal, C. Ridgway, G. Pianet, J. Schoelkopf, R. Roy, F. Bertrand, Effect of particle size distribution and packing compression on fluid permeability as predicted by lattice-Boltzmann simulations, *Comput. Chem. Eng.* 33 (2009) 256–266.
- [34] A. Daneyko, D. Hlushkou, S. Khirevich, U. Tallarek, From random sphere packings to regular pillar arrays: Analysis of transverse dispersion, *J. Chromatogr. A* 1257 (2012) 98–115.

Chapter 4

Analysis of packing microstructure and wall effects in a narrow-bore ultrahigh pressure liquid chromatography column using focused ion-beam scanning electron microscopy

Authors

Arved E. Reising, Sabine Schlabach, Vasili Baranau, Daniela Stoeckel, and Ulrich Tallarek

State of publication

Published 14 July 2017 in *Journal of Chromatography A*, Vol. 1513, pp. 172–182.

Abstract

Column wall effects are well recognized as major limiting factor in achieving high separation efficiency in HPLC. This is especially important for modern analytical columns packed with small particles, where wall effects dominate the band broadening. Detailed knowledge about the packing microstructure of packed analytical columns has so far not been acquired. Here, we present the first three-dimensional reconstruction protocol for these columns utilizing focused ion-beam scanning electron microscopy (FIB-SEM) on a commercial 2.1 mm inner diameter \times 50 mm length narrow-bore analytical column packed with 1.7 μm bridged-ethyl hybrid silica particles. Two sections from the packed bed are chosen for reconstruction by FIB-SEM: one from the bulk packing region of the column and one from its critical wall region. This allows quantification of structural differences between the wall region and the centre of the bed due to effects induced by the hard, confining column wall. Consequences of these effects on local flow velocity in the column are analysed with flow simulations utilizing the lattice-Boltzmann method. The reconstructions of the bed structures reveal significant structural differences in the wall region (extending radially over approximately 62 particle diameters) compared to the centre of the column. It includes the local reduction of the external porosity by up to 10% and an increase of the mean particle diameter by up to 3%, resulting in a decrease of the local flow velocity by up to 23%. In addition, four (more ordered) layers of particles in the direct vicinity of the column wall induce local velocity fluctuations by up to a factor of three regarding the involved velocity amplitudes. These observations highlight the impact of radial variations in packing microstructure on band migration and column performance. This knowledge on morphological peculiarities of column wall effects helps guiding us towards further optimization of the packing process for analytical HPLC columns.

4.1 Introduction

The reduction of the particle diameter and chromatographic bed length resulted in a substantial increase of the performance of packed HPLC columns during the last decades [1]. However, the art and science of column packing remains a key behind ultrahigh performance. For modern analytical columns, Gritti and Guiochon [2] estimated that eddy dispersion contributes by about 75% to band broadening at the optimal velocity (corresponding to the minimum of the plate height curve) in the separation of small analytes and identified transcolumen heterogeneities as major part of this eddy dispersion contribution. These heterogeneities are formed during the slurry packing process due to the complex interaction of the slurry with the hard column wall. Efficiency losses in the vicinity of the column wall have already been observed in the 1970s for dry-packed columns by Knox et al. [3] and by Eon [4]. In addition, a reduction of local flow velocity was observed for slurry-packed columns by Baur et al. [5,6] in the late 1980s. Following these early works, Guiochon and co-workers presented a series of studies closer investigating this issue in the 1990s. They used local amperometric [7] and fluorescence detection [8] at different positions at the column outlet to record retention times and peak width locally. Measured linear velocities in the wall region were 2–13% lower than those in the bulk region [9–11].

The first visual proof of a combination of two wall effects was reported by Shalliker et al. [12] in 2000, using a transparent 17 mm inner diameter \times 100 mm length borosilicate glass column packed with relatively large (21 μm) C18 silica particles. Iodine was chosen as unretained analyte to allow for a simple optical visualization of flow inequalities. The obtained photographs revealed very high velocities in close vicinity of the column wall followed by lower-than-average velocities near the wall before almost constant velocity in the bulk region is reached. They described two wall effects in the bed structure of the column as becoming responsible for this flow maldistribution. The first one is the well-known geometrical wall effect. The hard spherical particles cannot penetrate the flat, hard column wall, and thus a first, highly ordered layer of particles touching the wall is formed. This first layer is followed by several particle layers with decreasing order until a random packing structure is reached. The region between the more ordered particle layers directly at the wall and the bulk packing region reflects another (second) wall effect and shows a higher packing density than the bulk region of the bed. The extension of the region affected by the second wall effect may vary from 30 up to 100 particle diameters [3–6] and depends on the column diameter [9]. Based on their observations, Shalliker et al. [12] proposed a characteristic radial distribution of the external (or interstitial) porosity in the packing: It tends to unity at the wall, followed by a global minimum after a distance from the wall of ca. one particle radius. This is followed by a dampened oscillation of the porosity profile caused by the gradually reduced order in subsequent particle layers. After a random bed microstructure is reached, the porosity is still lower than in the bulk region but slowly approaches the bulk value with increasing distance from the wall. The impact of the geometrical wall effect on the velocity profile and eddy dispersion has been simulated for computer-generated, cylindrically confined sphere packings [13,14]. The radial velocity profile reflects the distribution of external porosity, except at and near the column wall, where

the velocity decays to zero due to the no-slip velocity boundary condition at the solid-liquid interface represented by the column wall (cf. Figs. 7 and 8 in [13]).

After 2000, further efforts were made to elaborate on a more detailed picture of packed columns, in general, and wall effects, in particular [15]. Park et al. [16] identified the geometrical wall effect and also signatures of the second wall effect for preparative columns packed with soft polymeric particles. Closely related studies included the investigation of axial and radial diffusion coefficients in packed columns [17], the quantification of radial velocity variations [18], the determination of individual contributions to band broadening [19], the role of different column inner diameters [20], a discussion of better packing protocols [21], the impact of colloidal particle properties in packing columns for ion chromatography [22], hydrodynamic aspects during the packing of capillary columns [23], and ideal packing conditions for polar particles in enantioseparations [24,25]. One of the most detailed analysis of the contribution of transcolumn eddy dispersion to band broadening was conducted by Gritti and Guiochon in 2010 [26]. They estimated the part of the radial velocity profile in a column that is affected by wall effects and demonstrated that the influence on band broadening of wall effects decreases massively with higher retention factors. In that context, they also identified the significant contribution of sample diffusion through the porous particles to the effective radial diffusion and lateral exchange between analytes residing in different regions of the column. It particularly addresses RPLC, where enhanced transparticle mass transfer originates in surface diffusion of analytes in the acetonitrile ditch that exists at and near the terminal ends of the bonded C18 chains [27]. The molecular-detail picture obtained in [27] revealed that the acetonitrile molecules accumulate around the alkyl chain ends, forming an acetonitrile-rich border layer (or “ditch”) between bonded and mobile phase, which is more conducive to analyte mobility than the water-rich mobile phase.

Further research was conducted to investigate the formation of the wall region and the underlying physical processes. Guiochon and co-workers [28–30] analysed the forces which are active during the bed formation for columns packed under axial compression. They identified several important effects due to friction between the packing material and the column wall: (i) the shear stress on the packing material during bed consolidation, (ii) the shear strength of the bed (if the shear stress approaches the shear strength of the bed, the bed will deform), and (iii) the shear strength of the interface between bed and column wall (if the shear stress is at least equal to the shear strength of the interface, the bed will slip along the wall). The consolidation is usually not a continuous process but more a chaotic rearrangement when the current structure is ruptured due to applied stress. An elastic-plastic model was employed to identify variations in porosity and effective stress in axial and radial direction due to the applied stress. They identified a massive increase in the shear stress in the vicinity of the column wall compared to the central region of the bed accompanied by radial porosity gradients. However, no direct solution to avoid these transcolumn heterogeneities could be identified.

Instead of spending further research for the systematic minimization of wall effects different types of “active flow” designs were introduced since 2011 by Shalliker and co-workers [31,32]. The flow through the central section of the column was separated from the flow in the wall region by using multi-channel fittings. It significantly reduces the influence of the differences

between wall region and central region on the separation efficiency [31–35]. The design has not only been adapted to conventional analytical columns but also to preparative columns [36], narrow-bore columns [35], and to the operation under gradient elution conditions [37].

Further insights into the salient features of column beds can be obtained by the investigation of the bed microstructure. This can be realized by three-dimensional imaging and reconstruction methods that have great potential for deriving quantitative morphology-transport relationships of functional materials which, in turn, can be used for a systematic optimization of material properties [38–41]. We have already implemented techniques including confocal laser scanning microscopy (CLSM) [42,43] and focused ion-beam scanning electron microscopy (FIB-SEM) [44,45] to study a variety of chromatographic materials. This has allowed us to identify structural causes for the improved performance of the second-generation Chromolith monolithic columns in comparison to the first generation [46,47]. The combination with simulations of flow and transport in a reconstruction has revealed the extreme and so far unreached separation efficiency of these silica monolithic columns [48]. As another example, the reconstruction and morphological analysis of packed capillaries [49–52] has inspired further targeted optimization of the packing procedure, resulting in reduced plate heights close to unity over 1 m of packed-column length [53].



Figure 4.1. The analysed column packing (Acquity UPLC BEH C18 1.7 μm , 2.1 \times 50 mm) after its embedding in poly(divinylbenzene) and the subsequent extrusion from the encasing 2.1 mm inner diameter, 50 mm long stainless-steel column.

To our knowledge, no bed morphological reconstruction and analysis of a packed analytical column has been reported so far. The primary goal of this paper is to introduce a high-quality reconstruction procedure for packed analytical columns and to identify current bed morphological limitations to further improved separation efficiency. As representative column for ultrahigh performance liquid chromatography (UHPLC) we used an Acquity UPLC BEH C18 1.7 μm 2.1 \times 50 mm column. For the reconstruction of packing microstructure, we filled the interparticle pore space of this narrow-bore analytical column with divinylbenzene (DVB), polymerized the DVB, extruded the stabilized bed from the steel casing (Fig. 4.1), and applied FIB-SEM for three-dimensional imaging. Two image stacks were acquired and reconstructed:

a stack at the column wall extending towards the centre of the bed (to resolve wall effects), and a stack in the bulk region along the column axis (serving as a reference for the wall stack). The derived three-dimensional packing models for these regions allow the investigation of wall effects on a microstructural level. The influence of the wall effects on the local flow velocity in the column is subsequently analysed using flow simulations. The results of the morphological analysis and the flow simulations are discussed in the context of already reported characteristics of packing microstructure and regions affected by wall effects, the expected impact on the macroscopic flow heterogeneity, bed reconstructions obtained earlier from packed capillary columns, and the results of flow simulations in computer-generated packings.

4.2 Experimental

4.2.1 Chemicals and materials

The UHPLC columns (Acquity UPLC BEH C18 1.7 μm , 2.1 mm inner diameter \times 50 mm length) used for imaging and reconstruction and for acquisition of the SEM-based particle size distribution (PSD) were provided by Waters Corporation (Milford, MA). Methanol (HPLC grade) and NaOH (99%, p.a.) were supplied by Carl Roth (Karlsruhe, Germany). The DVB, azobis(isobutyronitrile) (AIBN, 98%), and basic aluminium oxide used for the column bed embedding were obtained from Sigma–Aldrich (Taufkirchen, Germany). HPLC grade water was provided by a Milli-Q gradient purification system (Merck Millipore, Darmstadt, Germany). Methanol ($\geq 99.8\%$, HiPerSolv Chromanorm) used for acquisition of a FIB-SEM independent PSD came from VWR International (Darmstadt, Germany). Conductive silver paint (Schnelltrocknendes Leitsilber ACHSEON 1415) and conductive carbon pads (PLANO Leit-Tabs) for sample mounting were obtained from Plano (Wetzlar, Germany).

4.2.2 Column bed embedding and FIB-SEM imaging

The bed of one of the narrow-bore columns (#01953123115708) was embedded in DVB, following a procedure developed for silica monoliths [44], to conserve the bed structure after extrusion of the bed from the column, to enhance image contrast in FIB-SEM, and to prevent depth-of-focus effects during imaging. Prior to the embedding, the stabilizer 4-*tert*-butylbenzene-1,2-diol was removed from the DVB by washing with 1 M NaOH and water followed by filtering over basic aluminium oxide. Then, 0.01% (w/w) AIBN was dissolved in the purified DVB and the resulting solution was purged with nitrogen for 5 min to remove residual oxygen. Subsequently, an empty steel column serving as reservoir was filled with the AIBN/DVB solution and connected to the sample column. Methanol was used as pushing solvent at 250 bar to fill the sample column with the AIBN/DVB solution. The filling process was continued until a droplet of the solution had formed at the outlet of the column. Afterwards, the column was disconnected and deposited in excess of the AIBN/DVB solution for 4 days. Column ends were sealed for transport to an oven and just slightly re-opened to avoid overpressure prior to placement in the oven under a nitrogen stream. Temperature was raised to 85 °C within 5 h to start polymerization of the DVB, maintained at that value for 20 h, and slowly reduced back to room temperature. After reaching room temperature, the outlet fitting

was removed and the embedded packing carefully extruded from its steel housing by pushing gently with liquid flow. The stainless steel column showed a smooth inner surface after extrusion of the bed and no residues of polymerized DVB. Also the extruded rod did not reveal any signs of deformation or damage under the microscope. An image of the packing after extrusion is shown in Fig. 4.1. Two macroscopic pieces were cut from this sample with a scalpel and mounted on the FIB-SEM sample holder: (i) a standing cylinder for acquiring an image stack from the column wall towards the centre of the bed (right panel in Fig. 4.2A), and (ii) a laying half-cylinder from the bulk region of the column to acquire an image stack along the flow direction (left panel in Fig. 4.2A). To increase the sample conductivity and reduce charging effects during FIB-SEM analysis, a thin Au layer was deposited at a current of 40 mA for 60 s onto the sample surfaces using a Sputter Coater 108auto (Cressington Scientific Instruments, Watford, UK).

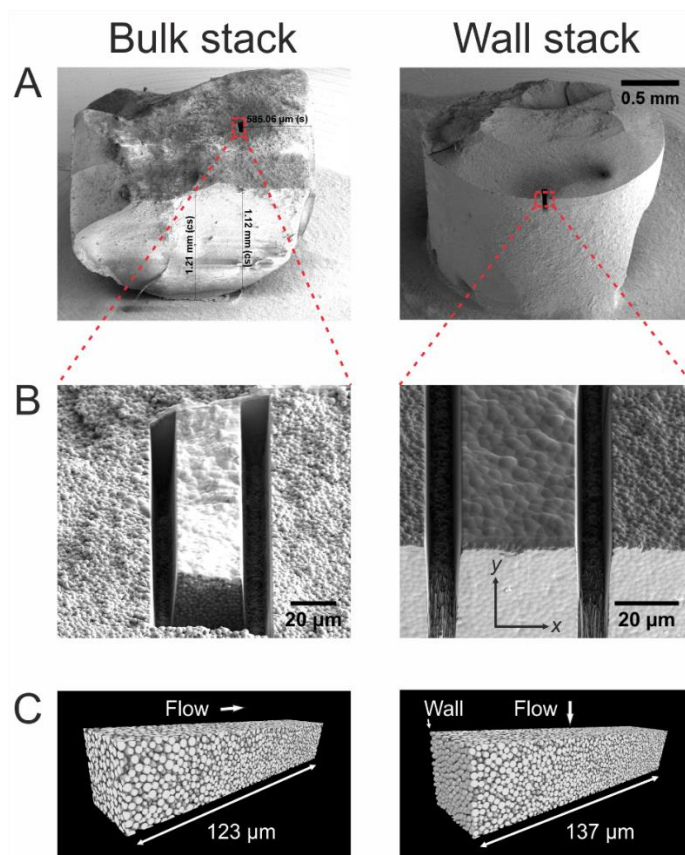


Figure 4.2. The two samples chosen for imaging (and resulting reconstructed image stacks) from the bulk region of the packing (along the flow direction; bulk stack) and from the wall region (towards the centre of the bed; wall stack). (A) The two macroscopic pieces cut from the column packing as mounted within the FIB-SEM setup after acquisition of the image stacks, highlighting the stack positions. (B) The two selected positions after preparation for imaging (before acquisition of the image stacks). The first slice of the subsequently acquired stacks is visible as the front surface. (C) The two fully reconstructed stacks with indication of the flow direction and the wall-bed interface.

FIB Slice&View tomography was performed using a Strata 400S dual-beam FIB system (FEI, Hillsboro, OR) at the Karlsruhe Nano Micro Facility (KNMF), Karlsruhe Institute of Technology (KIT), Germany. The SEM unit was operated at an acceleration voltage of 5 kV. Using a focused beam of Ga⁺ ions at 30 kV and a current of 2.8 nA (centre stack) or 0.9 nA (wall stack), a protective Pt layer (~1 μm thick) was deposited above the region of interest (ROI) to reduce curtaining effects. To create and freely expose the ROI, a focused beam of Ga⁺ ions at 30 kV and a current of 6.5 nA was used. Both ROIs (as prepared for the imaging) can be seen in Fig. 4.2B, which also provides the definition of the *x*- and *y*-direction referred to in the remainder of the discussion. A stack of images from the ROI is created with the Slice&View package of the instrument software, applying a 30 kV Ga⁺ ion beam with a current of 6.5 nA to remove material while imaging each newly generated surface by SEM (the final stack dimensions and resolutions after restoration and reconstruction are provided in Table 4.1, cf. Sections 4.2.4 and 4.2.5). The milling axis defined the *z*-direction in the image stack. For both ROIs, the imaging procedure had to be split into two stacks along the *z*-direction due to the large accumulated sample volume.

Table 4.1. Properties of the particles and bed reconstructions (cf. Fig. 4.2C).

	SEM	Bulk stack	Wall stack
Volume [μm ³]		21.6 × 21.2 × 123.5	27.5 × 27.4 × 132.0
Volume [<i>d_p</i> ³]		10.8 × 10.6 × 62.0	13.8 × 13.8 × 66.3
Voxel size [nm ³]		41.5 × 41.5 × 150	44.6 × 44.6 × 150
No. of particles	1003	8054	14433
<i>d_p</i> [μm]	1.99	1.97	2.00
Average porosity [–]		0.394	0.371
Voids per 1000 particles ^a		0.87	0.07

^a A void position is defined as larger void when it can accommodate a sphere with a diameter of at least 1.67 μm. This threshold corresponds to 10% of the PSD (cf. Fig. 4.4).

4.2.3 Scanning electron microscopy (SEM)

To validate the FIB-SEM based PSD of our reconstructions, we obtained an independent PSD from a second column (#01953123115759) using conventional SEM. For that purpose the BEH particles were flushed out of this column with methanol at 200 bar using an Agilent 1290 Infinity Bin Pump after removal of the column's outlet end-fitting. The extruded particles were initially dried at room temperature for 12 h and then further dried at 50 °C for 72 h. A fraction of them was deposited on a carbon film fixed to a SEM sample holder and placed under a stream of compressed air to remove loose particles. Particles were sputtered for 90 s with platinum using the sputtering chamber of a JSM-7500F scanning electron microscope (JEOL, Munich, Germany). Afterwards, the sample was transferred into the SEM chamber and images were acquired at 1 kV using the gentle beam high resolution mode and the secondary electron image at a working distance of 4.6 mm. The image resolution was set to 1280 × 960 pixels with a magnification of 4000x. The particle diameters were determined by overlaying circles in the

images using the same in-house written software as for the FIB-SEM images to ensure maximal comparability.

4.2.4 Image restoration

The restoration and reconstruction process to get representative three-dimensional packing models (Fig. 4.2C) is visualized in Fig. 4.3 for an exemplary slice from the image stack acquired next to the column wall. Initially, a multi-step process was applied to enhance image quality. Custom software, written in C# using Microsoft Visual Studio 2008, 2012, and 2013 (Microsoft Corporation, Redmond, WA), was used if not stated otherwise. The following steps were conducted first for the stacks acquired next to the column wall:

1. An autocorrelation algorithm was applied to the raw images (Fig. 4.3A) in an image section unaffected by the cutting procedure to determine stage drift between images using Matlab R2014b (The MathWorks, Inc., Natick, MA). The obtained shifts were used to correct the stage drift.
2. The movement of the stage along the y -axis during acquisition of the image stack (along the z -axis) was corrected.
3. To remove residual small drifts between the image slices, step 1 was repeated based on the front surface of the sample. Afterwards, the image size was reduced to the area of interest at the front surface of the sample (Fig. 4.3B).
4. Noise in the images was reduced using the PureDenoise [54] plugin for ImageJ [55,56].
5. The acquisition angle of the images was corrected by scaling along the y -axis using ImageJ to receive quadratic pixels in each slice.
6. Intensity variations within and between image slices were corrected by normalizing each slice to a fixed mean intensity based on a Gaussian blur filter with a radius of 150 pixels in ImageJ. The result is shown in Fig. 4.3C.
7. The two acquired image stacks were combined to represent the wall stack.

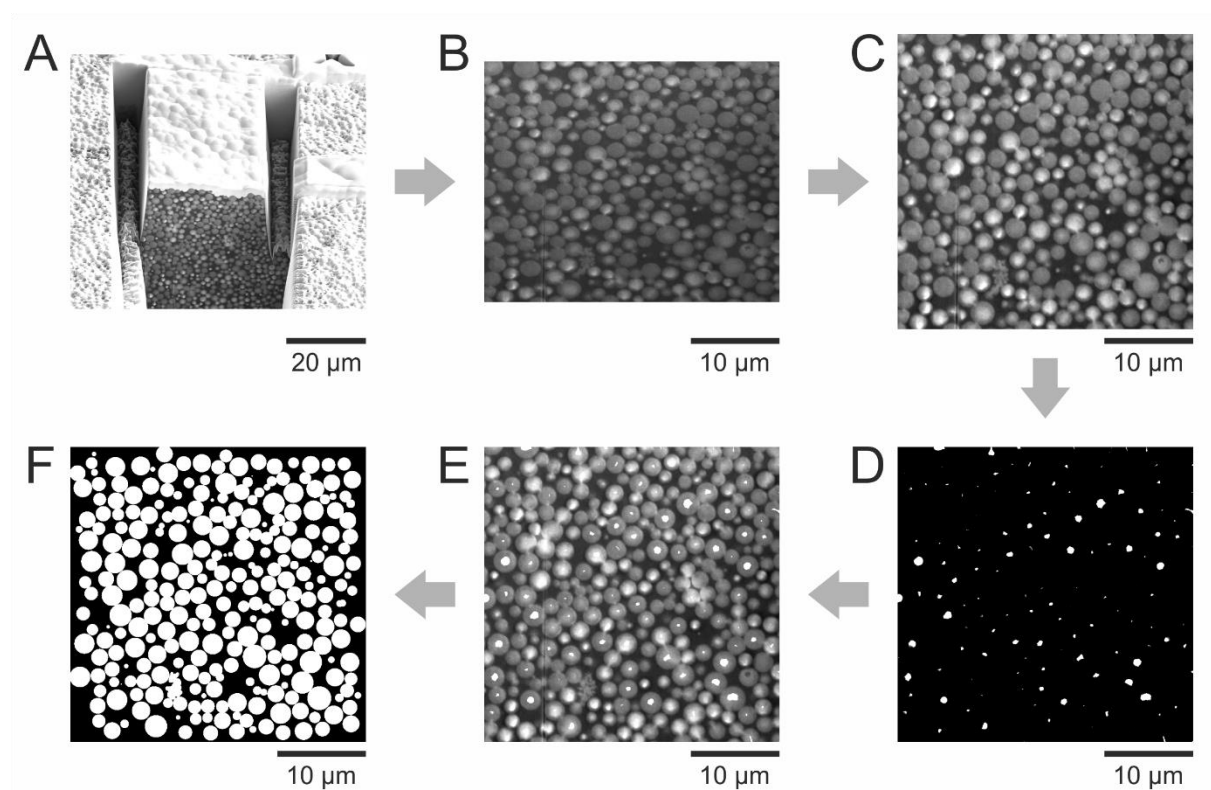


Figure 4.3. Reconstruction process for a single slice from the wall stack. (A) Image as acquired by FIB-SEM. (B) Area of interest extracted from the raw image after alignment of images. (C) Image slice after the restoration procedure. (D) Central particle sections identified for the generation of seed points for the fitting algorithm; (E) in addition, as overlay with the restored image. (F) Fully reconstructed image.

This outlined procedure was slightly modified for the image stacks acquired in the bulk region of the column packing:

1. An autocorrelation algorithm was applied to an image area unaffected by the measurement to determine stage drift between images using Matlab R2014b. The obtained shifts were used to correct the stage drift.
2. The movement of the stage along the y -axis during acquisition of the image stack (along the z -axis) was corrected and the image size reduced to the area at the front surface of the sample.
3. To remove residual small drifts between the image slices, step 1 was repeated based on the front surface of the sample.
4. The two acquired image stacks were combined to represent the bulk stack.
5. The acquisition angle of the images was corrected by scaling along the y -axis using ImageJ to receive quadratic pixels in each slice.
6. The stack was rotated by 8.5° along the y -axis using the TransformJ plugin for Fiji [55–57].
7. The stack was cut to the final size for three-dimensional reconstruction.

8. Intensity variations within and between image slices were corrected by normalizing each slice to a fixed mean intensity based on a Gaussian blur filter with a radius of 100 pixels in ImageJ.

4.2.5 Image reconstruction

We already established a reconstruction procedure for image stacks obtained from packed capillary columns using CLSM [49,51,58]. This procedure was modified according to the requirements of the FIB-SEM images in this study. Custom software, written in C# using Microsoft Visual Studio 2008, 2012, and 2013 (Microsoft Corporation, Redmond, WA), was used if not stated otherwise. The following steps were applied for representative reconstruction of the stacks:

1. Particle centres were estimated by applying an unsharp mask (20 pixels radius, mask weight: 0.99), an intensity threshold, a maximum filter (2 pixels), and a minimum filter (18 pixels) in ImageJ. The centres of the resulting clusters (Fig. 4.3D and E) were used to determine initial particle coordinates [58]. False positives were removed manually and missing particles added manually to the list of coordinates.
2. This preliminary list of particles was used as input file for the fitting algorithm. Spherical shells with increasing diameter around each coordinate were analysed until a defined number of pixels below a set intensity threshold was reached. The procedure was repeated with a variation of the x -, y -, and z -coordinate around the starting position. The largest determined radius and the corresponding coordinates were saved as describing the particle. For several equally sized “best positions”, the average position was saved.
3. The procedure was repeated over a wide range of intensity thresholds leading to several intensity threshold-dependent particle lists.
4. Lists were combined in a multi-step procedure starting from the list with the lowest intensity threshold, identifying the largest possible radius without unrealistic overlap to neighbouring particles for each particle.
5. Particles that could not be fitted without unrealistic overlap, isolated particles, and obvious misfits were removed from the resulting list and marked manually.
6. The final list of particles was used to draw a binarized image stack of spheres assuming perfect sphericity.
7. Non-spherical fragments were drawn manually using ImageJ based on the restored images and added to the sphere image stack. The resulting binarized image stacks are referred to as “reconstructions” in the remainder of the discussion (Fig. 4.3F).

4.2.6 Reconstruction analysis

Before analysing the reconstruction, 60 pixels in x - and y -direction and 15 slices in z -direction were removed from each border of a reconstruction to avoid border effects. Furthermore, each particle with its centre located in the removed border region was not considered for calculations of particle properties. The average external porosity of the bulk packing region $\varepsilon_{\text{bulk}}$ was

calculated using the mean slice intensities from the binarized reconstruction of the central bulk stack. The mean particle diameter d_p in the bulk packing region was calculated from the PSD for the central bulk stack. For accurate analysis of the reconstructed wall stack, the position of the wall was determined by fitting a plane to points that have been approximated manually as wall points in the image stack. The error compared to the treatment as cylindrical surface is negligible, because the width of the image stack ($\sim 27.5 \mu\text{m}$) is small compared to the column radius (1.05 mm). The smallest Euclidean distance to the plane describing the wall was calculated for any investigated particle and voxel. Radial profiles of the external porosity $\varepsilon(r)$ were derived by counting white pixels (particles) and black pixels (interparticle void) in bins with (i) a bin size of 312 nm and a step size of 44.6 nm for a highly resolved profile, and (ii) a bin size of $2.45 \mu\text{m}$ and a step size of 223 nm for a smoothed profile. Radial profiles of the mean particle diameter d_p were derived by assigning each particle (according to its centre) to a bin with (i) a bin size of 669 nm and a step size of 134 nm for a highly resolved profile, and (ii) a bin size of $18.3 \mu\text{m}$ and a step size of 446 nm for a smoothed profile. Packing voids were identified by inscribing spheres into the void space of a reconstruction, as done before in [51].

4.2.7 Simulation of fluid flow

The three-dimensional velocity field in the reconstructed wall stack was simulated with the lattice-Boltzmann method (LBM) [59,60] by adapting the same implementation and parameters as shown previously [13,14,61,62]. Key details are just briefly repeated here. LBM is equivalent to solving the Navier–Stokes equation for an incompressible fluid in the laminar flow regime at low Reynolds numbers, which is relevant for chromatographic columns. It means that the obtained velocity fields are assumed to scale linearly with pressure drop in the column or, equivalently, with the Reynolds number. As before, we used the LBM scheme with a single relaxation time, D3Q19 lattice, bounce-back boundary condition at the solid-liquid interface, and a uniform force acting on each voxel (an equivalent of the pressure drop inside the column). Prior to these simulations, the borders of the reconstruction were cut as described in Section 4.2.6 and afterwards mirror-reflected in all the three spatial directions. Our LBM implementation employs periodic boundary conditions. Applying the mirror reflection before the simulations ensures that the inlet and the outlet of a simulated domain (as well as the sides) match perfectly for periodic boundary conditions. To speed up simulations, the reconstruction was down-sampled by decreasing the linear resolution in every direction by two times, so that the number of voxels in the down-sampled reconstruction was 8 times less than the number of voxels in the original reconstruction. When computing the radial velocity profile (see Fig. 4.7 below), we used the voxels from the original reconstruction (not mirror-reflected along any axis) and excluded voxels that were closer than one average particle diameter to the boundaries of the reconstruction, except for voxels in the vicinity of the column wall. A smoothed profile has been calculated from the radial flow velocity distribution using the Savitzky–Golay method over a window of 50 points in Origin 2015 (OriginLab Corporation, Northampton, MA).

4.3 Results and discussion

In this paper, we report about the first three-dimensional physical reconstruction and morphological analysis of macroscopic bed sections from an embedded (and subsequently extruded) packing of a narrow-bore UHPLC column (Waters Acquity UPLC BEH C18 1.7 μm , 2.1×50 mm). Prior to the FIB-SEM imaging, a flow rate–efficiency analysis conducted by the supplier provided a maximum plate count N of 13,581, corresponding to $\sim 270,000$ plates per meter, at a flow rate of 0.45 mL/min (eluent: 100% acetonitrile, analyte: hexadecanophenone). It corresponds to a minimum plate height H_{min} of 3.7 μm and a reduced minimum plate height $h_{\text{min}} = H_{\text{min}}/d_p$ of ~ 1.9 (cf. Table 4.1 for the value of d_p), which is in good agreement with h_{min} -values reported for very similar columns [63–65]. The efficiency data for the investigated column can therefore be regarded as representative for state-of-the-art narrow-bore columns. To fix the packing structure as obtained after the packing process by the manufacturer, the bed was embedded in DVB and then extruded from its steel housing (Fig. 4.1). Two image stacks were acquired by FIB-SEM and reconstructed three-dimensionally as described in Sections 4.2.2, 4.2.4, and 4.2.5: (i) a stack covering the critical wall region, which allows us to resolve column wall effects, and (ii) a stack from the bulk packing region, acquired along the flow direction in the column, which provides the bulk packing properties as a reference and allows a comparison to other column packings.

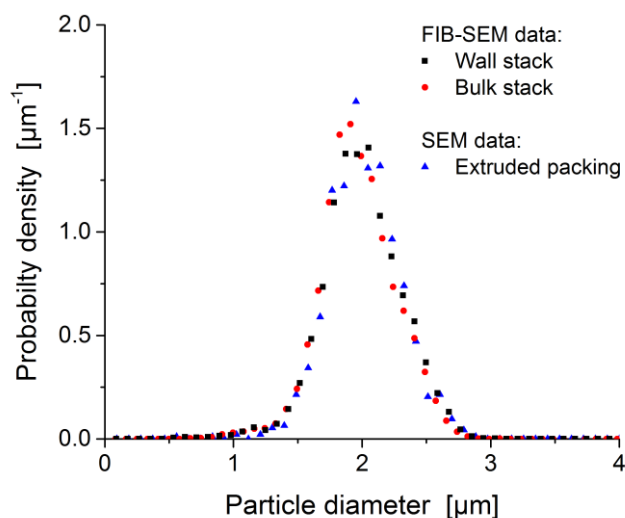


Figure 4.4. Particle size distribution (PSD) analysis for Acquity UPLC BEH C18 1.7 μm particles. FIB-SEM based PSDs for the reconstructed image stacks in comparison with the SEM-based PSD of the particles extruded from a second column.

Some general properties of the two stacks are summarized in Table 4.1. The obtained mean particle diameters of 1.97 μm (bulk stack) and 2.00 μm (wall stack) differ somewhat from the 1.7 μm given by the manufacturer. The latter has been obtained by the Coulter counter method, which determines the size of a particle based on the variation of electrical resistivity of an

electrolyte solution induced by the passing of the particle through a small orifice. To validate our reconstructions, the particles from a second, similar column were flushed out and imaged at high resolution using conventional SEM. This independent PSD is compared with the PSDs from the two reconstructions in Fig. 4.4. The mean particle diameter of $1.99 \mu\text{m}$ (SEM) is indeed highly similar to the values obtained from the FIB-SEM based reconstructions. A significant underestimation of the mean particle diameter by the Coulter counter method compared to SEM was previously documented for several types of commercially available particles in a study by Gritti and Guiochon [66]. Consequently, in further work data used from the Coulter counter method were calibrated by SEM images [67,68]. A similar difference between the mean particle diameter provided by the manufacturer and the actual value has been observed before with another batch of BEH particles used to pack capillary columns [49]. Therefore, the mean particle diameter d_p obtained from the analysis of the SEM data (cf. Table 4.1) is used in the remainder of our discussion.

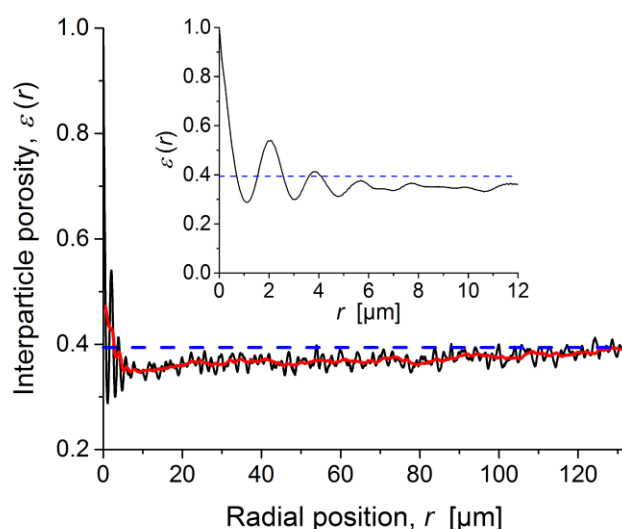


Figure 4.5. Radial porosity profile near the column wall ($r = 0$ at the wall): Distribution of the local interstitial void volume fraction $\varepsilon(r)$ in the reconstructed wall stack (cf. right panel in Fig. 4.2C). The black line is obtained after a little smoothing to remove noise, while the red line represents strong smoothing to retrieve the average local porosities. The dashed blue line reflects the porosity of the bulk stack (cf. left panel in Fig. 4.2C, $\varepsilon_{\text{bulk}} = 0.39$). The inset magnifies the oscillations in the porosity profile caused by the more ordered particle layers in the vicinity of the column wall.

A mean bulk value of the external porosity of $\varepsilon_{\text{bulk}} = 0.39$ is observed in the central region of the column (bulk stack). For the wall stack, the radially resolved profile of the external porosity $\varepsilon(r)$ is calculated and shown in Fig. 4.5, displaying the local interstitial void volume fraction as a function of the radial position, with $r = 0$ at the column wall. The black line represents a little smoothing to remove noise, while the red line is obtained after strong smoothing in order to get the variation of average values. An average external porosity higher than in the bulk region is realized in the direct vicinity of the wall, followed by a minimum value of 0.35 at approximately $r = 10 \mu\text{m}$. Thereafter, the average external porosity slowly increases until the bulk value is

reached at a distance of about $125 \mu\text{m}$ from the wall (equivalent to $\sim 62 d_p$). Our determined bulk porosity is in good agreement with external porosity values of 0.37 reported by Gritti and Guiochon [1,63,65] for similar columns. In addition, our observed radial extension of the wall region is consistent with the work performed by other groups: Knox et al. [3] proposed a radial extension of $\sim 30 d_p$, while a maximum value of $100 d_p$ can be estimated from the work by Baur et al. [5,6] and Yun and Guiochon [11]. Still other studies have reported data between these border values [4,10,12]. Gritti and Guiochon [20] studied chromatographically a number of columns that more closely reflect the narrow-bore column of this work. They estimated $\sim 100 \mu\text{m}$ for the radial extension of the wall region in 2.1 mm inner-diameter columns packed with 1.7 and $2.6 \mu\text{m}$ Kinetex core-shell particles, consistent with the ca. $125 \mu\text{m}$ found here for the $1.7 \mu\text{m}$ Acquity BEH particles based on the physical reconstruction analysis of the relevant packing sections in a narrow-bore column using FIB-SEM. To get a closer look at the geometrical wall effect (acting over a few particle layers next to the column wall), a magnification of the porosity profile in the direct vicinity of the wall is provided in the inset of Fig. 4.5. A value of unity is obtained at $r = 0$ and $\varepsilon(r)$ reaches a minimum of 0.275 at $r = 1 \mu\text{m}$, representing the centre of mass of the first and highly ordered particle layer. Three oscillations with decreasing amplitude follow, reflecting altogether four particle layers with a higher-than-bulk (but decreasing) structural homogeneity of the packing next to the column wall. After these four particle layers a random bed structure is attained.

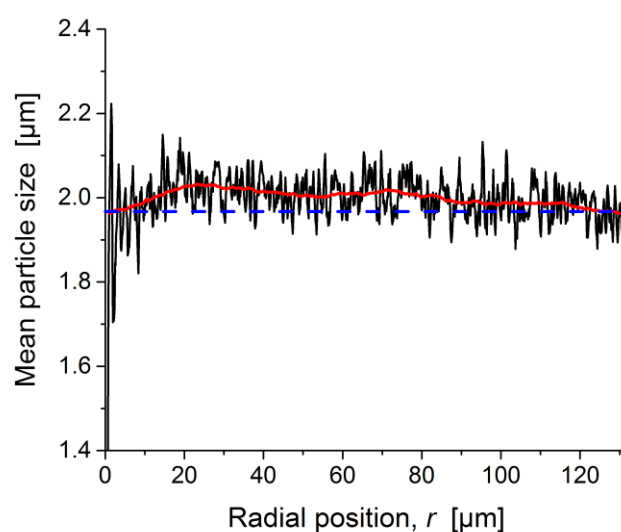


Figure 4.6. Radial profile of the mean particle size in the reconstructed wall stack ($r = 0$ at the wall, cf. right panel in Fig. 4.2C). The black line is obtained after a little smoothing to remove noise, while the red line represents strong smoothing to get average local values of the mean particle size. The dashed blue line reflects the mean particle diameter in the bulk stack ($1.97 \mu\text{m}$).

In our previous work on capillary columns [49–52], we identified a systematic radial discrimination of particles according to their size as morphological feature potentially contributing to transcolumen heterogeneities. Thus, we also analysed mean particle size locally

and resolved it in dependence of radial distance from the wall, as displayed in Fig. 4.6. Here, the black line represents a highly resolved profile, the red line a smoothed profile, and the dashed blue line mean particle size extracted from the bulk image stack. Compared to the reconstructed bulk section, the enrichment of larger particles in the reconstructed wall region is evident. When looking from the column centre towards the wall (right to left in Fig. 4.6), the mean particle diameter starts to increase from its bulk value of $1.97 \mu\text{m}$ to a maximum of $2.03 \mu\text{m}$ (corresponding to an increase of $\sim 3\%$) at a distance of $\sim 20 \mu\text{m}$ from the wall, followed by a decrease back to the bulk value of $1.97 \mu\text{m}$ for the first ordered layer of particles in touch with the wall.

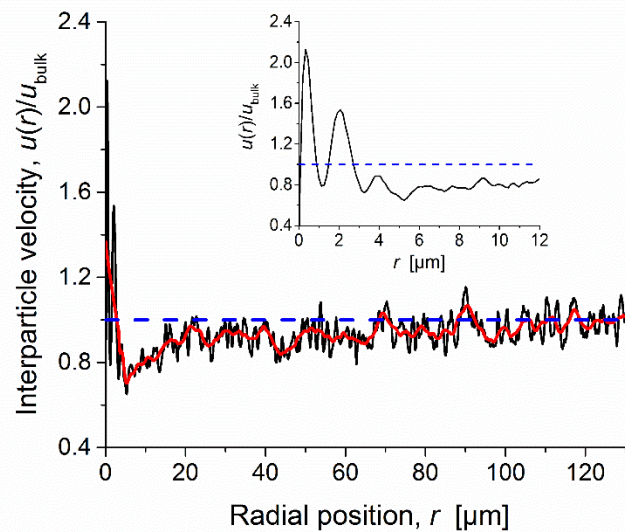


Figure 4.7. Radial velocity profile near the column wall ($r = 0$ at the wall): Distribution of the local mean velocity in the interstitial void space between particles, normalized by the interstitial velocity in the bulk packing region, as obtained from LBM flow simulations in the reconstructed structure of the wall stack (cf. right panel in Figure 4.2C). The black line is the calculated flow profile, while the red line represents smoothing to get average local values. The dashed blue line is the velocity at the transition between wall region and bulk packing region. The inset magnifies the situation closer to the wall, visualizing the zero-velocity requirement (directly at the wall) and the velocity extremes between the wall and the first, highly ordered layer of particles as well as between subsequent particle layers characterized by a decreasing packing order.

Subsequently, fluid flow through the bed structure in the wall region was simulated (Section 4.2.7) to investigate the combined influences of the geometrical wall effect, the shallow porosity gradient in the region affected by the second wall effect, and particle size-segregation on the flow velocity heterogeneity in the column. The radially resolved velocity profile for the wall stack (cf. right panel in Fig. 4.2C) is shown in Fig. 4.7, displaying the distribution of the local mean interstitial velocity (normalized by the mean interstitial velocity in the bulk packing region) as a function of the radial position, with $r = 0$ at the wall. The dashed blue line represents mean velocity at the border between wall region and bulk packing region. When looking from the column centre towards the wall (right to left in Fig. 4.7), the velocity first drops slowly from

the border between bulk and wall region until, after a distance of about 25 μm from the wall, a drop of $\sim 7\%$ is reached. Afterwards, the velocity drops quicker and reaches an overall decrease of $\sim 20\%$ at a distance of about 10 μm from the wall. As the more ordered layers of particles in close vicinity of the wall are entered, the velocity mirrors the oscillations in the porosity profile (cf. Fig. 4.5) and ultimately reaches a more than 2-fold increase over the bulk region within the gap between the first, highly ordered layer of particles and the wall, before it decays to zero directly at the wall-bed interface because of the no-slip velocity boundary condition. Since the relative drop in the local external porosity ($\sim 10\%$) is larger than the relative increase in the local mean particle diameter ($\sim 3\%$), the porosity variation expectedly dominates the velocity profile seen in Fig. 4.7.

The observed distributions of porosity and interstitial velocity are in excellent agreement with the qualitative results reported by Shalliker et al. [12] for a preparative column (17 mm inner-diameter \times 100 mm length borosilicate glass column packed with 21 μm -diameter C18 silica particles). Fig. 4.8 is adapted from Figs. 2 and 4 in [12] and shows the migration of unretained tracers injected either close to the column wall (A–E) or in the centre of the column (F). The evolution of the tracer profile provides insight about local velocities along the column radius. Higher-than-average velocities are observed directly at the column wall, while lower-than-average velocities are present in the region accounted to the second wall effect. It matches the expectations based on our radial porosity profile and the associated flow distribution. The substantially higher velocities of an unretained sample in the direct vicinity of the wall with respect to the bulk packing region observed in [12] are consistent with the velocity extremes originating in the more ordered particle layers and the locally increased average porosity (cf. red profile in Fig. 4.5). The actual decrease of velocity in the bed region affected by the second wall effect (seen in Fig. 4.7) also agrees with results of other groups. Their conclusions are mostly based on a local detection at the column outlet. Here, typical average velocities close to the wall were 2–8% lower than in the central region of the bed [10,12,18,26] and values reduced by up to 13% have been reported [11]. Our porosity and velocity profiles can also directly explain the often noticed lower separation efficiency in the wall region [3,5,7,9,10,12,18]. The presence of high and low velocities enhanced by channeling between the more ordered particle layers in direct vicinity of the wall imply a significant band dispersion in the wall region absent in the more uniform bulk packing region.

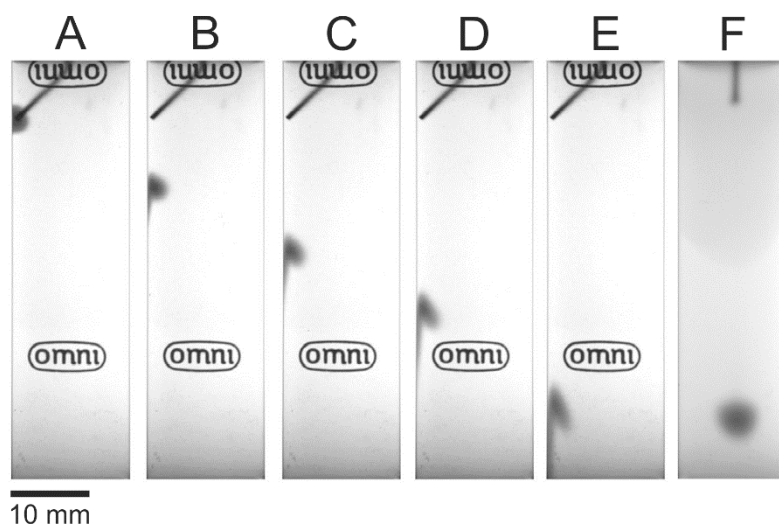


Figure 4.8. Photographs of a solution of iodine migrating along a chromatographic column (17 mm inner diameter \times 100 mm length) packed with 21 μm YMC C18 particles. (A–E) 10 μL injection at the column wall at a flow rate of 1.5 mL/min. Photographs acquired after: (A) time = 0 (initial injection), (B) time = 1.00 min, (C) time = 2.00 min, (D) time = 3.00 min, and (E) time = 4.60 min. (F) Photograph acquired after 4.60 min following a 20 μL injection in the column centre at a flow rate of 1.5 mL/min for comparison between a sample unaffected by the wall effects and a sample affected by wall effects. Reproduced from Shalliker et al. [12], Copyright \copyright 2000, with permission from Elsevier.

Another analysed aspect is the microscopic homogeneity of the bed structure in the bulk region of the column. For packed capillary columns, we have identified the formation of void defects in the bed [50–52], which can strongly impair the separation efficiency [69]. If such a packing defect can accommodate at least 10% of the particles from the PSD of the particle batch, it has been labelled as a larger void. Therefore, a similar analysis was conducted here. We identified seven larger voids in the bulk stack (corresponding to 0.87 voids per 1000 particles) and only one larger void in the wall stack (corresponding to 0.07 voids per 1000 particles). Voids that can accommodate at least 50% of the particles could not be found. The lower void number for the wall stack can be explained by its (on average) lower interstitial porosity, which reduces the probability of a larger free volume. Compared to our previous experience with the capillary columns, the voids observed here for the narrow-bore column are small and few. For example, two of the previously investigated capillary columns (packed with similar BEH particles at different slurry concentrations) showed 1.7 and 2.1 voids per 1000 particles, with a void volume that could be filled by at least 25% of the particles from the PSD, at almost identical bulk porosity of $\epsilon_{\text{bulk}} = 0.39$ [50].

The eddy dispersion characteristics and potential separation efficiency of (randomly-packed) bulk packing regions was investigated by simulations of flow and mass transport in computer-generated packings of nonporous particles with graded microstructural heterogeneity and similar bed porosity [14,70–72]. Obtained h_{min} -values ranged between 0.5 and 0.9. Complementary investigations with confined cylindrical packings realized at low column-to-particle diameter ratio ($d/d_p \leq 30$) [13,14] have demonstrated the principal contribution from the geometrical wall effect and differences in packing microstructure, resulting in h_{min} -values

for these confined packings between 0.83 and 1.46 in dependence of porosity and packing-generation protocol (cf. Figs. 7 and 9 in [14]). While a direct application of this insight to the investigated analytical column needs to be made with care (due to differences in the wall packing microstructure and the different column diameters), the actual loss in separation efficiency from the simulated h_{\min} -values to the value reported for the narrow-bore column ($h_{\min} \sim 1.9$) can be accounted to transcolumen heterogeneities induced by wall effects, in general, and by the second wall effect, in particular.

4.4 Conclusions

We adapted our imaging and reconstruction protocols established for packed capillary columns and monoliths to get the first three-dimensional reconstructions from a packed analytical column. Two image stacks were recorded and reconstructed from the exemplarily selected narrow-bore UHPLC column (Acquity UPLC BEH C18 1.7 μm , 2.1 \times 50 mm): one from its bulk region (with the image stack acquired along the column axis and macroscopic flow direction) and one from the wall region, i.e., from the wall-bed interface towards the centre of the bed, sufficiently far to include any wall effects before the bulk packing structure and its characteristics are attained.

The bulk stack of the analytical packing shows a mean bulk porosity of $\varepsilon_{\text{bulk}} = 0.39$ and only (very) few packing defects. Simulations of flow and eddy dispersion in computer-generated bulk packings with similar microstructure and packing density predict high separation efficiencies for this type of fictitious, infinite packing [70–72], which is confirmed by the success of the “active flow” designs [31–37]. In turn, this first, sufficiently large reconstruction (along the flow direction, cf. left panel in Fig. 4.2C) of an intact packing microstructure from the bulk region of an analytical column could be employed as model to conduct similar simulations to validate results and corroborate predictions based on computer-generated packings.

The second bed reconstruction extends from the column wall towards the centre of the bed in order to investigate the first, geometrical wall effect and the second wall effect. They pose a fundamental challenge in the further optimization of column efficiency and have so far been observed for any type of packed column: dry packed [3,4], slurry packed [5,7,8], packed under axial compression [11,15,28], columns packed with polymer particles [16], conventional and narrow-bore analytical columns [20], capillary columns [52], and preparative columns [9,12,17]. The quantification of the wall effects in most prior work on packed analytical columns was conducted via band detection at several positions at the column outlet, limiting the resolution. Even the most detailed investigation by Shalliker et al. [12] (cf. Fig. 4.8) was based on optical imaging with limited resolution. The highly resolved three-dimensional reconstruction utilizing FIB-SEM imaging in the present study allows the assessment of wall effects on the scale of individual particles.

The motivation for this investigation was to present a bed reconstruction procedure for analytical columns and to derive the microstructural details behind wall effects in a narrow-bore column, in particular. The analysed data appear to be representative of wall effects along the column (with the possible exception of the inlet and outlet regions), as supported by the

following observations: (i) the mutual consistency between the two (wall and bulk) stacks, which have been obtained at different positions along the column (i.e., the radial parameter profiles for the wall stack approach smoothly the mean values of the bulk stack); and (ii) the excellent agreement between our local morphological analysis and results of macroscopic (column-scale) experimental studies on wall effects. Especially the consistency with the band visualization work of Shalliker et al. [12] and the close agreement with the chromatographic analysis of wall effects in a similar narrow-bore column of Gritti and Guiochon [20] have to be emphasized here.

The presented approach will therefore guide the optimization of column packing towards the systematic reduction of wall effects and thereby also assists in adjustments of “active flow” designs for a specific column geometry or application. Furthermore, the approach has the potential to resolve the ongoing debate on the origin behind the different performance of analytical columns packed with core-shell and fully porous particles. For capillary columns, our detailed studies of packing conditions (utilizing a similar approach) have allowed the reproducible packing of ultra-efficient columns due to the almost entire suppression of wall effects, realized by combining high slurry concentrations with sonication during the packing and bed consolidation process [49–53].

Acknowledgement

The FIB-SEM work reported in this paper has been supported by the Karlsruhe Nano Micro Facility (KNMF), Karlsruhe Institute of Technology (Karlsruhe, Germany), under the KNMF long-term user proposal 2015-014-008069. The simulation work reported in this paper has been supported by the Deutsche Forschungsgemeinschaft DFG (Bonn, Germany) under grant TA 268/9–1. We thank the John von Neumann Institute for Computing (NIC) and the Jülich Supercomputing Center (JSC), Forschungszentrum Jülich (FZJ, Jülich, Germany), for the allocation of a special CPU-time grant (NIC project number: 10214, JSC project ID: HMR 10). Further, we thank Waters Corporation (Milford, MA) for the gift of the narrow-bore columns and Professor Andrew Shalliker (University of Western Sydney, Parramatta, NSW, Australia) for high-resolution images of Fig. 4.8.

References

- [1] F. Gritti, G. Guiochon, The current revolution in column technology: How it began, where is it going? *J. Chromatogr. A* 1228 (2012) 2–19.
- [2] F. Gritti, G. Guiochon, Perspectives on the evolution of the column efficiency in liquid chromatography, *Anal. Chem.* 85 (2013) 3017–3035.
- [3] J.H. Knox, G.R. Laird, P.A. Raven, Interaction of radial and axial dispersion in liquid chromatography in relation to the “infinite diameter effect”, *J. Chromatogr. A* 122 (1976) 129–145.
- [4] C.H. Eon, Comparison of broadening patterns in regular and radially compressed large-diameter columns, *J. Chromatogr. A* 149 (1978) 29–42.
- [5] J.E. Baur, E.W. Kristensen, R.M. Wightman, Radial dispersion from commercial high-

- performance liquid chromatography columns investigated with microvoltammetric electrodes, *Anal. Chem.* 60 (1988) 2334–2338.
- [6] J.E. Baur, R.M. Wightman, Microcylinder electrodes as sensitive detectors for high-efficiency, high-speed liquid chromatography, *J. Chromatogr. A* 482 (1989) 65–73.
- [7] T. Farkas, J.Q. Chambers, G. Guiochon, Column efficiency and radial homogeneity in liquid chromatography, *J. Chromatogr. A* 679 (1994) 231–245.
- [8] T. Farkas, M.J. Sepaniak, G. Guiochon, Column radial homogeneity in high-performance liquid chromatography, *J. Chromatogr. A* 740 (1996) 169–181.
- [9] T. Farkas, M.J. Sepaniak, G. Guiochon, Radial distribution of the flow velocity, efficiency and concentration in a wide HPLC column, *AIChE J.* 43 (1997) 1964–1974.
- [10] T. Farkas, G. Guiochon, Contribution of the radial distribution of the flow velocity to band broadening in HPLC columns, *Anal. Chem.* 69 (1997) 4592–4600.
- [11] T. Yun, G. Guiochon, Visualization of the heterogeneity of column beds, *J. Chromatogr. A* 760 (1997) 17–24.
- [12] R.A. Shalliker, B.S. Broyles, G. Guiochon, Physical evidence of two wall effects in liquid chromatography, *J. Chromatogr. A* 888 (2000) 1–12.
- [13] S. Khirevich, A. Hölzel, A. Seidel-Morgenstern, U. Tallarek, Geometrical and topological measures for hydrodynamic dispersion in confined sphere packings at low column-to-particle diameter ratios, *J. Chromatogr. A* 1262 (2012) 77–91.
- [14] A. Daneyko, S. Khirevich, A. Hölzel, A. Seidel-Morgenstern, U. Tallarek, From random sphere packings to regular pillar arrays: Effect of the macroscopic confinement on hydrodynamic dispersion, *J. Chromatogr. A* 1218 (2011) 8231–8248.
- [15] R.A. Shalliker, V. Wong, B.S. Broyles, G. Guiochon, Visualization of bed compression in an axial compression liquid chromatography column, *J. Chromatogr. A* 977 (2002) 213–223.
- [16] J.C. Park, K. Raghavan, S.J. Gibbs, Axial development and radial non-uniformity of flow in packed columns, *J. Chromatogr. A* 945 (2002) 65–81.
- [17] R.A. Shalliker, B.S. Broyles, G. Guiochon, Axial and radial diffusion coefficients in a liquid chromatography column and bed heterogeneity, *J. Chromatogr. A* 994 (2003) 1–12.
- [18] J.A. Abia, K.S. Mriziq, G.A. Guiochon, Radial heterogeneity of some analytical columns used in high-performance liquid chromatography, *J. Chromatogr. A* 1216 (2009) 3185–3191.
- [19] F. Gritti, G. Guiochon, Non-invasive measurement of eddy diffusion in very efficient liquid chromatography columns packed with sub-3 μm shell particles, *Chem. Eng. Sci.* 65 (2010) 6327–6340.
- [20] F. Gritti, G. Guiochon, Kinetic investigation of the relationship between the efficiency of columns and their diameter, *J. Chromatogr. A* 1218 (2011) 1592–1602.
- [21] J.J. Kirkland, J.J. DeStefano, The art and science of forming packed analytical high-performance liquid chromatography columns, *J. Chromatogr. A* 1126 (2006) 50–57.
- [22] M.F. Wahab, C.A. Pohl, C.A. Lucy, Colloidal aspects and packing behaviour of charged microparticulates in high efficiency ion chromatography, *J. Chromatogr. A* 1270 (2012)

- 139–146.
- [23] J.P.C. Vissers, M.A. Hoeben, J. Laven, H.A. Claessens, C.A. Cramers, Hydrodynamic aspects of slurry packing processes in microcolumn liquid chromatography, *J. Chromatogr. A* 883 (2000) 11–25.
- [24] O.H. Ismail, L. Pasti, A. Ciogli, C. Villani, J. Kocergin, S. Anderson, F. Gasparrini, A. Cavazzini, M. Catani, Pirkle-type chiral stationary phases on core-shell and fully porous particles: Are superficially porous particles always the better choice towards ultrafast high-performance enantioseparations? *J. Chromatogr. A* 1466 (2016) 96–104.
- [25] M. Catani, O.H. Ismail, F. Gasparrini, M. Antonelli, L. Pasti, N. Marchetti, S. Felletti, A. Cavazzini, Recent advancements and future directions of superficially porous chiral stationary phases for ultrafast high-performance enantioseparations, *Analyst* 142 (2017), 555–566.
- [26] F. Gritti, G. Guiochon, Relationship between trans-column eddy diffusion and retention in liquid chromatography: Theory and experimental evidence, *J. Chromatogr. A* 1217 (2010) 6350–6365.
- [27] J. Rybka, A. Höltzel, S.M. Melnikov, A. Seidel-Morgenstern, U. Tallarek, A new view on surface diffusion from molecular dynamics simulations of solute mobility at chromatographic interfaces, *Fluid Phase Equilib.* 407 (2016) 177–187.
- [28] G. Guiochon, E. Drumm, D. Cherrak, Evidence of a wall friction effect in the consolidation of beds of packing materials in chromatographic columns, *J. Chromatogr. A* 835 (1999) 41–58.
- [29] B.G. Yew, J. Ureta, R.A. Shalliker, E.C. Drumm, G. Guiochon, Mechanics of column beds: II. Modeling of coupled stress-strain-flow behavior, *AIChE J.* 49 (2003) 642–664.
- [30] B.G. Yew, E.C. Drumm, G. Guiochon, Mechanics of column beds: I. Acquisition of the relevant parameters, *AIChE J.* 49 (2003) 626–641.
- [31] M. Camenzuli, H.J. Ritchie, J.R. Ladine, R.A. Shalliker, The design of a new concept chromatography column, *Analyst* 136 (2011) 5127–5130.
- [32] R.A. Shalliker, M. Camenzuli, L. Pereira, H.J. Ritchie, Parallel segmented flow chromatography columns: Conventional analytical scale column formats presenting as a “virtual” narrow bore column, *J. Chromatogr. A* 1262 (2012) 64–69.
- [33] F. Gritti, G. Guiochon, Effect of parallel segmented flow chromatography on the height equivalent to a theoretical plate. II - Performances of 4.6 mm × 30 mm columns packed with 2.6 μm Accucore-C18 superficially porous particles, *J. Chromatogr. A* 1314 (2013) 44–53.
- [34] M. Camenzuli, H.J. Ritchie, R.A. Shalliker, Improving HPLC separation performance using parallel segmented flow chromatography, *Microchem. J.* 111 (2013) 3–7.
- [35] R.A. Shalliker, H. Ritchie, Segmented flow and curtain flow chromatography: Overcoming the wall effect and heterogeneous bed structures, *J. Chromatogr. A* 1335 (2014) 122–135.
- [36] M. Camenzuli, H.J. Ritchie, J.R. Ladine, R.A. Shalliker, Active flow management in preparative chromatographic separations: A preliminary investigation into enhanced separation using a curtain flow inlet fitting and segmented flow outlet fitting, *J. Sep. Sci.*

- 35 (2012) 410–415.
- [37] M. Camenzuli, H.J. Ritchie, R.A. Shalliker, Gradient elution chromatography with segmented parallel flow column technology: A study on 4.6 mm analytical scale columns, *J. Chromatogr. A* 1270 (2012) 204–211.
- [38] P. Levitz, Toolbox for 3D imaging and modeling of porous media: Relationship with transport properties, *Cem. Concr. Res.* 37 (2007) 351–359.
- [39] T. Müllner, K.K. Unger, U. Tallarek, Characterization of microscopic disorder in reconstructed porous materials and assessment of mass transport-relevant structural descriptors, *New J. Chem.* (2016) 3993–4015.
- [40] D. Enke, R. Gläser, U. Tallarek, Sol-gel and porous glass-based silica monoliths with hierarchical pore structure for solid-liquid catalysis, *Chem. Ing. Tech.* 88 (2016) 1561–1585.
- [41] T. Müllner, A. Zankel, A. Höltzel, F. Svec, U. Tallarek, Morphological properties of methacrylate-based polymer monoliths: From gel porosity to macroscopic inhomogeneities, *Langmuir* 33 (2017) 2205–2214.
- [42] S. Bruns, T. Hara, B.M. Smarsly, U. Tallarek, Morphological analysis of physically reconstructed capillary hybrid silica monoliths and correlation with separation efficiency, *J. Chromatogr. A* 1218 (2011) 5187–5194.
- [43] S. Bruns, D. Stoeckel, B.M. Smarsly, U. Tallarek, Influence of particle properties on the wall region in packed capillaries, *J. Chromatogr. A* 1268 (2012) 53–63.
- [44] D. Stoeckel, C. Kübel, K. Hormann, A. Höltzel, B.M. Smarsly, U. Tallarek, Morphological analysis of disordered macroporous-mesoporous solids based on physical reconstruction by nanoscale tomography, *Langmuir* 30 (2014) 9022–9027.
- [45] D. Stoeckel, C. Kübel, M.O. Loeh, B.M. Smarsly, U. Tallarek, Morphological analysis of physically reconstructed silica monoliths with submicrometer macropores: Effect of decreasing domain size on structural homogeneity, *Langmuir* 31 (2015) 7391–7400.
- [46] K. Hormann, T. Müllner, S. Bruns, A. Höltzel, U. Tallarek, Morphology and separation efficiency of a new generation of analytical silica monoliths, *J. Chromatogr. A* 1222 (2012) 46–58.
- [47] K. Hormann, U. Tallarek, Analytical silica monoliths with submicron macropores: Current limitations to a direct morphology-column efficiency scaling, *J. Chromatogr. A* 1312 (2013) 26–36.
- [48] D. Hlushkou, K. Hormann, A. Höltzel, S. Khirevich, A. Seidel-Morgenstern, U. Tallarek, Comparison of first and second generation analytical silica monoliths by pore-scale simulations of eddy dispersion in the bulk region, *J. Chromatogr. A* 1303 (2013) 28–38.
- [49] S. Bruns, J.P. Grinias, L.E. Blue, J.W. Jorgenson, U. Tallarek, Morphology and separation efficiency of low-aspect-ratio capillary ultrahigh pressure liquid chromatography columns, *Anal. Chem.* 84 (2012) 4496–4503.
- [50] S. Bruns, E.G. Franklin, J.P. Grinias, J.M. Godinho, J.W. Jorgenson, U. Tallarek, Slurry concentration effects on the bed morphology and separation efficiency of capillaries packed with sub-2 μm particles, *J. Chromatogr. A* 1318 (2013) 189–197.
- [51] A.E. Reising, J.M. Godinho, K. Hormann, J.W. Jorgenson, U. Tallarek, Larger voids in

- mechanically stable, loose packings of 1.3 μm frictional, cohesive particles: Their reconstruction, statistical analysis, and impact on separation efficiency, *J. Chromatogr. A* 1436 (2016) 118–132.
- [52] A.E. Reising, J.M. Godinho, J.W. Jorgenson, U. Tallarek, Bed morphological features associated with an optimal slurry concentration for reproducible preparation of efficient capillary ultrahigh pressure liquid chromatography columns, *J. Chromatogr. A* 1504 (2017) 71–82.
- [53] J.M. Godinho, A.E. Reising, U. Tallarek, J.W. Jorgenson, Implementation of high slurry concentration and sonication to pack high-efficiency, meter-long capillary ultrahigh pressure liquid chromatography columns, *J. Chromatogr. A* 1462 (2016) 165–169.
- [54] F. Luisier, PureDenoise, Biomedical Imaging Group, École Polytechnique Fédéral de Lausanne, <http://bigwww.epfl.ch/algorithms/denoise/>, 2010.
- [55] W.S. Rasband, ImageJ, U. S. National Institutes of Health, Bethesda, MD, <http://imagej.nih.gov/ij/>, 1997–2014.
- [56] C.A. Schneider, W.S. Rasband, K.W. Eliceiri, NIH Image to ImageJ: 25 years of image analysis, *Nat. Methods* 9 (2012) 671–675.
- [57] J. Schindelin, I. Arganda-Carreras, E. Frise, V. Kaynig, M. Longair, T. Pietzsch, et al., Fiji: an open-source platform for biological-image analysis, *Nat. Methods* 9 (2012) 676–682.
- [58] S. Bruns, U. Tallarek, Physical reconstruction of packed beds and their morphological analysis: Core-shell packings as an example, *J. Chromatogr. A* 1218 (2011) 1849–1860.
- [59] S. Chen, G.D. Doolen, Lattice Boltzmann method for fluid flows, *Annu. Rev. Fluid Mech.* 30 (1998) 329–364.
- [60] S. Khirevich, I. Ginzburg, U. Tallarek, Coarse- and fine-grid numerical behavior of MRT/TRT lattice-Boltzmann schemes in regular and random sphere packings, *J. Comput. Phys.* 281 (2015) 708–742.
- [61] S. Khirevich, A. Höltzel, D. Hlushkou, U. Tallarek, Impact of conduit geometry and bed porosity on flow and dispersion in noncylindrical sphere packings, *Anal. Chem.* 79 (2007) 9340–9349.
- [62] A. Daneyko, D. Hlushkou, S. Khirevich, U. Tallarek, From random sphere packings to regular pillar arrays: Analysis of transverse dispersion, *J. Chromatogr. A* 1257 (2012) 98–115.
- [63] F. Gritti, G. Guiochon, Fundamental chromatographic equations designed for columns packed with very fine particles and operated at very high pressures. Applications to the prediction of elution times and the column efficiencies, *J. Chromatogr. A* 1206 (2008) 113–122.
- [64] F. Gritti, M. Martin, G. Guiochon, Influence of viscous friction heating on the efficiency of columns operated under very high pressures, *Anal. Chem.* 81 (2009) 3365–3384.
- [65] F. Gritti, G. Guiochon, Performance of new prototype packed columns for very high pressure liquid chromatography, *J. Chromatogr. A* 1217 (2010) 1485–1495.
- [66] F. Gritti, G. Guiochon, Comparative study of the performance of columns packed with several new fine silica particles. Would the external roughness of the particles affect

-
- column properties? *J. Chromatogr. A* 1166 (2007) 30–46.
- [67] F. Gritti, T. Farkas, J. Heng, G. Guiochon, On the relationship between band broadening and the particle-size distribution of the packing material in liquid chromatography: Theory and practice, *J. Chromatogr. A* 1218 (2011) 8209–8221.
- [68] F. Gritti, G. Guiochon, Comparison of heat friction effects in narrow-bore columns packed with core-shell and totally porous particles, *Chem. Eng. Sci.* 65 (2010) 6310–6319.
- [69] M.R. Schure, R.S. Maier, How does column packing microstructure affect column efficiency in liquid chromatography? *J. Chromatogr. A* 1126 (2006) 58–69.
- [70] S. Khirevich, A. Daneyko, A. Hörtzel, A. Seidel-Morgenstern, U. Tallarek, Statistical analysis of packed beds, the origin of short-range disorder, and its impact on eddy dispersion, *J. Chromatogr. A* 1217 (2010) 4713–4722.
- [71] A. Daneyko, A. Hörtzel, S. Khirevich, U. Tallarek, Influence of the particle size distribution on hydraulic permeability and eddy dispersion in bulk packings, *Anal. Chem.* 83 (2011) 3903–3910.
- [72] A. Daneyko, D. Hlushkou, V. Baranau, S. Khirevich, A. Seidel-Morgenstern, U. Tallarek, Computational investigation of longitudinal diffusion, eddy dispersion, and trans-particle mass transfer in bulk, random packings of core-shell particles with varied shell thickness and shell diffusion coefficient, *J. Chromatogr. A* 1407 (2015) 139–156.

IV. Conclusions and perspective

In this work, the complex relationships between packing conditions, bed microstructure, and chromatographic separation efficiency were investigated for columns packed with porous silica particles used in HPLC. This included the utilization of highly sophisticated packing procedures, chromatographic characterisation, 3D imaging, reconstruction, morphological analysis of the obtained models, and LBM simulations of flow through the reconstructed structures. The obtained insights were used to understand the influence of individual packing parameters on the bed structure, to obtain insights into the process of bed formation, to understand the influence of the bed structure on the flow distribution and separation efficiency, and to identify opportunities to efficiently optimize the fabrication process.

For capillary columns, the slurry concentration was varied over a wide range using two types of particles: from 5 to 50 mg/mL for 1.3 μm BEH particles packed into 75 μm inner diameter columns with a length of 34 cm (Chapter 1) and from 5 to 200 mg/mL for 1.9 μm BEH particles packed into 75 μm inner diameter columns with a length of 45 cm (Chapter 2). Chromatographic characterisation was conducted with hydroquinone as weakly retained compound to investigate the fluid dynamics and identified an optimal intermediate slurry concentration for both particle types. 3D imaging and reconstruction based on CLSM revealed similar morphological origins for the observed column efficiencies. At low slurry concentrations, radial heterogeneities were demonstrated including porosity deviations between the wall region of the column and the centre of the column as well as particle size segregation. They are directly connected to an increased transcolumn eddy dispersion. With higher slurry concentration, an increased formation of packing defects in the form of larger voids with the size of a typical particle was observed. This alters both transchannel eddy dispersion and short-range interchannel eddy dispersion. In addition, a non-uniform void distribution could induce long-range interchannel and/or transcolumn eddy dispersion. These counteracting effects are balanced at intermediate slurry concentrations explaining the superior separation efficiency. The origin of these structural features was investigated by videos acquired during bed formation for concentrations of 10 mg/mL and 100 mg/mL. They showed significant differences in the behaviour of the slurry. At low concentrations, particles arrive individually with the highest mass flow in the centre of the column leading to a cone-shaped bed front, individual settling of particles and possible rearrangements. This offers freedom for radial discrimination of particles in the particle stream or during the settling process. At high concentrations, the bed formation occurs in a different way. Large patches of particles arrive at different positions along the column diameter resulting in continuous changes of the bed front. This suppresses radial heterogeneities but also prevents any chances for a relocation of particles and conserves possible gaps in the bed. The increasing aggregation can also explain the significant difference in the optimal slurry concentration for the two particle types (20 mg/mL for 1.3 μm versus 140 mg/mL for 1.9 μm). Interparticle forces become more important with a decrease in the particle diameter, especially for sub-2 μm particles. Thus, a significant amount of aggregation starts already at lower slurry concentrations for the smaller 1.3 μm particles. These results strongly pointed towards an opportunity to modify the packing process in order to pack columns with

even higher efficiencies. The combination of very high slurry concentration and ultrasonication during packing resulted in ultra-efficient columns with close to 500,000 plates over a length of 1 m corresponding to a reduced plate height near unity (Chapter 3). It can be concluded that the advantage of high slurry concentration was maintained (good radial homogeneity) while the sonication largely prevented the formation of unfavourable voids. These columns provide exceptional separation potential for very complex samples and are well suited for biological probes which provide only small sample volumes. While the handling of these columns is challenging due to high back-pressures and the sensitivity towards extra-column band broadening effects, recent studies have demonstrated the successful applications of such columns for the analysis of complex peptide mixtures [1] and digested rat hormones [2].

To conduct similar studies for columns of analytical format, a new imaging and reconstruction procedure is required due to intransparent column walls (usually stainless steel in contrast to fused silica for the capillary columns). FIB-SEM was selected as an adequate method and a commercial narrow-bore column was chosen as the sample (Chapter 4). The bed structure was stabilized with poly(divinylbenzene) and extruded from the steel housing. Imaging and reconstruction was conducted for the first time for a packed analytical column at two selected positions to illuminate the region affected by column wall effects and the bulk structure of the column bed. In addition, simulations of fluid flow demonstrated the effect of the structure on the flow profile in the column. The observed peculiarity of the bed structure in the wall region was found to be in excellent agreement with macroscopic and chromatographic (indirect) characterisations of the wall effects. At the same time, the microscopic bed structure on the scale of individual particles has been illuminated. Four more ordered layers of particles were observed directly at the column wall inducing velocity fluctuations by up to a factor of three. The random particle structure beyond the last ordered particle layer shows a densification with a porosity reduction by 10% and a 3% larger average particle diameter compared to the bulk region of the column, inducing a reduction in the local flow velocity by about 20%. When moving further towards the centre of the column, these values steadily approach the corresponding bulk values, which are reached after a distance of 125 μm from the column wall. The new reconstruction approach offers huge potential to address several interesting questions (often controversially) discussed for modern HPLC columns: Why do core-shell particles provide better performance than fully-porous particles with the same particle diameter in reversed-phase HPLC for conventional analytical columns [3]? Why is the same trend not observed for narrow-bore columns [3] and chiral phases in enantioseparations [4,5]? Which packing parameters influence the formation of wall effects and can they be optimized? Can the knowledge of the radial extension of wall effects be used to specifically optimize active flow designs [6] for a given application? A recent perspective discussing the choice of packing parameters has shown that optimal conditions differ drastically between capillary columns and columns with larger diameter [7].

Furthermore, computer simulations can be utilized to investigate the influence of individual structural features on the performance of a material. This has been conducted using computer generated packings, for example, in the case of different conduit shapes in HPLC microchips [8], the comparison of the bulk separation potential of narrow and wide PSD packings [9],

different bed porosities [9], and structural heterogeneity in unconfined bulk packings [10]. While these computer generated structures allow a wide variation of properties, imaging and reconstruction procedures allow to investigate morphology-transport relationships in real materials. For example, pore-scale simulations in reconstructed silica monolithic structures could explain the massive improvement in separation efficiency for the second generation of analytical silica monoliths compared to the first generation [11]. Similar studies can now be conducted using the obtained reconstructions of packed beds for capillary columns and narrow-bore analytical columns. This will be a unique chance to validate how realistic the results from computer generated structures are with respect to real structures and might help to identify structural features limiting separation efficiencies which have not yet been properly addressed.

References

- [1] K.M. Grinias, J.M. Godinho, E.G. Franklin, J.T. Stobaugh, J.W. Jorgenson, Development of a 45 kpsi ultrahigh pressure liquid chromatography instrument for gradient separations of peptides using long microcapillary columns and sub-2 μm particles, *J. Chromatogr. A* 1469 (2016) 60–67.
- [2] O. Mozziconacci, J.T. Stobaugh, R. Bommana, J. Woods, E. Franklin, J.W. Jorgenson, et al., Profiling the photochemical-induced degradation of rat growth hormone with extreme ultra-pressure chromatography–mass spectrometry utilizing meter-long microcapillary columns cacked with sub-2 μm particles, *Chromatographia* (2017).
- [3] G. Guiochon, F. Gritti, Shell particles, trials, tribulations and triumphs, *J. Chromatogr. A* 1218 (2011) 1915–1938.
- [4] O.H. Ismail, L. Pasti, A. Ciogli, C. Villani, J. Kocergin, S. Anderson, et al., Pirkle-type chiral stationary phase on core–shell and fully porous particles: are superficially porous particles always the better choice toward ultrafast high-performance enantioseparations? *J. Chromatogr. A* 1466 (2016) 96–104.
- [5] M. Catani, O.H. Ismail, F. Gasparini, M. Antonelli, L. Pasti, N. Marchetti, et al., Recent advancements and future directions of superficially porous chiral stationary phases for ultrafast high-performance enantioseparations, *Analyst*. 142 (2017) 555–566.
- [6] R.A. Shalliker, H. Ritchie, Segmented flow and curtain flow chromatography: overcoming the wall effect and heterogeneous bed structures, *J. Chromatogr. A* 1335 (2014) 122–135.
- [7] M. Farooq Wahab, D.C. Patel, R.M. Wimalasinghe, D.W. Armstrong, Fundamental and Practical Insights on the Packing of Modern High- Efficiency Analytical and Capillary Columns, (2017).
- [8] S. Khirevich, A. Höltzel, D. Hlushkou, U. Tallarek, Impact of conduit geometry and bed porosity on flow and dispersion in noncylindrical sphere packings, *Anal. Chem.* 79 (2007) 9340–9349.
- [9] A. Daneyko, A. Höltzel, S. Khirevich, U. Tallarek, Influence of the Particle Size Distribution on Hydraulic Permeability and Eddy Dispersion in Bulk Packings, *Anal. Chem.* 83 (2011) 3903–3910.

- [10] S. Khirevich, A. Hörtzel, A. Daneyko, A. Seidel-Morgenstern, U. Tallarek, Structure-transport correlation for the diffusive tortuosity of bulk, monodisperse, random sphere packings, *J. Chromatogr. A* 1218 (2011) 6489–6497.
- [11] D. Hlushkou, K. Hormann, A. Hörtzel, S. Khirevich, A. Seidel-Morgenstern, U. Tallarek, Comparison of first and second generation analytical silica monoliths by pore-scale simulations of eddy dispersion in the bulk region, *J. Chromatogr. A* 1303 (2013) 28–38.

V. Appendix

V.1 Curriculum vitae

Persönliche Daten

Arved Ernst Reising
Geburtsdatum: 19.04.1988
Geburtsort: Göttingen

Beruflicher Werdegang

05/2013 – 05/2017 Wissenschaftlicher Mitarbeiter
Philipps-Universität Marburg
Fachbereich Chemie

04/2009 – 02/2013 Studentische Hilfskraft
Philipps-Universität Marburg
Fachbereich Chemie

Ausbildung

05/2013 – heute Promotionsstudium
Philipps-Universität Marburg
Fachbereich Chemie
Betreuer: Prof. Dr. Ulrich Tallarek

04/2010 – 05/2013 Master of Science (Chemie)
Philipps-Universität Marburg

10/2011 – 03/2012 Erasmus-Austausch
University of Cambridge
Centre for Atmospheric Science

04/2007 – 03/2010 Bachelor of Science (Chemie)
Philipps-Universität Marburg

08/1999 – 06/2006 Gottfried Arnold Gymnasium Perleberg
Abitur

V.2 Publikationsverzeichnis

- [1] A.E. Reising, S. Schlabach, V. Baranau, D. Stoeckel, U. Tallarek, Analysis of packing microstructure and wall effects in a narrow-bore ultrahigh pressure liquid chromatography column using focused ion-beam scanning electron microscopy, *J. Chromatogr. A* 1513 (2017) 172–182. doi:10.1016/j.chroma.2017.07.049.
- [2] A.E. Reising, J.M. Godinho, J.W. Jorgenson, U. Tallarek, Bed morphological features associated with an optimal slurry concentration for reproducible preparation of efficient capillary ultrahigh pressure liquid chromatography columns, *J. Chromatogr. A* 1504 (2017) 71–82. doi:10.1016/j.chroma.2017.05.007.
- [3] M. von der Lehr, K. Hormann, A. Höltzel, L.S. White, A.E. Reising, M.F. Bertino, B.M. Smarsly, U. Tallarek, Mesopore etching under supercritical conditions – A shortcut to hierarchically porous silica monoliths, *Microporous Mesoporous Mater.* 243 (2017) 247–253. doi:10.1016/j.micromeso.2017.02.036.
- [4] J.M. Godinho, A.E. Reising, U. Tallarek, J.W. Jorgenson, Implementation of high slurry concentration and sonication to pack high-efficiency, meter-long capillary ultrahigh pressure liquid chromatography columns, *J. Chromatogr. A* 1462 (2016) 165–169. doi:10.1016/j.chroma.2016.08.002.
- [5] A.E. Reising, J.M. Godinho, K. Hormann, J.W. Jorgenson, U. Tallarek, Larger voids in mechanically stable, loose packings of 1.3 μm frictional, cohesive particles: Their reconstruction, statistical analysis, and impact on separation efficiency, *J. Chromatogr. A* 1436 (2016) 118–132. doi:10.1016/j.chroma.2016.01.068.

V.3 Erklärungen

Erklärung der Eigenleistung

Diese Dissertation wurde von mir verfasst. Kapitel 1-4 bestehen aus veröffentlichten Fachartikeln, die in Zusammenarbeit mit verschiedenen Kooperationspartnern verfasst wurden. Die Beiträge der einzelnen Ko-Autoren sind im Folgenden dargelegt.

Kapitel 1 – Die Reihe der chromatographischen Säulen wurde Dr. Justin M. Godinho in der Arbeitsgruppe von Prof. Dr. James W. Jorgenson gepackt und chromatographisch charakterisiert. Die Vorbereitung der Säulen für die optischen Aufnahmen, die lichtmikroskopischen Aufnahmen, die physikalischen Rekonstruktionen und die Analyse der erhaltenen Strukturen wurden von mir durchgeführt. Dr. Kristof Hormann half bei den lichtmikroskopischen Aufnahmen. Das Manuskript wurde von Prof. Dr. Ulrich Tallarek und mir ausgearbeitet und anschließend von Prof. Dr. Ulrich Tallarek in Zusammenarbeit mit unseren Kooperationspartnern überarbeitet, sowie von ihm eingereicht.

Kapitel 2 – Die experimentellen Arbeiten wurde analog zu Kapitel 1 von Dr. Justin M. Godinho und mir durchgeführt. Das Manuskript wurde von mir mit Hilfe von Prof. Dr. Ulrich Tallarek ausgearbeitet und anschließend von Prof. Dr. Ulrich Tallarek in Zusammenarbeit mit unseren Kooperationspartnern überarbeitet, sowie von ihm eingereicht.

Kapitel 3 – Die Studie wurde basierend auf den Ergebnissen der Kapitel 1 und 2 von allen Autoren gemeinsam konzipiert. Der genaue Aufbau der Packapparatur für die Nutzung von hoher Slurry-Konzentration und Ultraschall wurde Dr. Justin M. Godinho und mir entworfen. Die experimentellen Arbeiten wurden von Dr. Justin M. Godinho durchgeführt. Das Manuskript wurde von Dr. Justin M. Godinho ausgearbeitet und von Prof. Dr. James W. Jorgenson in Zusammenarbeit mit Prof. Dr. Ulrich Tallarek und mir überarbeitet und anschließend von Prof. Dr. James W. Jorgenson eingereicht.

Kapitel 4 – Die Studie wurde von mir konzipiert. Die chromatographische Säule wurde von Dr. Daniela Stoeckel eingebettet. Die Probenstücke wurden von mir vorbereitet und anschließend die elektronenmikroskopischen Aufnahmen von Dr. Sabine Schlabach und mir durchgeführt. Das Verfahren zur Bildaufarbeitung und Rekonstruktion der Packungsstruktur wurde von mir entwickelt und für beide Rekonstruktionen von mir angewendet. Die morphologische Analyse der erhaltenen 3D-Strukturen wurde von mir durchgeführt. Die lattice-Boltzmann-Simulationen wurden von Dr. Vasili Baranau in Zusammenarbeit mit mir durchgeführt und ausgewertet. Das Manuskript wurde von mir ausgearbeitet und von Prof. Dr. Ulrich Tallarek überarbeitet und eingereicht.

(Ort, Datum, Unterschrift des Promovierenden)

(Ort, Datum, Unterschrift des Betreuers)

Erklärung

Ich erkläre, dass eine Promotion noch an keiner anderen Hochschule als der Philipps-Universität Marburg, Fachbereich Chemie, versucht wurde.

Ich versichere, dass ich meine vorgelegte Dissertation

“Targeted optimization of chromatographic columns based on 3D analysis of packing microstructure”

selbst und ohne fremde Hilfe verfasst, nicht andere als die in ihr angegebenen Quellen oder Hilfsmittel benutzt, alle vollständig oder sinngemäß übernommenen Zitate als solche gekennzeichnet sowie die Dissertation in der vorliegenden oder einer ähnlichen Form noch bei keiner anderen in- oder ausländischen Hochschule anlässlich eines Promotionsgesuchs oder zu anderen Prüfungszwecken eingereicht habe.

Ort/Datum

Unterschrift
(Vor- und Zuname)